SEARCH FOR A NEW HEAVY GAUGE BOSON IN FINAL STATES WITH ONE LEPTON AND MISSING TRANSVERSE MOMENTUM WITH THE ATLAS DETECTOR

KyungEon Choi

Submitted to the faculty of the University Graduate School

in partial fulfillment of the requirements

for the degree

Doctor of Philosophy

in the Department of Physics,

Indiana University

December 2018

Accepted by the Graduate Faculty, Indiana University, in partial fulfillment of the requirements for the degree of Doctor of Philosophy.

Doctoral Committee

Hal Evans, Ph.D (Chair)

Sabine Lammers, Ph.D

Radovan Dermisek, Ph.D

Frederick Luehring, Ph.D

December 7, 2018

To my father

ACKNOWLEDGMENTS

I want to thank my advisor professor Hal Evans for his endless support and patience. I have to say that I am very fortunate to be a student of Hal and it could not be done without you.

I want to thank Fred Luehring for your warm support and pleasant conversations. Thanks to Sabine Lammers, Rick Van Kooten, Daria Zieminska for their kind support. Thanks to my colleagues Magnar Bugge, Philippe Calfayan, Ximo Poveda, Andrew Beddall, Nadezda Proklova for the enjoyable discussions and works at CERN. Thank my high school teacher Gwondul Son for your guidance to physics. Many thanks to professor In-Kwon Yoo for his support.

Thanks to my parents and parents-in-law for their love and sacrifice. I have to admit that the long endurance of my wife Sinee made this possible. I thank my son JiSung for his smile and dance.

Finally, thank you my Father in heaven for everything.

KyungEon Choi

SEARCH FOR A NEW HEAVY GAUGE BOSON IN FINAL STATES WITH ONE LEPTON AND MISSING TRANSVERSE MOMENTUM WITH THE ATLAS DETECTOR

The Standard Model (SM) has been an extremely successful theory in describing nature from the fundamental particles and their interactions. Despite the successes of the SM, there are phenomena which cannot be explained by the SM such as dark matter, neutrino mass, and gravity. Hence, various extensions to the SM have been developed during the last few decades, and several theoretical models predict the existence of additional heavy gauge bosons.

In this thesis, a search for a new heavy gauge boson in final states with one lepton (electron or muon) and missing transverse momentum is presented using the dataset of proton-proton collisions at a center-of-mass energy of 13 TeV, which were recorded in 2015, 2016, and 2017 by the ATLAS detector at Large Hadron Collider at CERN. No deviation from the Standard Model prediction is observed, and hence exclusion limits on the production cross section times branching ratio, $\sigma(pp \to W') \times \mathrm{BR}(W' \to \ell\nu)$ and on the Sequential Standard Model W' boson mass are derived exploiting the Bayesian approach. Masses for W' bosons up to 5.6 TeV are excluded by the combination of the electron and muon channels. This marks the most stringent exclusion limit obtained in the W' searches by any collider experiment so far.

Hal Evans, Ph.D (Chair)

Sabine Lammers, Ph.D

Radovan Dermisek, Ph.D

Frederick Luehring, Ph.D

CONTENTS

LIST OF FIGURES xi

LIST OF TABLES xv

1 Introduction 1

2 Theoretical Background 3
- 2.1 The Standard Model of Particle Physics 3
- 2.2 Limitations of the Standard Model 5
- 2.3 Physics Beyond the Standard Models with a Charged Lepton and a Neutrino in the Final State 6

3 Experimental Facilities 8
- 3.1 The Large Hadron Collider 8
  - 3.1.1 Beam Energy 8
  - 3.1.2 Luminosity 10
- 3.2 The ATLAS Detector 11
  - 3.2.1 Coordinate System 12
  - 3.2.2 Inner Detector 13
  - 3.2.3 Calorimeter System 15
  - 3.2.4 Muon Spectrometer 17

4 Reconstruction of Physics Objects 19
- 4.1 Track Reconstruction 20
  - 4.1.1 Track reconstruction in the ID 20
  - 4.1.2 Track reconstruction in the MS 22
  - 4.1.3 Track Parameters 23
- 4.2 Calorimeter Cluster Reconstruction 24
  - 4.2.1 Topological Cluster 25
- 4.3 High-level Physics Objects 26
  - 4.3.1 Electrons 27
  - 4.3.2 Muons 32
  - 4.3.3 Jets 36

Page

4.3.4 Missing Transverse Momentum . . . 38

5 Monte Carlo Simulation . . . 42

5.1 Monte Carlo Generator . . . 42

5.2 Detector Simulation . . . 44

5.2.1 Full Simulation . . . 44

5.2.2 Fast Simulation . . . 44

5.3 Digitization . . . 45

6 Signal Process . . . 46

6.1 Experimental Signature . . . 46

6.2 Signal Model . . . 47

7 Background Processes . . . 49

7.1 Irreducible Background . . . 49

7.1.1 W Boson Production . . . 49

7.2 Reducible Backgrounds . . . 51

7.2.1 Top Quark Pair and Single Top Production . . . 51

7.2.2 Z/γ^* Production . . . 53

7.2.3 Diboson Production . . . 53

7.2.4 Multijet Background . . . 54

8 Event Selection . . . 56

8.1 Collision Data . . . 56

8.2 Preselection . . . 57

8.2.1 Data Quality . . . 57

8.2.2 Event Cleaning . . . 58

8.3 Electron Channel . . . 58

8.3.1 Trigger Configuration . . . 58

8.3.2 Electron Object Selection . . . 59

8.3.3 Event Topology Selection . . . 62

8.3.4 Cut-flow in the Electron Channel . . . 64

8.4 Muon Channel . . . 65

8.4.1 Trigger Configuration . . . 65

8.4.2 Muon Object Selection . . . 65

8.4.3 Event Topology Selection . . . 67

8.4.4 Cut-flow in the Muon Channel . . . 69

8.5 Event Selection Efficiency for the W' Signal . . . 70

9 Background Estimation . . . 73

Page

9.1 Multijet Background Estimation . . . 73
9.1.1 Principle of the Matrix Method . . . 73
9.1.2 Multijet Background Estimation in the Electron Channel . . . 74
9.1.3 Multijet Background Estimation in the Muon Channel . . . 83
9.2 Backgrounds from MC Simulation . . . 87
9.3 Extrapolation to High Transverse Mass . . . 90
9.3.1 Extrapolation of the Top Background . . . 91
9.3.2 Extrapolation of the Diboson Background . . . 93
9.3.3 Extrapolation of the Multijet Background . . . 93

10 Systematic Uncertainties . . . 97
10.1 Experimental Systematic Uncertainties . . . 97
10.1.1 Electron . . . 97
10.1.2 Muon . . . 98
10.1.3 Jet and $E_{\mathrm{T}}^{\mathrm{miss}}$ . . . 99
10.1.4 Pile-up . . . 100
10.1.5 Luminosity . . . 100
10.1.6 Multijet Background Estimation . . . 100
10.1.7 Extrapolation . . . 104
10.2 Theoretical Systematic Uncertainties . . . 104
10.2.1 W and Z Backgrounds . . . 104
10.2.2 Top and Diboson Backgrounds . . . 105
10.3 Summary . . . 105

11 Results . . . 111

12 Statistical Interpretation of the Results . . . 116
12.1 Framework for Statistical Analysis . . . 116
12.2 Discovery Statistics . . . 118
12.2.1 Frequentist Probability for Discovery of a New Signal . . . 118
12.2.2 Results . . . 121
12.3 Exclusion Limits . . . 123
12.3.1 Bayesian Limit on the Signal Cross Section . . . 123
12.3.2 Results . . . 125
12.3.3 Comparison to the Previous Searches . . . 127

13 Conclusion and Outlook . . . 128

A Monte Carlo Background Samples . . . 129

B Low-p_{T} Control Region . . . 139

BIBLIOGRAPHY 143

LIST OF FIGURES

Figure Page

3.1 The CERN accelerator complex [23]. . . . 9

3.2 Cross sections for several physics processes as a function of center-of-mass energy. 11

3.3 Cutaway view of the ATLAS detector indicating locations of sub-detectors. . . . 12

3.4 Schematic view of the inner barrel detectors. . . . 14

3.5 Schematic view of the inner end-cap detectors and Pixel and SCT barrel. The IBL installed during LS1 is not shown. . . . 14

3.6 The cutaway view of the ATLAS calorimeter system. . . . 16

3.7 Schematic view of a barrel module of the LAr EM calorimeter. . . . 16

3.8 The cutaway view of the ATLAS muon system. . . . 17

3.9 Schematic view of the muon spectrometer in the x-y projection [25]. . . . 18

4.1 Schematic cutaway of the ATLAS detector with the signatures from various particles. . . . 19

4.2 Space-points and track finding seeds in the Pixel and SCT barrel layers from a $t\bar{t}$ event. The IBL at a radius of 33.25 mm is missing in the figure. . . . 21

4.3 TRT extenstions in red full circles and TRT segments in black full circles in the ID barrel for the same $t\bar{t}$ event shown in Figure 4.2. The IBL at a radius of 33.25 mm is missing in the figure. . . . 22

4.4 Schematic of the transverse and longitudinal impact parameters in the ATLAS coordinate system. . . . 24

4.5 The electron identification efficiencies measured from reconstructed electrons in the MC simulation for $Z \to ee$ (left) and dijet (right) samples. . . . 30

5.1 Schematic representation of the full production chain. . . . 42

6.1 Feynman diagram of SSM W' production. . . . 47

6.2 The truth invariant mass and truth transverse mass distributions of the flat W' samples, the fixed mass W' samples, and the reweighted to the same mass points from the flat W' samples. . . . 48

7.1 Leading order Feynman diagrams of W production. . . . 49

7.2 The truth invariant mass and truth transverse mass distributions of the invariant mass-binned W samples. . . . 51

Figure Page

7.3 Leading order Feynman diagrams of $t\bar{t}$ production. 51

7.4 Leading order Feynman diagrams of single top productions for Wt (left), s-channel (middle), and t-channel (right) processes. 52

7.5 Leading order Feynman diagrams of Z/γ^* production 53

7.6 Some leading order Feynman diagrams of QCD dijet production 54

8.1 Left: Cumulative integrated luminosity delivered to ATLAS (green), recorded by ATLAS (yellow), and certified to be good quality data (blue) versus time from 2015 to 2017. Right: Mean number of interactions per bunch crossing distributions from 2015 to 2017. 56

8.2 The distributions of d_0 significance on the top and $|\Delta z_0 \sin\theta|$ on the bottom. The left plots show the distributions for electrons with a truth matching requirement ($\Delta R < 0.2$) in the W' flat sample. The right plots show the distributions for backgrounds and data at final selection. 61

8.3 The cut efficiency of d_0 significance as a function of p_{T} (left) and the cut efficiency of $|\Delta z_0 \sin\theta|$ as a function of $\langle\mu\rangle$ (right). Both efficiencies are measured in the W' flat sample. 62

8.4 The distributions of d_0 significance on the top and $|\Delta z_0 \sin\theta|$ on the bottom. The left plots show the distributions for muons with a truth matching requirement ($\Delta R < 0.2$) in the W' flat sample. The right plots show the distributions for backgrounds and data at final selection. 66

8.5 Total W' signal acceptance $\times$ efficiency as a function of SSM W' pole mass in the electron channel and the muon channel. 72

9.1 Real efficiency as a function of p_{T} and η estimated from W MC sample. 75

9.2 Real efficiency as a function of p_{T} and η estimated from W MC sample. 76

9.3 Dilution in p_{T}, $E_{\mathrm{T}}^{\mathrm{miss}}$, and $\Delta\phi$ for the loose selection with $p_{\mathrm{T}} < 145$ GeV (left) and with $p_{\mathrm{T}} > 145$ GeV (right). 78

9.4 Dilution in p_{T}, $E_{\mathrm{T}}^{\mathrm{miss}}$, and $\Delta\phi$ for the tight selection with $p_{\mathrm{T}} < 145$ GeV (left) and with $p_{\mathrm{T}} > 145$ GeV (right). 79

9.5 Fake efficiency as a function of p_{T}, η, $E_{\mathrm{T}}^{\mathrm{miss}}$, and $\Delta\phi$. 80

9.6 Fake efficiency as a function of $\Delta\phi$ vs. p_{T} 80

9.7 The η, ϕ, p_{T}, $E_{\mathrm{T}}^{\mathrm{miss}}$, m_{T}, and $\Delta\phi$ distributions in the multijet validation region . 82

9.8 The multijet background in the electron channel 83

9.9 The real efficiency as a function of p_{T} in the muon channel. 84

9.10 The fake efficiency as a function of p_{T} in the muon channel. 85

Figure Page

9.11 The number of jets, d_0 significance, p_{T}, $E_{\mathrm{T}}^{\mathrm{miss}}$, m_{T}, and $|\Delta\phi_{\mu,E_{\mathrm{T}}^{\mathrm{miss}}}|$ distributions in the multijet validation region . . . 86

9.12 The multijet background in the muon channel . . . 87

9.13 Background extrapolation of the top background in the electron channel (left) and the muon channel (right). . . . 92

9.14 Background extrapolation of the diboson background in the electron channel (left) and the muon channel (right). . . . 94

9.15 Background extrapolation of the multijet background in the electron channel. . . 95

9.16 Background extrapolation of the multijet background in the muon channel. . . . 96

10.1 Fake efficiency variations as a function of p_{T} and $\Delta\phi$ from the fake enriched samples. The solid and dashed lines correspond to $p_{\mathrm{T}} < 145$ GeV and $p_{\mathrm{T}} > 145$ GeV respectively. . . . 101

10.2 Relative uncertainty of the multijet backgrounds as a function of $E_{\mathrm{T}}^{\mathrm{miss}}$ for the fake efficiency variations at final selection (left). The ratio of the total background with the fake efficiency variations to the nominal at final selection (right).102

10.3 The real efficiency (left) and the fake efficiency (right) as a function of p_{T} for the systematic variations. . . . 103

10.4 The multijet backgrounds in the m_{T} distribution at final selection under all systematic variations (left). The ratio of the total background with the systematic variations to the nominal (right). The different line styles in the right-hand side plot respresent different background extraploation ranges. . . . 103

10.5 Experimental systematic uncertainties on the electron (left) and the muon (right).106

10.6 Experimental systematic uncertainties on the jet and $E_{\mathrm{T}}^{\mathrm{miss}}$ in the electron channel (left) and the muon channel (right). . . . 106

10.7 Experimental systemtic uncertainties on the background extrapolation, pile-up, and luminosity in the electron channel (left) and the muon channel (right). . . 107

10.8 Theoretical systematic uncertainties in the electron channel (left) and the muon channel (right). . . . 107

11.1 Electron η (left top), ϕ (right top), p_{T} (left bottom), and $E_{\mathrm{T}}^{\mathrm{miss}}$ (right bottom) distributions at the signal selection in the $W' \to e\nu$ channel. . . . 112

11.2 Muon η (left top), ϕ (right top), p_{T} (left bottom), and $E_{\mathrm{T}}^{\mathrm{miss}}$ (right bottom) distributions at the signal selection in the $W' \to \mu\nu$ channel. . . . 113

11.3 Transverse mass distributions at the signal selection in the electron (left) and muon (right) channels. As examples, the expected SSM W' signal distributions for three different masses are shown on top of the SM prediction. . . . 114

Figure Page

12.1 Distribution of the test statistic q_0 for background-only pseudo-experiments in the electron channel (left) and muon channel (right). 119

12.2 The mapping between the highest local significance and global significance for the electron channel, the muon channel, and the combined. 121

12.3 The local p-values from W'_{SSM} signals between 0.35 and 6 TeV for the electron (top left), muon (top right), and combined channel (bottom). The local significance levels are shown as dashed lines. 122

12.4 W' cross section limit results for the electron channel (top), the muon channel (middle) and combined (bottom). 126

B.1 Distributions of the η (top left), $|\Delta\phi_{e,E_{\mathrm{T}}^{\mathrm{miss}}}|$ (top right), $E_{\mathrm{T}}^{\mathrm{miss}}$ (bottom left) and m_{T} (bottom right) for electron p_{T} less than 145 GeV in the final selection. . . . 139

B.2 Distributions of the $|\Delta\phi_{e,E_{\mathrm{T}}^{\mathrm{miss}}}|$ (top) and $|p_{\mathrm{T}} - E_{\mathrm{T}}^{\mathrm{miss}}|$ (bottom) between electron p_{T} and $E_{\mathrm{T}}^{\mathrm{miss}}$ for electron $p_{\mathrm{T}} < 145$ GeV on the left hand side and $145 < p_{\mathrm{T}} < 300$ GeV on the right hand side. 140

B.3 Distributions of the p_{T}, $E_{\mathrm{T}}^{\mathrm{miss}}$, η, $|\Delta\phi_{e,E_{\mathrm{T}}^{\mathrm{miss}}}|$, $|p_{\mathrm{T}} - E_{\mathrm{T}}^{\mathrm{miss}}|$ and m_{T} without the multijet background for electron p_{T} less than 145 GeV in the final selection. . . 142

LIST OF TABLES

Table Page

2.1 The fundamental particles of the SM for the matter particles (left), gauge bosons (middle), and the Higgs boson (right). 4

4.1 List of discriminating variables for electron identification. 29

4.2 The electron isolation operating points which are set by the efficiency of the isolation requirement. 31

4.3 Muon reconstrution efficiencies for the identification selections evaludated in the region of $|\eta| < 2.5$ from W MC for prompt muons and $t\bar{t}$ MC for background muons from hadrons. 34

4.4 The muon isolation operating points which are set by the efficiency of the isolation requirement. 35

8.1 Trigger configuration of electron channel for each data-taking period 58

8.2 Number of events after each selection in the electron channel. The numbers in the parentheses are the efficiencies with respect to the previous line. 64

8.3 Number of events after each selection in the muon channel. The numbers in the parentheses are the efficiencies with respect to the previous line. 69

8.4 Cut efficiency flow of W' signals in the electron channel. The efficiencies are with respect to the previous line. The numbers in parentheses are the number of events normalized to the integrated luminosity of the data, but without corrections such as K-factors, efficiency scale factors, and pileup reweighting. . . 70

8.5 Cut efficiency flow of W' signals in the muon channel. The efficiencies are with respect to the previous line. The numbers in parentheses are the number of events normalized to the integrated luminosity of the data, but without corrections such as K-factors, efficiency scale factors, and pileup reweighting. 71

9.1 Cut efficiency flow in the electron channel. The efficiencies are with respect to the previous line. The numbers in parentheses are the number of events normalized to the integrated luminosity of the data, but without corrections such as K-factors, efficiency scale factors, and pileup reweighting. All samples are skimmed with the requirement of at least one electron satisfying the loose likelihood operating point with $p_{\mathrm{T}} > 60$ GeV. 89

Table Page

9.2 Cut efficiency flow in the muon channel. The efficiencies are with respect to the previous line. The numbers in parentheses are the number of events normalized to the integrated luminosity of the data, but without corrections such as K-factors, efficiency scale factors, and pileup reweighting. All samples are skimmed with the requirement of at least one combined muon with $p_{\mathrm{T}} > 50$ GeV. 90

10.1 Summary of the systematic uncertainties and correlations between channels. . . 109

10.2 Systematic uncertainties in the expected number of events as estimated for the total background and for signal with a W'_{SSM} mass of 2 (4) TeV. The uncertainty is estimated with the binning shown in Figure 10.5 to 10.8 at $m_{\mathrm{T}} = 2$ (4) TeV for the background and in a three-bin window around $m_{\mathrm{T}} = 2$ (4) TeV for the signal. Uncertainties that are not applicable are denoted "N/A", and "negl." means that the uncertainty is not included in the statistical analysis. Sources of uncertainties not included in the table are neglected in the statistical analysis. 110

11.1 Contributions of individual backgrounds with uncertainties for different m_{T} regions in the electron channel. The uncertainties include both statistical uncertainty and all systematics, and all weights are included so that the total background level can be compared to data. 115

11.2 Contributions of individual backgrounds with uncertainties for different m_{T} regions in the muon channel. The uncertainties include both statistical and systematic uncertainty, and all weights are included so that the total background level can be compared to data. 115

12.1 Expected and observed 95% CL lower limit on the SSM W' mass in the electron and muon channels and their combination. 126

12.2 Observed 95% CL lower limits on the SSM W' mass from previous and other searches. The last row is the result of this analysis. 127

A.1 Monte Carlo samples for backgrounds that contribute to both the electron and muon channels. For each dataset, the following is listed: the ATLAS Monte Carlo dataset ID, the physics process (including the mass range in GeV when appropriate), the number of generated events, the cross section times branching ratio, K-factor, and the equivalent integrated luminosity $L_{\mathrm{int}} = N_{evt}/(\sigma B)$. Letters in the parentheses represent Monte Carlo samples with the 2015+2016 dataset pile-up profile with (a) and the 2017 dataset pile-up profile with (d). . 129

A.2 Monte Carlo samples for backgrounds that contribute to the electron channel. For each dataset, the following is listed: the ATLAS Monte Carlo dataset ID, the physics process (including the mass range in GeV when appropriate), the number of generated events, the cross section times branching ratio, K-factor ($K(m)$ denotes a mass dependent K-factor is used), and the equivalent integrated luminosity $L_{\mathrm{int}} = N_{evt}/(\sigma B)$. Letters in the parentheses represent Monte Carlo samples with the 2015+2016 dataset pile-up profile with (a) and the 2017 dataset pile-up profile with (d). 130

Table Page

A.3 Monte Carlo samples for backgrounds that contribute to the electron channel. For each dataset, the following is listed: the ATLAS Monte Carlo dataset ID, the physics process (including the mass range in GeV when appropriate), the number of generated events, the cross section times branching ratio, K-factor ($K(m)$ denotes a mass dependent K-factor is used), and the equivalent integrated luminosity $L_{\text{int}} = N_{evt}/(\sigma B)$. Letters in the parentheses represent Monte Carlo samples with the 2015+2016 dataset pile-up profile with (a) and the 2017 dataset pile-up profile with (d). 131

A.4 Monte Carlo samples for backgrounds that contribute to the muon channel. For each dataset, the following is listed: the ATLAS Monte Carlo dataset ID, the physics process (including the mass range in GeV when appropriate), the number of generated events, the cross section times branching ratio, K-factor ($K(m)$ denotes a mass dependent K-factor is used), and the equivalent integrated luminosity $L_{\text{int}} = N_{\text{evt}}/(\sigma B)$. Letters in the parentheses represent Monte Carlo samples with the 2015+2016 dataset pile-up profile with (a) and the 2017 dataset pile-up profile with (d). 132

A.5 Monte Carlo samples for backgrounds that contribute to the muon channel. For each dataset, the following is listed: the ATLAS Monte Carlo dataset ID, the physics process (including the mass range in GeV when appropriate), the number of generated events, the cross section times branching ratio, K-factor ($K(m)$ denotes a mass dependent K-factor is used), and the equivalent integrated luminosity $L_{\text{int}} = N_{\text{evt}}/(\sigma B)$. Letters in the parentheses represent Monte Carlo samples with the 2015+2016 dataset pile-up profile with (a) and the 2017 dataset pile-up profile with (d). 133

A.6 Monte Carlo samples for backgrounds that contribute to both the electron and muon channels. For each dataset, the following is listed: the ATLAS Monte Carlo dataset ID, the physics process (including the mass range in GeV when appropriate), the number of generated events, the cross section times branching ratio, K-factor ($K(m)$ denotes a mass dependent K-factor is used, see appendix), and the equivalent integrated luminosity $L_{\text{int}} = N_{\text{evt}}/(\sigma B)$. Letters in the parentheses represent Monte Carlo samples with the 2015+2016 dataset pile-up profile with (a) and the 2017 dataset pile-up profile with (d). 134

A.7 Monte Carlo samples for backgrounds that contribute to both the electron and muon channels. For each dataset, the following is listed: the ATLAS Monte Carlo dataset ID, the physics process (including the mass range in GeV when appropriate), the number of generated events, the cross section times branching ratio, K-factor ($K(m)$ denotes a mass dependent K-factor is used, see appendix), and the equivalent integrated luminosity $L_{\text{int}} = N_{\text{evt}}/(\sigma B)$. Letters in the parentheses represent Monte Carlo samples with the 2015+2016 dataset pile-up profile with (a) and the 2017 dataset pile-up profile with (d). 135

Table Page

A.8 Monte Carlo samples for backgrounds that contribute to the electron channel. For each dataset, the following is listed: the ATLAS Monte Carlo dataset ID, the physics process (including the mass range in GeV when appropriate), the number of generated events, the cross section times branching ratio, K-factor ($K(m)$ denotes a mass dependent K-factor is used), and the equivalent integrated luminosity $L_{\text{int}} = N_{evt}/(\sigma B)$. Letters in the parentheses represent Monte Carlo samples with the 2015+2016 dataset pile-up profile with (a) and the 2017 dataset pile-up profile with (d). 136

A.9 Monte Carlo samples for backgrounds that contribute to the muon channel. For each dataset, the following is listed: the ATLAS Monte Carlo dataset ID, the physics process (including the mass range in GeV when appropriate), the number of generated events, the cross section times branching ratio, K-factor ($K(m)$ denotes a mass dependent K-factor is used), and the equivalent integrated luminosity $L_{\text{int}} = N_{evt}/(\sigma B)$. Letters in the parentheses represent Monte Carlo samples with the 2015+2016 dataset pile-up profile with (a) and the 2017 dataset pile-up profile with (d). 137

A.10 Monte Carlo samples for backgrounds that contribute to both the electron and muon channels. For each dataset, the following is listed: the ATLAS Monte Carlo dataset ID, the physics process (including the mass range in GeV when appropriate), the number of generated events, the cross section times branching ratio, K-factor ($K(m)$ denotes a mass dependent K-factor is used), and the equivalent integrated luminosity $L_{\text{int}} = N_{evt}/(\sigma B)$. Letters in the parentheses represent Monte Carlo samples with the 2015+2016 dataset pile-up profile with (a) and the 2017 dataset pile-up profile with (d). 138

1. Introduction

The quest to understand the fundamental building blocks of nature and their interactions is one of the oldest and most ambitious of human endeavors. Remarkable breakthroughs by dozens of experiments in the early 20th century established the concept of particles such as the proton [1], neutron [2] and electron [3]. Further discoveries of new particles led to an introduction of the quark model [4], which describes new particles as bound states of quarks and gluons. Successes of theoretical predictions and experimental observations led to the formulation of the Standard Model (SM), which describes the fundamental particles and their interactions in quantum field theory. The SM is a very successful theory as numerous experimental measurements agree with the SM predictions in great precision. The last missing piece of the SM, the Higgs boson, was discovered [5, 6] in 2012 by the ATLAS (A Toroidal LHC ApparatuS) and CMS (Compact Muon Solenoid) experiments at the LHC (Large Hadron Collider) at CERN. Even though the SM is completed with the Higgs boson, there are phenomena which cannot be explained by the SM such as dark matter, neutrino mass, and gravity. Hence, various extensions to the SM have been developed during the last few decades as we know the SM is not a complete theory to explain all that we see from nature. In this thesis, a search for a new heavy gauge boson, which is predicted by several theories for physics beyond the SM, is presented. The analysis is performed using the dataset of proton-proton collisions at a center-of-mass energy of 13 TeV, which are collected from 2015-2017 by the ATLAS detector. The final states with one electron or one muon and missing transverse momentum are considered in the analysis. This thesis is organized as follows:

Chapter 2 outlines the theoretical backgrounds of the analysis of this thesis.

Chapter 3 gives an overview of the LHC and the ATLAS detector.

Chapter 4 explains the reconstruction of track, calorimeter cluster, and high-level physics objects with the ATLAS detector.

Chapter 5 describes Monte Carlo simulation of proton-proton collisions and the simulation of detector responses.

Chapter 6 discusses the experimental signature of the signal process and the benchmark model used in the analysis of this thesis.

Chapter 7 describes various background processes arising from the SM processes which contribute to the search for a new heavy boson in final states with an electron or muon and missing transverse momentum.

Chapter 8 presents the datasets for the analysis and the event selections for both electron and muon channels.

Chapter 9 discusses the background estimations for MC-based backgrounds and a background with the data-driven estimation technique.

Chapter 10 describes the experimental and theoretical systematic uncertainties on the background estimations and the signal predictions.

Chapter 11 presents the result of the event selection and the background estimations with uncertainties by comparing the expected background to the data.

Chapter 12 presents the statistical interpretation of the result presented in Chapter 11.

Chapter 13 gives a summary of the results and an outlook on the future searches for a new heavy boson in final states with one electron or one muon and missing transverse momentum.

2. Theoretical Background

The theoretical background of the analysis of this thesis is briefly introduced. Section 2.1 introduces the basic concept of the SM as it is the basis of modern particle physics. The limitations of the SM and the theories of the physics beyond the Standard Model (BSM) are introduced in Section 2.2.

2.1 The Standard Model of Particle Physics

The SM describes nature by means of fundamental particles and their interactions. It has been developed over the last decades with an interplay between theoretical predictions and experimental discoveries. The SM includes three of the four *known* fundamental forces in nature: the strong interaction, the weak interaction, and the electromagnetic interaction.

Relativistic quantum field theory [7] is a mathematical framework to construct the SM. The fundamental particles are described by the states of quantized fields. Table 2.1 shows fundamental matter particles on the left-hand side, which are associated with fields of spin-1/2 and called fermions. The Lagrangian of the SM, which describes the motion and interactions of excitations of the fields, is based on a gauge group of SU(3)×SU(2)×U(1). Thus, the Lagrangian of the SM is invariant under space-time dependent local transformations. The gauge invariance of the Lagrangian requires additional quantum fields with spin-1. These are called gauge fields and associated with the gauge bosons as shown in the middle of Table 2.1. In the SM, twelve gauge fields are included in the Lagrangian: eight for the SU(3) gauge symmetry (gluons, g) to describe the strong interactions, three for the SU(2) gauge symmetry ($W^{\pm}$ and Z bosons) to describe the weak interactions, and one for the U(1) gauge symmetry (photons, γ) to describe the electromagnetic interactions.

A modification to the theory described above is required due to the masses of particles. The gauge fields of the electromagnetic and weak interactions, governed by the SU(2)×U(1)

Spin-1/2 fermions

	Generations I	II	III
Quarks	u	c	t
	d	s	b
Lepton	e^-	μ^-	τ^-
	ν_e	ν_μ	ν_τ

Spin-1 gauge bosons

Strong force	g
Weak force	$W^\pm$, Z^0
Electromagnetic force	γ

Spin-0 boson

H

Table 2.1. The fundamental particles of the SM for the matter particles (left), gauge bosons (middle), and the Higgs boson (right).

symmetry, should appear as massless particles to preserve gauge invariance. However, the gauge bosons are required to have a large mass in order to properly describe the weak force, which seemingly contradicts the prediction. Another factor is due to the fact that the weak interaction violates parity and couples differently to the left and right-handed quarks and lepton helicity states. Hence, the left and right-handed fermions are considered as different fields with different couplings in the SM. A fermion mass term in the Lagrangian would couple these different fields and thus break gauge invariance. In order to preserve the gauge invariance of left-handed weak interaction, the fermion fields should not have mass terms and consequently the quarks and leptons should be massless particles. This contradicts the massive quarks and leptons from the observations.

An introduction of additional quantum fields to the theory resolves the masses of particles. These fields couple to the electroweak SU(2)×U(1) gauge fields and have spin-0, which are also called *scalar* fields. The scalar fields are included in the Lagrangian of the SM in a way that follows the SU(2)×U(1) symmetry and preserves the gauge invariance. The key is that the scalar fields take a special form of interactions such that zero values of the fields do not correspond to the lowest energy state. While the actual interaction in the Lagrangian preserves the SU(2)×U(1) symmetry, the ground state of the fields necessarily break the symmetry. Hence, the Lagrangian preserves gauge invariance, despite the particular vacuum which describes nature does not show SU(2)×U(1) symmetry. This is called *spontaneous symmetry breaking*.

As a result of the spontaneous symmetry breaking, the scalar fields take a non-zero value, called the *vacuum expectation value* (VEV). The VEV couples to the fermion and gauge fields in a way that is equivalent to having mass terms. As a result, the fermions and gauge bosons appear as massive particles in nature, which is consistent with the experimental observations. Another consequence of the spontaneous symmetry breaking is the prediction of a massive scalar particle. The interactions that generate the VEV give mass to one of the additional scalar fields. This field should appear as a neutral massive spin-zero boson in nature. This particle is called the Higgs boson, which was discovered by the ATLAS and CMS experiments in 2012 [5, 6].

2.2 Limitations of the Standard Model

All particles predicted by the SM have been observed, and relationships between SM parameters have been confirmed experimentally to a high degree of accuracy. Despite the great successes of the SM, there are motivations for physics beyond the Standard Model as described below.

- **Neutrino mass**: The Standard Model does not include right-handed neutrinos as they do not participate in any SM interactions. The observations of neutrino-oscillations are interpreted as requiring some small masses for neutrinos. The massive neutrinos lead to an inclusion of right-handed neutrinos into the SM. An extension of the SM can be justified to have interactions for right-handed neutrinos.

- **Dark matter and dark energy**: The existence of dark matter is supported by many astrophysical observations such as measurements of the cosmic microwave background fluctuations [8] and observations of gravitational lensing [9]. The existence of dark energy is needed to explain the observed acceleration of the expansion of the universe [10]. Neither of them are included in the SM. The only candidate in the SM is neutrinos but the SM neutrinos can account for a small fraction of the dark matter due to light mass.

- **Hierarachy problem**: The mass of the Higgs boson contains large contributions from radiative loop corrections. In particular, it is sensitive to heavy particles of the SM (as well as to hypothetical particles of new physics that might lie at the TeV scale). These corrections are quadratically divergent which leads to an unnaturally high mass of the Higgs boson. It is possible to restore the Higgs mass to a proper value through fine-tuning, but this is considered to be unnatural.

2.3 Physics Beyond the Standard Models with a Charged Lepton and a Neutrino in the Final State

Many theories which extend the SM have been developed to describe phenomena which cannot be explained by the SM as discussed in the previous chapter. These include theories such as supersymmetry [11], extra dimensions [12], and extended gauge groups [13]. Some of these theories predict additional heavy gauge bosons (so-called W' and Z'). The following are some models which include final states with one lepton (electron or muon) and missing transverse momentum. Models that do not predict additional heavy gauge bosons but share final states are also introduced as the search presented in this thesis can be interpreted in the context of these models.

Left Right Symmetric Model

The left-right symmetric model [14] includes the $W_R'^{\pm}$ bosons which obtain a mass via spontaneous symmetry breaking of a gauge group SU(2)$_R\times$SU(2)$_L\times$U(1). The mass of the $W_R'^{\pm}$ bosons is expected to be higher than the SM W boson, and the couplings to the quarks and leptons are equal to the SM W boson. Therefore, the $W_R'^{\pm}$ bosons can be observed in the final state of one lepton and missing transverse momentum.

Sequential Standard Model

The Sequential Standard Model (SSM) [15] introduces the W' as a heavy partner of the SM W boson with the same couplings and quantum numbers, but higher mass and width. The SSM is not considered as a realistic model due to lack of theoretical motivation, but it has been used as a benchmark model for experimental W' boson searches for more than two decades. In this context, the interference between the SSM W' and the SM W boson is not included in the SSM W' signal model as it leads to additional complications to the model. The width of W' boson is approximately 3% of the pole mass, and about 33 GeV for a W' mass of 1 TeV.

Supersymmetry Models

In some supersymmetry models [16], charginos ($\tilde{\chi}^{\pm}$) can be produced together with neutralinos ($\tilde{\chi}^{0}$) at the energy of the LHC. Thereafter, charginos can further decay into a lepton and neutrino and neutralinos can decay into a sneutrino and a neutrino. Thus, the final state of the production can be one charged lepton and missing transverse momentum.

Dark Matter Models

The dark matter candidate particle, called weakly interacting massive particle (WIMP), can be produced in pairs at the energy of the LHC, $pp \to \chi\bar{\chi}$, via a unknown interaction. These particles cannot be measured as they do not leave any signature in the detectors. Hence, searches are performed via initial state radiation of a SM particle [17, 18, 19, 20], $pp \to \chi\bar{\chi} + X$ where X is a gluon or a W boson. In case of a W boson radiation, the final state can be one lepton and missing transverse momentum from a neutrino and WIMPs.

3. Experimental Facilities

Many of the modern particle physics experiments utilize particle accelerators to understand the universe as it allows us to produce rare decays in control. A detector system should accompany a particle accelerator to measure produced particles. In this chapter, the accelerator and the detector used in the work of this thesis will be introduced.

3.1 The Large Hadron Collider

The Large Hadron Collider (LHC) [21] is a two-ring superconducting hadron accelerator located at CERN laboratory in Geneva, Switzerland. The machine is installed inside a 26.7 km long tunnel and around 100 m below ground. It is designed to accelerate protons (p) and heavy ions (A) and has delivered pp, pA and AA collisions. There are four main detectors installed at the interaction points of the LHC: ALICE (A Large Ion Collider Experiment), ATLAS [22], CMS (Compact Muon Solenoid), and LHCb (Large Hadron Collider beauty). All experiments generally cover a wide range of physics programs with the following primary purpose. The ATLAS and CMS experiments are designed to investigate a variety of Standard Model and Beyond Standard Model physics. The LHCb experiment is designed to investigate b-quark physics and CP-violation. The ALICE experiment is designed to investigate the quark-gluon plasma via heavy ion collisions.

3.1.1 Beam Energy

Multiple stages of particle acceleration are required to reach the nominal energy of the LHC. Figure 3.1 shows the CERN accelerator complex. Hydrogen atoms are ionized, and protons are accelerated to the energy of 50 MeV in the LINAC 2. Protons are then injected into the Proton Synchrotron Booster (PSB), then to the Proton Synchrotron (PS), then to

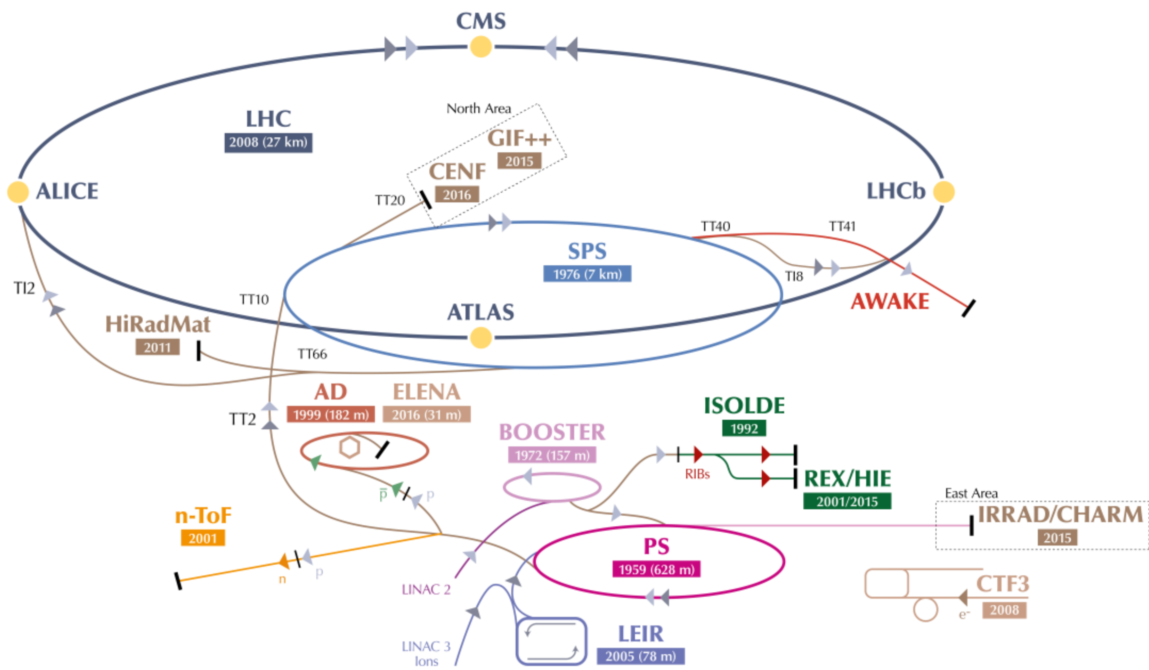

Figure 3.1. The CERN accelerator complex [23].

the Super Proton Synchrotron (SPS). The energies of protons are 1.4 GeV, 25 GeV and 450 GeV after an acceleration in the PSB, the PS and the SPS respectively. Finally, protons are injected into the each LHC ring then accelerated up to 7 TeV.

The LHC was first fired up in 2008 and then 2009 for short periods. In 2010 and 2011, the machine started to operate with the moderate energy of 3.5 TeV. The beam energy was pushed to 4 TeV in 2012. The LHC operation restarted in 2015 after the first Long Shutdown (LS1), and the beam energy was increased to 6.5 TeV, which gives a center-of-mass energy of 13 TeV, from 2015 to 2017 [24].

3.1.2 Luminosity

The LHC is designed to deliver protons in 2808 bunches per ring and 1.15×10^{11} protons per bunch with a bunch space of 25 ns. The instantaneous luminosity of the pp collision is given by

$$\mathcal{L} = \frac{\langle\mu\rangle n_{\mathrm{b}} f_{\mathrm{r}}}{\sigma_{\mathrm{inel}}} \tag{3.1}$$

where $\langle\mu\rangle$ is an average number of inelastic interactions per bunch crossing, n_b is the number of colliding bunch pairs, f_r is the bunch revolution frequency, and σ_{inel} is the pp inelastic cross section. The resulting peak instantaneous luminosity was measured as 2.09×10^{34} $\mathrm{cm}^2\mathrm{s}^{-1}$ during the data taking in 2017.

In addition to the energy, the luminosity is an important characteristic of the LHC, as the expected number of events per second of a specific physics process is given by

$$N_{event} = \mathcal{L}\sigma_{event} \tag{3.2}$$

where σ_{event} is the cross section of a given physics process. Figure 3.2 shows the expected event rates for several physics processes in proton-(anti)proton collisions as a function of center-of-mass energy. The higher energy and higher luminosity of the LHC than the Tevatron allowed the discovery of the Higgs boson. Precision measurements of the Standard Model processes and searches for the new physics beyond the Standard Model are currently being performed. Higher energy and higher luminosity are still being vigorously pursued such as HL-LHC (High Luminosity LHC) project and FCC (Future Circular Collider) project.

An important characteristic of instantaneous luminosity in the LHC is the average number of inelastic interactions per bunch crossing, which is also called pile-up. The pile-up reached up to 70 during the data taking in 2017, which results in a challenging complication for reconstruction of various physics objects. As an example, a collision of a pair of protons produces a Higgs particle of interest which decays into 4 leptons. There are additional 69 proton-proton collisions in the given bunch crossing, which produce a bunch of particles. Thus, various methods to deal with pile-up used for the results in this thesis will be discussed in Section 4.

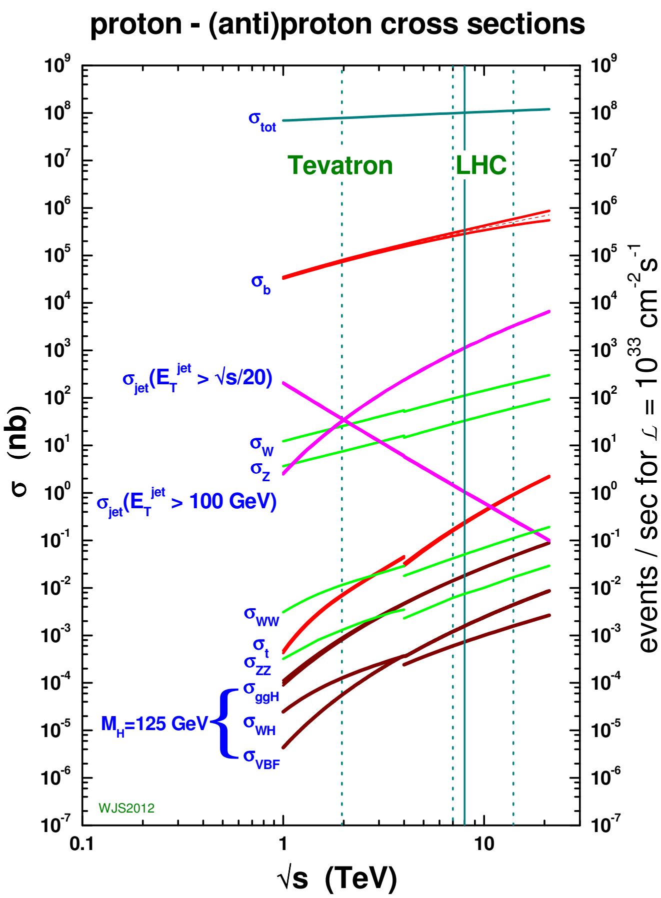

Figure 3.2. Cross sections for several physics processes as a function of center-of-mass energy.

3.2 The ATLAS Detector

The ATLAS detector is a general-purpose detector which measures a wide range of physics objects produced by proton-proton collisions at the LHC. The dimensions of the detector are 44 m in length and 25 m in height, and it weighs approximately 7000 tonnes as depicted in Figure 3.3.

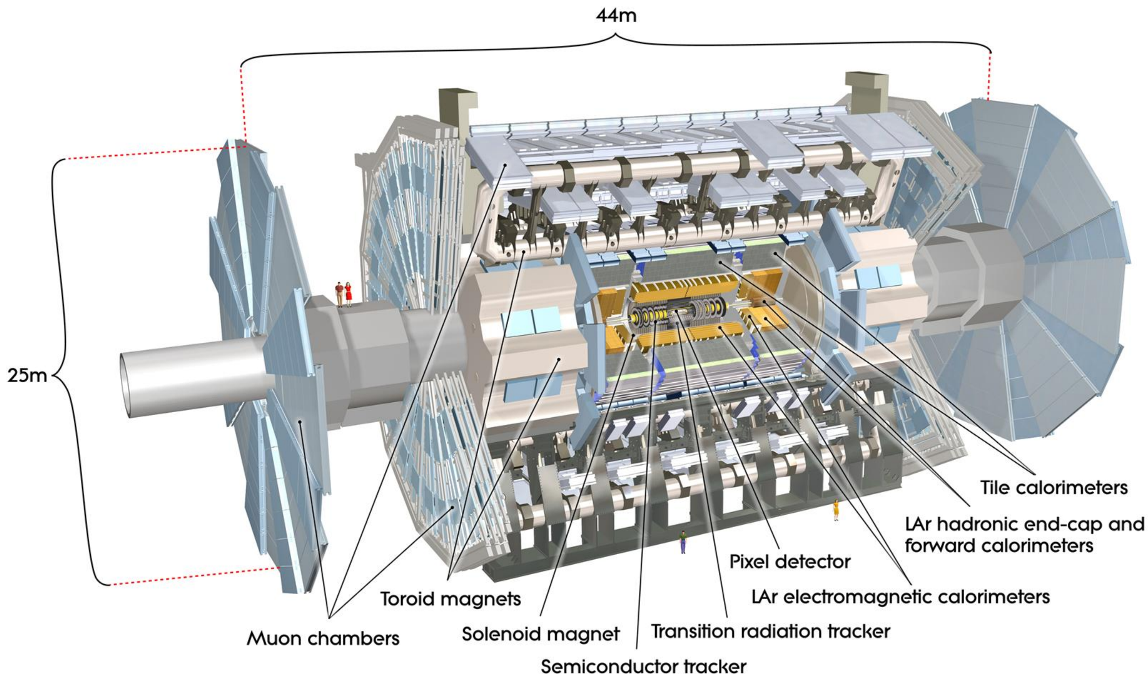

Figure 3.3. Cutaway view of the ATLAS detector indicating locations of sub-detectors.

The ATLAS detector consists of a series of concentric sub-systems around the LHC beam pipe where protons collide each other. The ATLAS detector is divided into three main sub-systems: the inner detector is located at the center of the ATLAS, the calorimeter system follows, and the muon spectrometer is the outermost system.

3.2.1 Coordinate System

The coordinate system of the ATLAS detector defines the nominal interaction point (IP) as the origin of the coordinate system. The z-axis is defined in parallel to the beam direction, and the x-y plane is defined as the transverse plane to the beam direction. The positive x-axis is defined as the horizontal axis pointing the center of the LHC ring, and the positive y-axis is defined as the vertical axis pointing upward. To take advantage of the cylindrical detector geometry, the azimuthal angle ϕ is defined around the z-axis, and the polar angle θ is defined with respect to the z-axis. In high energy physics, the polar angle is often represented in terms of pseudorapidity, which is defined as

$$\eta = -\ln(\tan(\frac{\theta}{2})). \tag{3.3}$$

The pseudorapidity is an approximation of the rapidity when the particle mass is negligible compared to its energy. The rapidity y is defined as

$$y = \frac{1}{2}\ln\frac{E + p_z}{E - p_z}. \tag{3.4}$$

The distance ΔR is defined as $\Delta R = \sqrt{(\Delta\eta)^2 + (\Delta\phi)^2}$ to evaluate the distance between two objects in the η-ϕ plane.

3.2.2 Inner Detector

The inner detector (ID), surrounded by a 2 T solenoid magnet, starts next to the LHC beam pipe. The ID is the main tracking system which is designed to reconstruct the trajectories of charged particles at $|\eta| < 2.5$ and full ϕ ranges using the positions measured by the Pixel detector, the Semiconductor strip tracker (SCT), and the Transition Radiation Tracker (TRT) in the outermost part. Figure 3.4 and Figure 3.5 show a cutaway view of the ID in the barrel and one side of an end-cap.

The Pixel detector is the closest detector to the IP. It consists of three layers in the barrel and two end-caps, covering a range of $|\eta| < 2.5$. The Insertable B-Layer (IBL) was installed during the LS1 at a radius of 33.25 mm, just about 8 mm from the beam pipe, as a fourth barrel layer. The Pixel detector provides on average three to four measurements

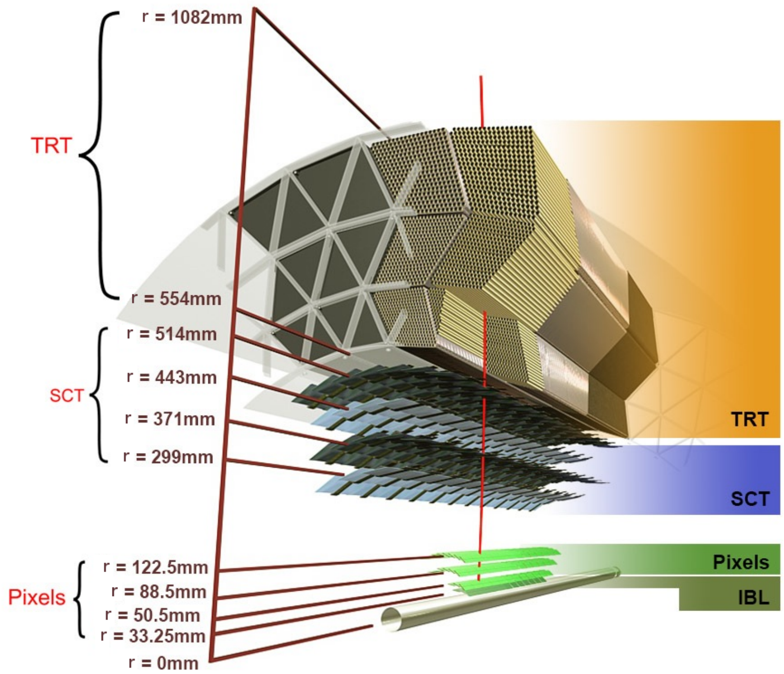

Figure 3.4. Schematic view of the inner barrel detectors.

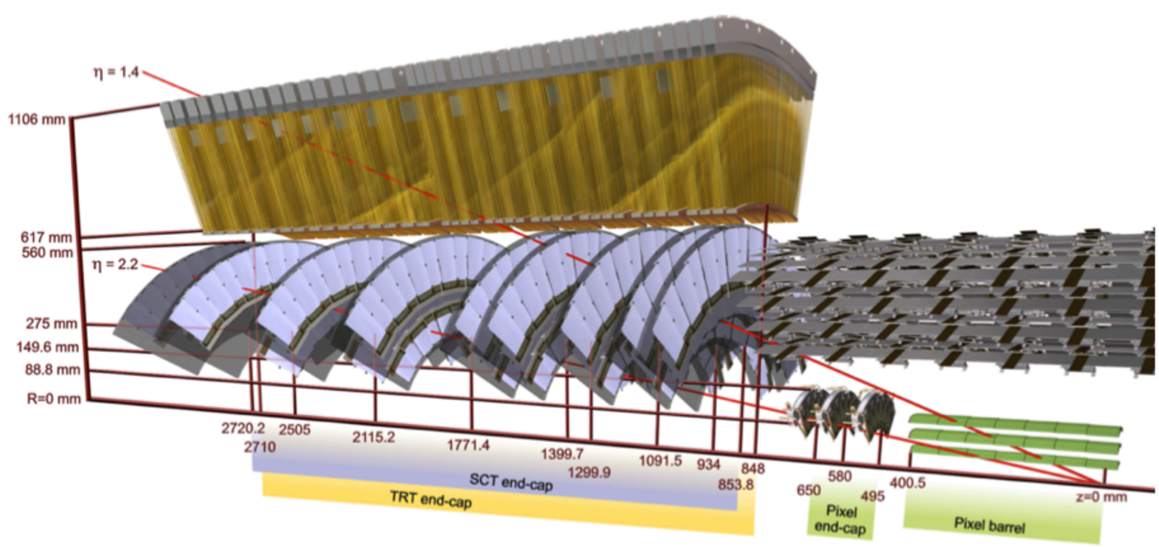

Figure 3.5. Schematic view of the inner end-cap detectors and Pixel and SCT barrel. The IBL installed during LS1 is not shown.

per track, and has a position resolution of 10 μm in the $r-\phi$ plane, and 115 μm in the z/r direction of the barrel/end-cap.

The SCT consists of four barrel and nine end-cap layers, covering a range of $|\eta| < 2.5$. Each SCT layer is composed of a double layer of silicon strips. It provides between four to nine measurements per track, and the measurements by a double layer has a position resolution of 17 μm in the $r-\phi$ plane, and 580 μm in the z/r direction of the barrel/end-cap.

The TRT is composed of about 300,000 straw tubes, covering a range of $|\eta| < 2.0$. A straw is a proportional drift tube with a diameter of 4 mm, filled with a mixture of Xe (or Ar), CO_2, O_2 gas in the ratio 70:27:3. The space between straws is filled with radiator material to produce transition radiation (TR) photon. The TRT provides about 35 measurements per track, and has a position resolution of 130 μm per straw tube. In addition to the tracking, the TRT also provides an electron identification using the signal from TR photons.

3.2.3 Calorimeter System

The calorimeter system, surrounding the ID, is designed to measure the energy of all particles except weakly interacting particles such as muons or neutrinos. Figure 3.6 shows the ATLAS calorimeter system, which is comprised of the electromagnetic (EM) calorimeter next to the ID, the hadronic calorimeters surrounding the EM calorimeters, and the forward calorimeters at large η.

The EM calorimeter is a high-granularity liquid-argon (LAr) sampling calorimeter, using lead as an absorber. It covers a range of $|\eta| < 3.2$, and is divided into one barrel and two end-cap regions. Figure 3.7 shows a barrel module of the LAr EM calorimeter. It is composed of three layers with different thicknesses and $\Delta\eta \times \Delta\phi$ granularities of the calorimeter cells. The second layer provides most of the energy measurements and has fine granularity in both η and ϕ directions. The total thickness of the EM calorimeter is larger than 22 radiation lengths (X_0), which allows to stop high p_{T} electrons and photons.

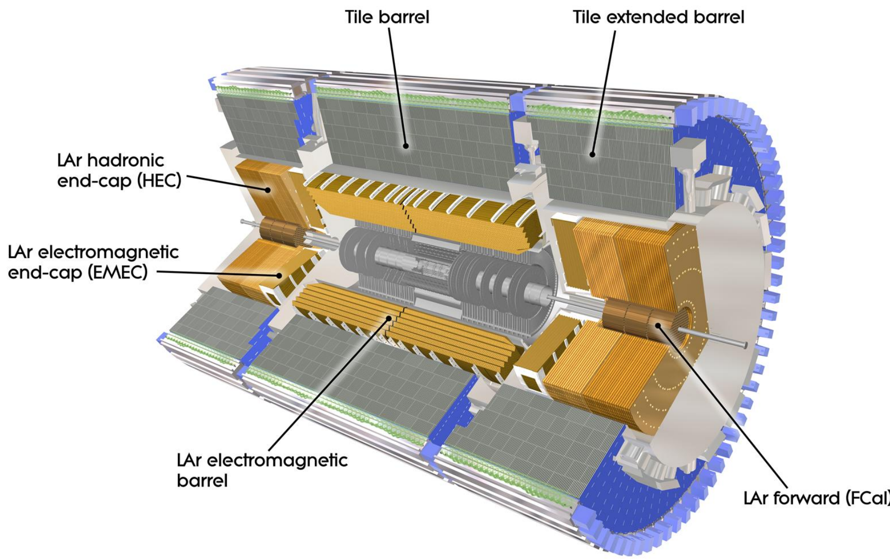

Figure 3.6. The cutaway view of the ATLAS calorimeter system.

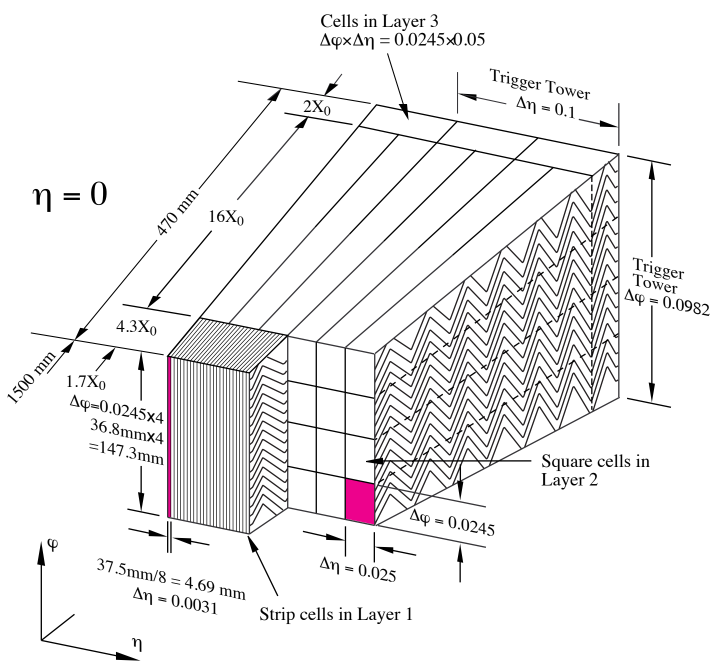

Figure 3.7. Schematic view of a barrel module of the LAr EM calorimeter.

The hadronic calorimeter is designed for energy measurement of jets and hadronically interacting particles, covering a range of $|\eta| < 3.2$. It consists of the Tile calorimeter in barrel and the Hadronic end-cap calorimeter in two end-cap regions. The Tile and the Hadronic end-cap calorimeters are sampling calorimeters using iron and copper as absorber, respectively. The total thickness of about 10 nuclear interaction length (λ) provides a good energy resolution for high energy jets and a significant reduction of punch-through to the muon system. The forward calorimeter covers very forward region, $3.1 < |\eta| < 4.9$. It consists of three layers, the first for electron and photon measurements and the other two for hadrons.

3.2.4 Muon Spectrometer

The Muon Spectrometer (MS) is the outermost system which surrounds the calorimeters. The MS is designed to measure the trajectories of muons as other detectable particles are

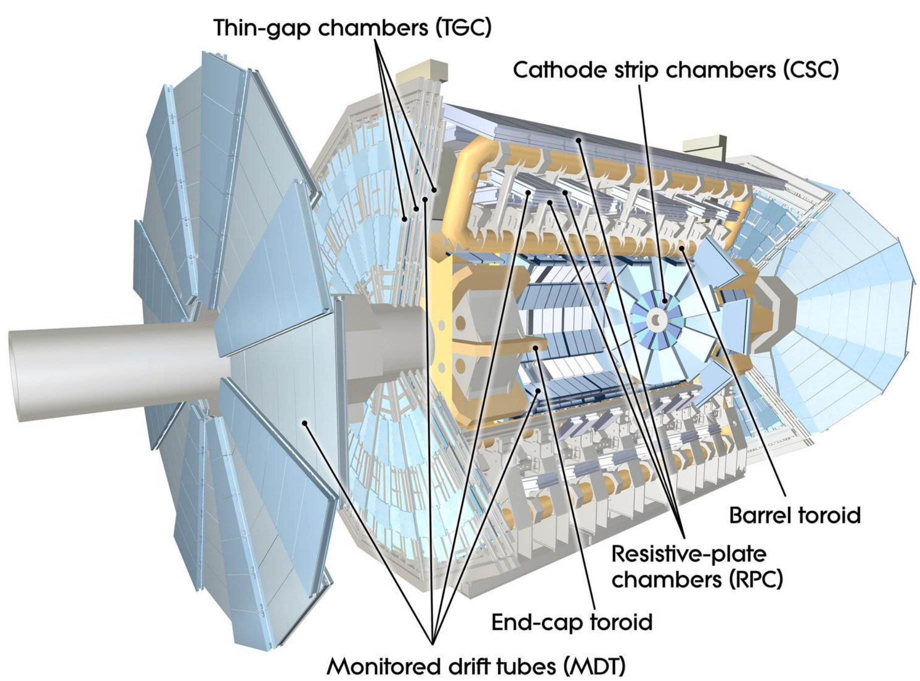

Figure 3.8. The cutaway view of the ATLAS muon system.

mostly stopped by the calorimeters. The MS consists of a barrel and two end-cap toroid magnets to bend the muon trajectories and the muon chambers for precision tracking and triggering as shown in Figure 3.8. The Resistive Plate Chambers (RPC, three doublet layers for $|\eta| < 1.05$) and the Thin Gap Chambers (TGC, one triplet layer followed by two doublets for $1.0 < |\eta| < 2.4$) are mainly used for triggering. A precision measurement of the track with pseudorapidity up to 2.7 is provided by three layers of the Monitored Drift Tubes (MDTs), with each chamber providing six to eight η measurements along the trajectory. For $|\eta| > 2$, the first layer is instrumented with the Cathode Strip Chambers (CSCs) instead of MDTs due to high radiation level in this region.

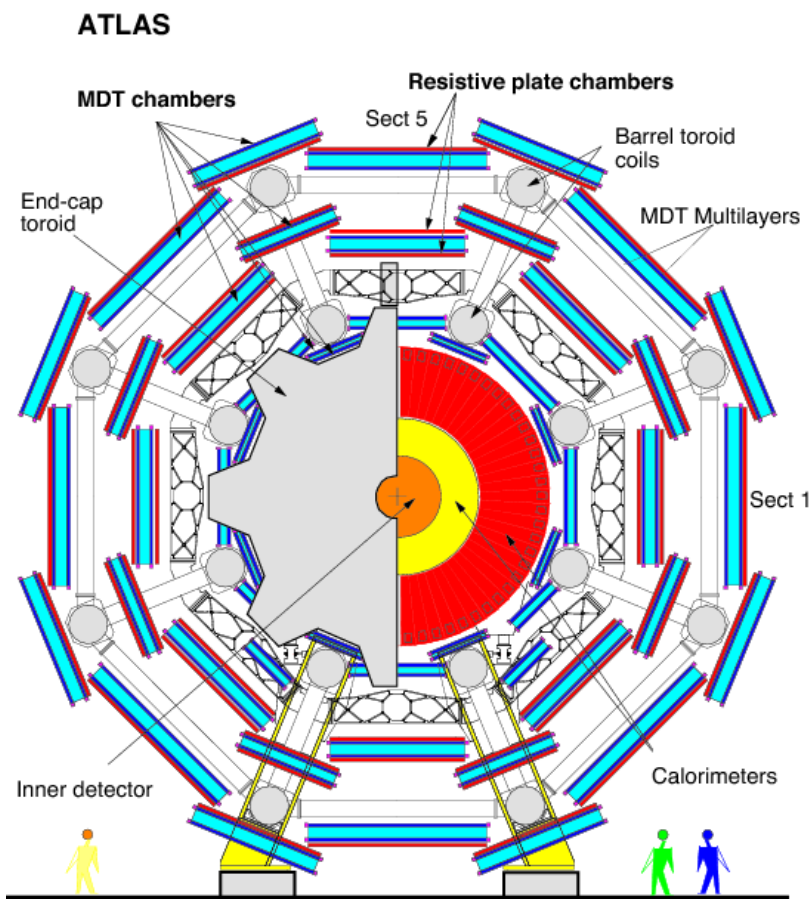

Figure 3.9. Schematic view of the muon spectrometer in the x-y projection [25].

4. Reconstruction of Physics Objects

The ATLAS detector measure traces left in each sub-detector by particles which traverse the detector volume. The transformation of the raw detector signal into high-level physics objects such as electrons or muons is collectively referred to as reconstruction. Figure 4.1 shows a schematic of the signatures from various particles in the ATLAS detector. In this chapter, track and calorimeter cluster reconstructions are briefly discussed in Section 4.1

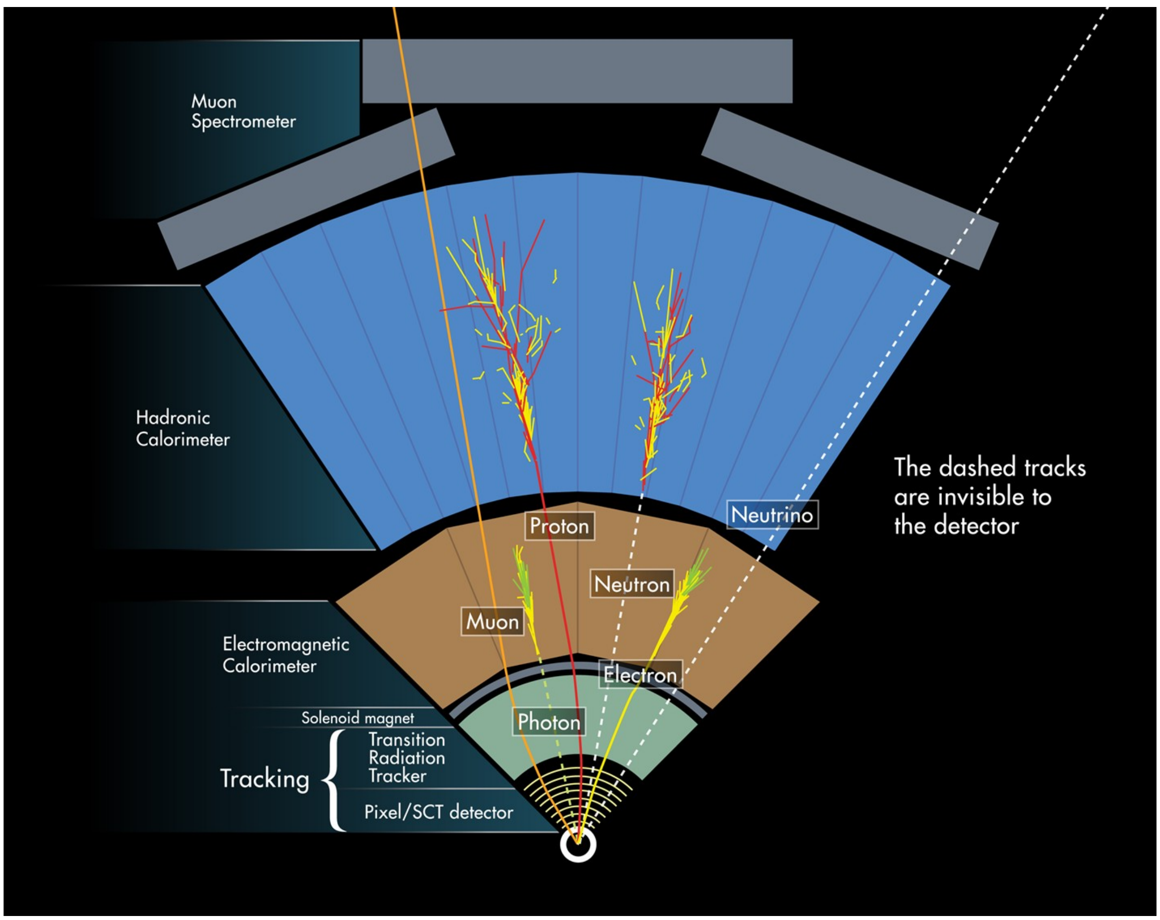

Figure 4.1. Schematic cutaway of the ATLAS detector with the signatures from various particles.

and Section 4.2, respectively, as particle trajectories (tracks) and calorimeter clusters are the basic ingredients for the reconstruction of high-level physics objects. Subsequently, reconstruction and identification of high-level physics objects are discussed in Section 4.3.

4.1 Track Reconstruction

The ATLAS track reconstructions are performed separately in the ID and the MS. The reconstruction in the ID is the primary track reconstruction for charged particles, and the reconstruction in the MS is used as a dedicated track measurement for muons.

4.1.1 Track reconstruction in the ID

Track reconstruction of the ID consists of several algorithms [26]. For brevity, only the main algorithm, the inside-out track finding, is described. It consists of the following sequence of steps:

- Formation of space-points: The first step is the creation of clusters in the Pixel and SCT, and drift circles in the TRT. Then, clusters and drift circles are transformed into 3D space-points. The space-points in the Pixel and SCT barrel layers from a $t\bar{t}$ event are shown as black circles in Figure 4.2.

- Track finding seeded by space-points: Sets of three space-points form a seed, which defines a circular track segment, either Pixel-only, SCT-only or Mixed seed. Figure 4.2 shows the Pixel-only seeds in red lines and the others in blue lines. Seeds which pass the initial transverse momentum and impact parameter resolution (defined in Section 4.1.3) cuts are also required to match a fourth space-point that is compatible with the particle's trajectory estimated from the seed. A combinatorial Kalman filter [27] is then used to complete track candidates within the silicon detector.

- Ambiguity solving: Track candidates are ranked based on track score, favoring tracks with a higher score. In general, each hit associated with the track leads to a better score value to favor fully reconstructed tracks rather than small track segments. Track

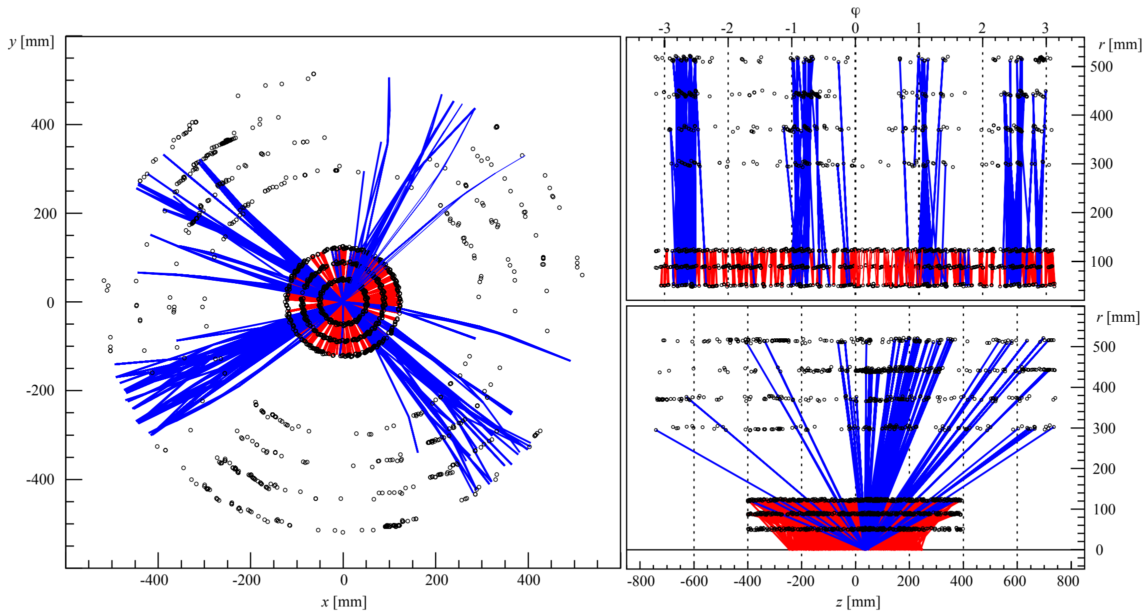

Figure 4.2. Space-points and track finding seeds in the Pixel and SCT barrel layers from a $t\bar{t}$ event. The IBL at a radius of 33.25 mm is missing in the figure.

candidates are rejected if they fail to meet basic quality criteria such as goodness of the track fit. A neural network clustering algorithm has been implemented for the Pixel clusters assigned to multiple track candidates in order to separate multiple particles within a merged cluster in dense environments.

- TRT extension: Finally, the track candidates are extended to the TRT if there is a valid set of matching drift circles. Then, the track is refitted using all ID information to improve momentum resolution. The TRT extended tracks from the same $t\bar{t}$ event are shown in Figure 4.3.

In addition to the inside-out track finding algorithm, the outside-in track finding algorithm is also implemented in order to reconstruct tracks from photon conversion or secondary decay vertices. The TRT segments from the outside-in track finding algorithm are shown in Figure 4.3.

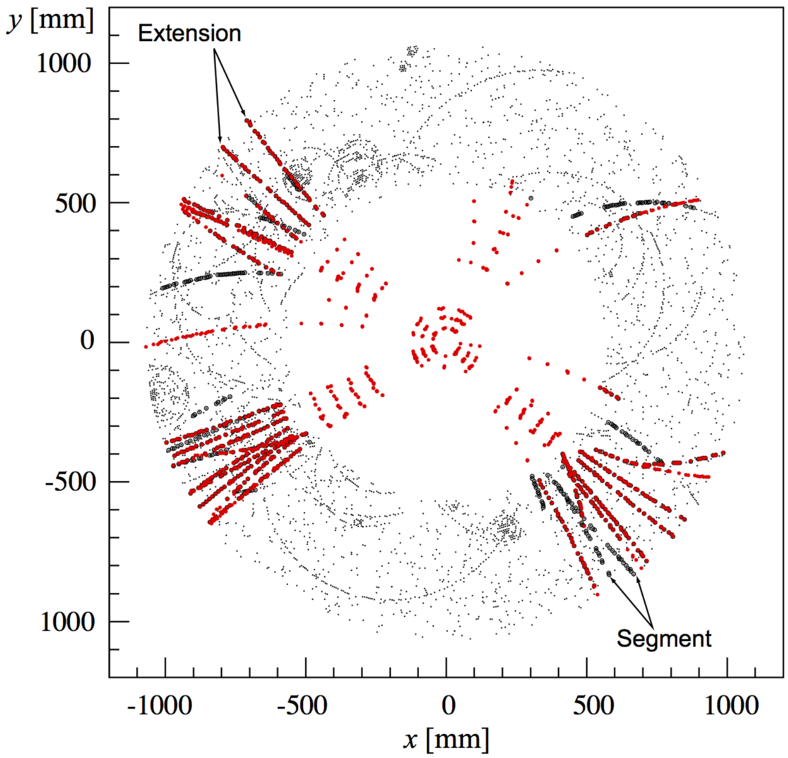

Figure 4.3. TRT extenstions in red full circles and TRT segments in black full circles in the ID barrel for the same $t\bar{t}$ event shown in Figure 4.2. The IBL at a radius of 33.25 mm is missing in the figure.

4.1.2 Track reconstruction in the MS

Track reconstruction is performed independently in the MS, and the reconstructed track in the MS is further utilized for muon reconstruction which is discussed in Section 4.3.2. The track reconstruction in the MS is described in the following sequence of steps:

- Hit pattern in the chambers: Search for hit patterns consistent with tracks inside each layer of the MDT chambers. A Hough transform is used for the chambers in the toroid magnets, where tracks have curved trajectories.

- MDT segment: A straight-line fit is performed to the hits found in each layer to form a MDT segment.

- Track finding: Track candidates are built by fitting hits from segments. A segment-seeded combinatorial search is performed from the middle layer where more trigger hits from RPC or TGC are available. The search is then extended to the segments from the outer and inner layers. At least two matching segments are required to build a track, except in the barrel-endcap transition region.

- Overlap removal: The same segment can be initially used to build several track candidates, but an overlap removal algorithm selects the best candidate. The segment can be shared between two tracks if no hits are shared in the outermost layer.

- Track refit: Finally, all hits on each track candidate are fitted using the ATLAS global χ^2 fit [28]. A track candidate is accepted if the χ^2 fit satisfies the selection criteria.

4.1.3 Track Parameters

Once a track is reconstructed, ATLAS uses the following representation for the track parameters:

$$\mathbf{x} = (d_0, z_0, \phi_0, \theta, q/p) \tag{4.1}$$

where d_0 and z_0 are the transverse and longitudinal impact parameters of the track with respect to the origin, ϕ_0 is the azimuthal angle of the track at the perigee, θ is the polar angle, and q/p is the inverse momentum multiplied by the charge. Figure 4.4 shows a schematic of each track parameter in the ATLAS coordinate system, which is discussed in Section 3.2.

In the analysis of this thesis, the following variables, based on the track parameters, are used:

- d_0 significance is defined as $|d_0/\sigma_{d_0}|$, where σ_{d_0} is defined by the error of the track fit. The σ_{d_0} changes with the track $p_{\mathrm{T}}$and is about 20 μm for tracks with $p_{\mathrm{T}} > 10$ GeV.

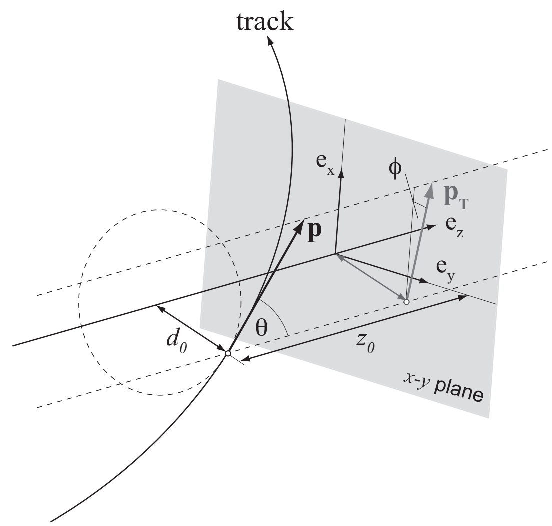

Figure 4.4. Schematic of the transverse and longitudinal impact parameters in the ATLAS coordinate system.

- $|\Delta z_0 \sin\theta|$ is the distance of closest approach between the track and the primary vertex in the x-z plane, where $|\Delta z_0|$ is defined as the distance between the track and the primary vertex on the z-axis.
- Pseudorapidity (η) is defined in Section 3.2.

4.2 Calorimeter Cluster Reconstruction

Energy deposits in the calorimeters by electrons, photons, τ-leptons, muons, jets, and other particles form clusters, which are reconstructed by clustering algorithms. Previously, ATLAS used two types of clustering algorithms, the sliding-window algorithm [29] and the topological cell clustering algorithm, until the data processed in 2016. The sliding-window algorithm, which was the primary algorithm for electron and photon cluster reconstructions, is deprecated in 2017 and the topological algorithm is used for the reconstruction of all objects.[1] Thus, the data used in the analysis of this thesis is processed only with the topological clustering algorithms.

4.2.1 Topological Cluster

The topological cluster (topo-cluster) is formed by three-dimensional collection of calorimeter cell signals which are generated by particle showers. The strength of the calorimeter cell signal is represented by the cell signal significance ς_{cell}^{EM}, which is defined as

$$\varsigma_{\mathrm{cell}}^{\mathrm{EM}} = \frac{E_{\mathrm{cell}}^{\mathrm{EM}}}{\sigma_{\mathrm{noise,cell}}^{\mathrm{EM}}} \tag{4.2}$$

where $E_{\mathrm{cell}}^{\mathrm{EM}}$ is the cell energy and $\sigma_{\mathrm{noise,cell}}^{\mathrm{EM}}$ is the expected cell noise. The expected cell noise is estimated from the electronic noise and the noise from pile-up. Topo-clusters are built by a growing-volume algorithm which utilizes three thresholds for the seeding, growth, and boundary:

1. Select all cells which exceed the seed threshold ($|\varsigma_{cell}^{EM}| > 4$). Then seed cells are ordered in decreasing ς_{cell}^{EM}.

2. The cells which neighbour a seed cell and exceed the growing threshold ($|\varsigma_{cell}^{EM}| > 2$) or the boundary threshold ($|\varsigma_{cell}^{EM}| > 0$) are combined with the seed cell to form a proto-cluster. A neighbouring cell is defined as an adjacent cell in a given calorimeter layer or in adjacent layer with an overlap in the $\eta - \phi$ plane.

3. Step 2 is iteratively applied until the last iteration with only boundary cells.

4. The proto-clusters with two or more local maxima are split between the signal peaks in all three spatial dimensions. A local signal maximum is required to have $E_{\mathrm{cell}}^{\mathrm{EM}} >$ 500 MeV and satisfy the basic topological requirements. If one cell is shared by two split clusters, respective energies are defined as the $E_{\mathrm{cell}}^{\mathrm{EM}}$ multiplied by geometrical

[1] The sliding-window algorithm was used for electron and photon reconstructions until the ATLAS Offline Software release 20.7, and the topological algorithm supersedes the sliding-window algorithm since the ATLAS Offline Software release 21.

weights, which are calculated from the distance of the cell to the center of gravity of of the two clusters (d_1, d_2), as defined by:

$$w^{\text{geo}}_{\text{cell},1} = \frac{E^{\text{EM}}_{\text{clus},1}}{E^{\text{EM}}_{\text{clus},1} + rE^{\text{EM}}_{\text{clus},2}}, \qquad w^{\text{geo}}_{\text{cell},2} = 1 - w^{\text{geo}}_{\text{cell},1} \tag{4.3}$$

where $r = \exp(d_1 - d_2)$.

5. The final proto-clusters after splitting are the topo-clusters used for the reconstruction of high-level physics objects.

The cluster energy is measured on the electromagnetic (EM) energy scale, which signifies the energy deposit by electrons and photons are correctly measured but not for hadrons as they can generate a distant sub-showers from inelastic interactions. This feature is referred to as non-compensating calorimeter response. Hence, the corrections are applied to the cluster energy based on the calibration which includes the effects of the non-compensating calorimeter response to hadrons, accidental signal losses due to the clustering algorithm, cluster-by-cluster fluctuations, and energy lost in inactive material. This calibration is referred to as local hadronic cell weighting (LCW) calibration, and is of particular importance for jets and τ-leptons. A detail description of the topological cell clustering is given in reference [30].

4.3 High-level Physics Objects

The reconstruction and identification of higher level physics objects are discussed for electron, muon, jet, and missing transverse momentum as these are high-level physics objects used in the analysis of this thesis.

4.3.1 Electrons

Electrons and positrons, which are collectively referred to as electrons, are measured in the ID and the EM calorimeter as shown in Figure 4.1. Electron measurements in the region of $|\eta| < 2.47$, which corresponds to the ID coverage, are discussed.

Electron Reconstruction

Reconstruction of electron candidates is briefly described in the following sequence of steps:

- Electron seed-cluster reconstruction: Topo-clusters which contain more than 50% of their total energy in the EM calorimeter are selected among the topo-clusters discussed in Section 4.2.1. EM cluster regions-of-interest (ROIs) are then defined as a cone of $\Delta R = 0.3$ around the seed cluster barycenter.

- Electron supercluster reconstruction: The satellite clusters formed by low energy photon radiation due to bremsstrahlung or topo-cluster splitting are added to the EM topo-clusters. This is referred to as the superclusters algorithm [31] which improves the electron energy resolution up to 40% and was implemented in 2017 as mentioned in Section 4.2.

- Electron-track candidate reconstruction: In addition to the track reconstruction described in Section 4.1, an electron-specific reconstruction is performed for track candidates within the EM cluster ROI in order to recover electron tracks by allowing up to 30% of energy losses from bremsstrahlung. Tracks loosely matched to EM clusters are defined as electron-track candidates.

- Electron-candidate reconstruction: Electron-track candidates are refitted with the Gaussian Sum Filter (GSF) algorithm [32], which is a non-linear generalization of the Kalman filter algorithm, in order to have a better estimate of the electron track parameters. An electron candidate is then defined if at least one track is matched to the seed cluster.

The four-momentum of electron candidate is constructed from the EM cluster for the energy and the track parameters for the ϕ and η. The transverse momentum is calculated from the energy and the η with the electron mass hypothesis. A detail description of the electron reconstruction is given in reference [33].

Electron Identification

Electron candidates originate from either real prompt electrons, which are produced from hard-scatterings, or background objects which include hadronic jets and non-prompt electrons from photon conversions and heavy-flavor decays. In order to reject as much background as possible while maintain high efficiency for prompt electrons, electron identification is performed using discriminating variables described in Table 4.1. The full descriptions of each discriminating variable can be found in reference [34]. A likelihood-based (LH) method, which is one of the multivariate analysis (MVA) techniques [35], is used for electron identifications. It utilizes the signal and background probability density functions (PDFs) of the discriminating variables listed in Table 4.1 except variables in the "Additional cuts". A probability is calculated for a given electron to be signal or background based on the PDFs. The signal (S) and background (B) probabilities are then combined into a discriminant $d_{\mathcal{L}}$:

$$d_{\mathcal{L}} = \frac{\mathcal{L}_S}{\mathcal{L}_S + \mathcal{L}_B}, \qquad \mathcal{L}_{S(B)}(\vec{x}) = \prod_{i=1}^{n} P_{S(B),i}(x_i) \tag{4.4}$$

where $\vec{x}$ is the vector of discriminating variable values and $P_{S(B),i}(x_i)$ is the value of the signal probability density function of the i^{th} variable evaluated at $\vec{x}$. The following simple selections are then applied for the variables in the "Additional cuts": $n_{\text{Blayer}} = 1$, $n_{\text{Pixel}} \geq 2$, and $n_{\text{Si}} \geq 7$.

ATLAS provides three levels of electron identification operating points which are referred to as *Loose*, *Medium* and *Tight* operating point in order of increasing background rejection.

Type	Variable name	Description
Calorimeter variables	R_{had}	Ratio of E_{T} leaked into the hadronic calorimeter
	f_3	Fraction of energy in the third layer to the total energy
	R_η	η direction leakage in the second layer
	R_ϕ	ϕ direction leakage in the second layer
	W_{η^2}	Lateral shower width in the second layer
	f_1	Ratio of the energy in the first layer to the total energy in the EM cluster
	E_{ratio}	Ratio of the energy difference between the largest and second largest over the sum of these energies in the first layer
Track variables	d_0	Discussed in Section 4.1.3
	d_0 significance	Discussed in Section 4.1.3
	$\Delta p/p$	Momentum lost by the track between the perigee and the last measurement point over the original momentum
	TRT PID	Likelihood probability based on transition radiation in the TRT
Track-cluster matching	$\Delta\eta_1$	$\Delta\eta$ between the cluster position in the first layer and the extrapolated track
	$\Delta\phi_{Res}$	$\Delta\phi$ between the cluster position in the second layer and the track extrapolated from the perigee
Additional cuts	n_{Blayer}	Number of hits in the IBL
	n_{Pixel}	Number of hits in the Pixel
	n_{Si}	Number of hits in the Pixel and SCT

Table 4.1. List of discriminating variables for electron identification.

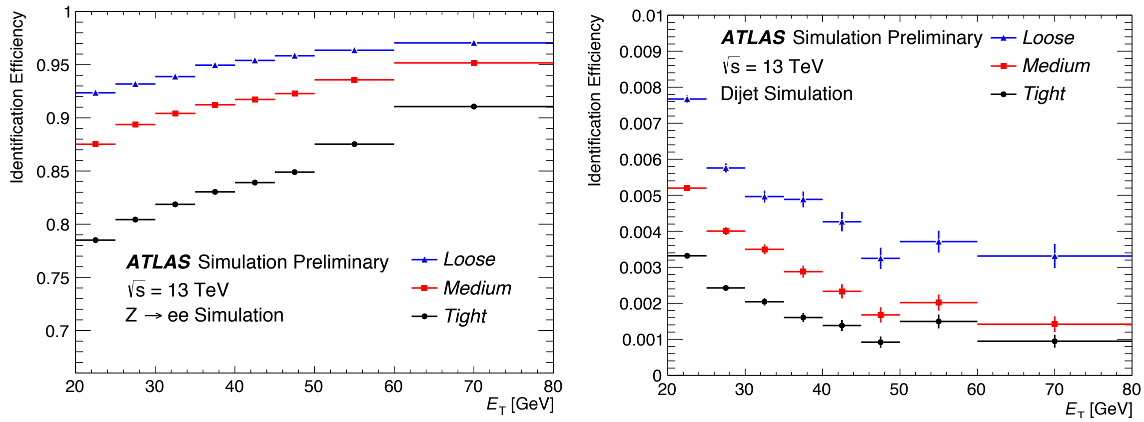

Figure 4.5. The electron identification efficiencies measured from reconstructed electrons in the MC simulation for $Z \rightarrow ee$ (left) and dijet (right) samples.

The *Loose*, *Medium* and *Tight* operating points are defined such that *Medium* electrons are a subset of *Loose* electrons, and *Tight* electrons are a subset of *Medium* electrons. The operating points are set to have the signal (background) efficiencies for electron with E_{T} = 25 GeV in the range from 78 to 90% (0.3 to 0.8%) and increase (decrease) with E_{T} as shown in Figure 4.5.

Electron Isolation

In addition to the identification criteria, an isolation requirement further discriminates prompt electrons from non-isolated electron candidates such as electrons from heavy-flavor decays and misidentified light quark jets. The discriminating variables are designed for calorimeter-based and track-based isolations:

- calorimeter-based isolation, $E_{\mathrm{T}}^{\mathrm{cone}0.2}$: Sum the E_{T} in the calorimeter cells within a cone of $\Delta R = 0.2$ around the electron, then subtract the contribution within $\Delta\eta \times \Delta\phi = 0.125 \times 0.175$ around the electron cluster barycenter. Contributions from pile-up and underlying event are corrected on an event-by-event basis using the ambient energy-density technique [36].

- track-based isolation, $p_{\mathrm{T}}^{\mathrm{varcone0.2}}$: Sum of p_{T} of all tracks from the primary vertex within a cone of $\Delta R = \min(0.2, 10\ \mathrm{GeV}/E_{\mathrm{T}})$ around the electron, then subtract the p_{T} of electron.

Various operating points are designed using the relative isolation variables, which are defined as $E_{\mathrm{T}}^{\mathrm{cone0.2}}/E_{\mathrm{T}}$ and $p_{\mathrm{T}}^{\mathrm{varcone0.2}}/E_{\mathrm{T}}$. The operating points are set by the efficiency of

Operating point	$E_{\mathrm{T}}^{\mathrm{cone0.2}}/E_{\mathrm{T}}$	$p_{\mathrm{T}}^{\mathrm{varcone0.2}}/E_{\mathrm{T}}$	total efficiency
LooseTrackOnly	-	99%	99%
Loose	99%	99%	$\sim$ 98%
Tight	96%	99%	$\sim$ 95%
Gradient	0.1143%$\times E_{\mathrm{T}}$ + 92.14%	0.1143% $\times$ E_{T} + 92.14%	90/99% at 25/60 GeV
GradientLoose	0.057% $\times$ E_{T} + 95.57%	0.0057% $\times$ E_{T} + 95.57%	95/99% at 25/60 GeV

Table 4.2. The electron isolation operating points which are set by the efficiency of the isolation requirement.

the isolation requirement, which can be either constant or as a function of E_{T} as shown in Table 4.2. In addition to the operating points shown in Table 4.2, the fixed cut operating points are also designed for physics analyses using low E_{T} electrons. A more detailed description of the electron isolation is given in reference [34].

Corrections to Electron

Corrections are applied on the energy scale, energy resolution, and efficiencies in order to achieve the optimal performance and ideally the same response from collision data and MC simulation. The correction on the energy scale is applied to both data and MC [37]. The data is corrected for the equal response throughout the detector by considering various sources such as the longitudinal EM calorimeter layers and High-Voltage (HV) inhomogeneities. The MC-based energy correction is applied to both data and MC, where the calibration constants are determined using a multivariate algorithm (MVA). The energy resolution is corrected in MC in order to reproduce the energy resolution observed in data. Electron efficiency is measured for both data and MC from $J/\psi \rightarrow ee$ for the low E_{T} range and $Z \rightarrow ee$ above 15 GeV. The efficiency is measured as a function of E_{T} and η for each stage which includes reconstruction, trigger, identification, isolation. The total efficiency for a single electron is defined as:

$$\epsilon_{\mathrm{total}} = \epsilon_{\mathrm{reconstruction}} \times \epsilon_{\mathrm{trigger}} \times \epsilon_{\mathrm{identification}} \times \epsilon_{\mathrm{isolation}}. \tag{4.5}$$

The ratio between data and MC total efficiencies is then used as a scale factor for electrons in MC.

4.3.2 Muons

Muon Reconstruction

Reconstruction of muon candidates is performed using the information provided by the MS, ID, and calorimeters. The following muon types are defined depending on which subdetectors are used in reconstruction:

- Combined (CB) muon: An ID-MS combined track is formed by a global refit which uses hits from reconstructed tracks in the ID and MS as discussed in Section 4.1. Most muons are reconstructed from the MS and then extrapolated to a matched ID track.
- Segment-tagged (ST) muon: A track in the ID is extrapolated to at least one MDT segment. ST muons are mostly low p_{T} or fall in regions with reduced MS acceptance.
- Calorimeter-tagged (CT) muon: A track only with an energy deposit in the calorimeter, which is compatible with a minimum-ionizing particle. This type is designed to recover muons in the region of $|\eta| < 0.1$ as muon chambers are absent in this region, which is used for cables and services.

- Extrapolated (ME) muon: A MS track with a loose requirement on its impact parameter with respect to the interaction point (IP). ME muons are mainly used for muons in the region of $2.5 < |\eta| < 2.7$, which is outside of the ID coverage.

Muon Identification

Muon candidates originate from either prompt muons, which are produced from hard-scattering, and backgrounds such as muons from pion and kaon decays. The main feature of background muons from hadron decays is a distinctive kink topology in their tracks, which leads to a poor fit quality of the track and a change in the momentum. Thus, the following discriminating variables are used for identification of CB tracks:

- q/p significance: The absolute value of the difference between the q/p in the ID and MS divided by the sum in quadrature of each uncertainty.
- The absolute value of the difference between the p_{T} in the ID and MS divided by the p_{T} of the combined track.
- The normalized χ^2 of the combined track fit.

Additional track quality requirements are applied to assure a robust momentum measurement such as the number of hits in the ID and MS.

ATLAS provides four levels of muon identification selections which are referred to as *Loose*, *Medium*, *Tight*, and *High*-p_{T}. As in the electron identification, the *Medium* muons are a subset of *Loose* muons, and *Tight* muons are a subset of *Medium* muons.

- Medium muon: CB and ME muons are used. The CB muons are required to have more than 3 hits in at least two MDT layers except for tracks in the region of $|\eta| < 0.1$. The ME muons are required to have at least three MDT/CSC layers, and are used only in the region of $2.5 < |\eta| < 2.7$. The q/p significance is required to be less than seven.
- Loose muon: All muon types are used. This selection yields maximal muon efficiency as was specificially designed for Higgs boson candidates in the four-lepton final state.

CT and ST muons are restricted to the region of $|\eta| < 0.1$. In the region of $|\eta| < 2.5$, about 98% of the *Loose* muons are CB muons.

- Tight muon: Only CB muons are used. More stringent requirements are applied than the *Medium* muons, which allow maximal purity at the cost of some efficiency especially $p_{\mathrm{T}} < 20$ GeV.

- High-p_{T} muon: Only CB muons are used, which pass the *Medium* selection and have at least three hits in three MS stations. This selection maximizes the momentum resolution for tracks with $p_{\mathrm{T}} > 100$ GeV. The p_{T} resolution improves about 30% above 1.5 TeV. Specific regions of the MS where the alignment is suboptimal are vetoed as a precaution.

The efficiencies of muon reconstruction for the identification selections are evaluated in the region of $|\eta| < 2.5$ from W MC for prompt muons and $t\bar{t}$ MC for background muons from hadrons, and the efficiencies in the region of $4 < p_{\mathrm{T}} < 20$ GeV and $20 < p_{\mathrm{T}} < 100$ GeV are shown in Table 4.3. The efficiencies are about 90 to 98% for prompt muons with

	$4 < p_{\mathrm{T}} < 20$ GeV		$20 < p_{\mathrm{T}} < 100$ GeV	
Selection	ϵ_{μ}^{MC}	$\epsilon_{Hadrons}^{MC}$	ϵ_{μ}^{MC}	$\epsilon_{Hadrons}^{MC}$
Loose	96.7	0.53	98.1	0.76
Medium	95.5	0.38	96.1	0.17
Tight	89.9	0.19	91.8	0.11
High-p_{T}	78.1	0.26	80.4	0.13

Table 4.3. Muon reconstrution efficiencies for the identification selections evaludated in the region of $|\eta| < 2.5$ from W MC for prompt muons and $t\bar{t}$ MC for background muons from hadrons.

background efficiency below 1% for all identification selections except High-p_{T} selection. The High-p_{T} selection is designed for physics analyses which require good p_{T} resolutions for high p_{T} muons.

Muon Isolation

In addition to the identification selection, an isolation requirement further discriminates prompt muons from backgrounds such as muons inside jets. The following discriminating variables are designed:

- track-based isolation, $p_{\mathrm{T}}^{\mathrm{varcone30}}$: Sum the p_{T} of all tracks within a cone of $\Delta R = \min(0.3,\ 10\ \mathrm{GeV}/E_{\mathrm{T}})$ around the muon, then subtract the p_{T} of the muon.
- calorimeter-based isolation, $E_{\mathrm{T}}^{\mathrm{topocone20}}$: Sum the E_{T} of topological clusters in a cone of $\Delta R = 0.2$ around the muon, then subtract the contribution from the expected energy deposit of the muon. Contribution from pile-up and underlying event is corrected on an event-by-event basis using the ambient energy-density technique [36].

Similar to the electron isolation, operation points are designed using the relative isolation variables, which are defined as $p_{\mathrm{T}}^{\mathrm{varcone30}}/p_{\mathrm{T}}$ and $E_{\mathrm{T}}^{\mathrm{topocone20}}/p_{\mathrm{T}}$. The operating points are set by the efficiency of the isolation requirement, which can be either constant or as a function of p_{T} as shown in Table 4.4. In addition to the operating points shown in Table 4.4, the fixed cut operating points are also designed for physics analyses using low p_{T} muons. A more detailed description of the muon isolation is given in reference [38].

Operating point	Discriminating variable(s)	Total efficiency
LooseTrackOnly	$p_{\mathrm{T}}^{\mathrm{varcone30}}/p_{\mathrm{T}}$	99%
Loose	$p_{\mathrm{T}}^{\mathrm{varcone30}}/p_{\mathrm{T}}$, $E_{\mathrm{T}}^{\mathrm{topocone20}}/p_{\mathrm{T}}$	99%
Tight	$p_{\mathrm{T}}^{\mathrm{varcone30}}/p_{\mathrm{T}}$, $E_{\mathrm{T}}^{\mathrm{topocone20}}/p_{\mathrm{T}}$	96%
Gradient	$p_{\mathrm{T}}^{\mathrm{varcone30}}/p_{\mathrm{T}}$, $E_{\mathrm{T}}^{\mathrm{topocone20}}/p_{\mathrm{T}}$	90/99% at 25/60 GeV
GradientLoose	$p_{\mathrm{T}}^{\mathrm{varcone30}}/p_{\mathrm{T}}$, $E_{\mathrm{T}}^{\mathrm{topocone20}}/p_{\mathrm{T}}$	95/99% at 25/60 GeV

Table 4.4. The muon isolation operating points which are set by the efficiency of the isolation requirement.

Corrections to Muon

Similar to the electron, corrections are applied on the momentum scale, momentum momentum resolution, and efficiencies. The muon momentum scale and resolution are measured using $J/\psi \to \mu\mu$ and $Z \to \mu\mu$ decays for data and MC simulation, and then corrections are applied to the simulated muon momentum to match the invariant mass distributions in data.

4.3.3 Jets

Jets are made of collimated showers of hadrons from various origins such as quarks or gluons. In this chapter, jets which are relevant to the analysis of this thesis are briefly discussed.

Jet Reconstruction

Jet reconstruction can be divided into three primary steps: input constituents for the jet reconstruction, jet algorithm, and finally jet grooming for large-R jets. Small-R jets are used to reconstruct non-top-quarks and gluons, and large-R jets are instead used to reconstruct the decays of massive hadronically decaying particles, such as W and Z bosons, and top quarks. The following introduces small-R jets reconstructed with two different inputs using the same jet algorithm.

- EMTopo Jet: Jets are reconstructed from calibrated topo-clusters at the EM scale using the anti-k_t algorithm [39] with a distance parameter $R = 0.4$. Jets are then calibrated using the EM+JES scheme [40] with a correction for pile-up [41].

- Particle Flow (or PFlow) Jet: Jets are reconstructed from measurements in the calorimeter and the ID using the anti-k_t algorithm with a distance parameter $R = 0.4$. The PFlow algorithm utilizes charged tracks which are associated with the primary vertex as charged constituents and topo-clusters after subtraction of a contribution from charged tracks as neutral constituents. This strategy provides improvements of the jet energy resolution, reduced pile-up jet rates, and a more accurate jet direction estimation in the $\eta - \phi$ plane. The PFlow algorithm is described in detail in reference [42].

Jet Identification

Jets originate from either a hard scatter collision or other backgrounds. Background jets can arise from either non-collision origins and pile-up collisions.

The main sources of non-collision background are the beam-induced background (BIB), cosmic-ray showers, and calorimeter noise [43]. The BIB is due to proton losses upstream of the interaction point. The rate of BIB is proportional to the beam current and depends on the operation conditions of the LHC. Cosmic-ray showers produced in the atmosphere can overlap with proton collision events. Permanently noisy calorimeter cells are masked out before jet reconstruction, while sporadically noisy cells are masked on an event-by-event basis. ATLAS provides removal of such jets at an object-level or event-level. Event-level cleaning is preferred as the presence of a corrupted jet in an event can affect other objects, especially the $E_{\mathrm{T}}^{\mathrm{miss}}$ calculation and the topo-cluster reconstruction. ATLAS provides the *Loose*/*Tight* selection working points which are designed to provide an efficiency of selecting jets from proton-proton collisions above 99.5%/95% for $p_{\mathrm{T}} > 20$ GeV.

Jets from pile-up collisions are filtered using a tagging algorithm, which is referred to as the jet vertex tagging (JVT) algorithm [44], to select hard-scatter jets. The JVT algorithm provides a likelihood discriminant, which ranges from 0 (pile-up-like) to 1 (hard-scatter-like), for each jet with matched tracks. The EMTopo jets are required to have JVT > 0.59 for jets with $p_{\mathrm{T}} < 60$ GeV and $|\eta| < 2.4$. The PFlow jets are required to have JVT > 0.2 for the entire phase space. The selection criteria show the same pile-up jet rejection for both EMTopo jets and PFlow jets.

Corrections to Jet

Corrections to the jet energy scale are applied to both data and MC. The jet energy scale (JES) calibration [40] consists of several stages derived from a combination of MC-based methods and *in situ* techniques. The MC-based correction is applied to the four-momentum of reconstructed jets from the simulated particles within the jet. *In situ* techniques are used to measure the difference between data and MC, and the correction on the residual is applied to only data.

4.3.4 Missing Transverse Momentum

The initial momentum carried by a pair of colliding partons in the protons is nearly entirely longitudinal. Thus, the transverse momenta of all particles in the final state should add up to zero. Any momentum imbalance in the transverse plane may indicate production of invisible particles such as neutrinos or possible a new particle. This momentum imbalance in the transverse plane is referred to as a missing transverse momentum[2] ($E_{\mathrm{T}}^{\mathrm{miss}}$).

The $E_{\mathrm{T}}^{\mathrm{miss}}$ Reconstruction

The $E_{\mathrm{T}}^{\mathrm{miss}}$ is reconstructed from two contributions. The first is hard objects, which are fully reconstructed and calibrated objects such as electrons, photons, muons, hadronically decaying τ-leptons, and jets. The second is from soft terms, which are the reconstructed charged particle tracks while not matched to the hard objects. The missing transverse momentum is then written as

$$\mathbf{E}_{\mathrm{T}}^{\mathrm{miss}} = \underbrace{-\sum_{\substack{\text{selected}\\\text{electrons}}} \mathbf{p}_{\mathrm{T}}^{e} - \sum_{\substack{\text{selected}\\\text{muons}}} \mathbf{p}_{\mathrm{T}}^{\mu} - \sum_{\substack{\text{accepted}\\\text{photons}}} \mathbf{p}_{\mathrm{T}}^{\gamma} - \sum_{\substack{\text{accepted}\\\tau\text{-leptons}}} \mathbf{p}_{\mathrm{T}}^{\tau_{\mathrm{had}}} - \sum_{\substack{\text{accepted}\\\text{jets}}} \mathbf{p}_{\mathrm{T}}^{\mathrm{jet}}}_{\text{hard term}} \underbrace{- \sum_{\substack{\text{unused}\\\text{tracks}}} \mathbf{p}_{\mathrm{T}}^{\mathrm{track}}}_{\text{soft term}}, \tag{4.6}$$

[2]Missing transverse momentum is also known as missing transverse energy, $\not{E}_{\mathrm{T}}$, MET, p_{T}^{miss}, $\not{p}_{\mathrm{T}}$.

and the magnitude and direction of $E_{\mathrm{T}}^{\mathrm{miss}}$ are defined in the transverse plane as

$$E_{\mathrm{T}}^{\mathrm{miss}} = \sqrt{(E_{\mathrm{x}}^{\mathrm{miss}})^2 + (E_{\mathrm{y}}^{\mathrm{miss}})^2}, \qquad \phi_{E_{\mathrm{T}}^{\mathrm{miss}}} = \tan^{-1} \frac{E_{\mathrm{y}}^{\mathrm{miss}}}{E_{\mathrm{x}}^{\mathrm{miss}}}. \tag{4.7}$$

The $E_{\mathrm{T}}^{\mathrm{miss}}$ of Hard Objects

Each hard object is fully reconstructed and calibrated prior to the calculation of $E_{\mathrm{T}}^{\mathrm{miss}}$ of the given event. Low-level objects such as a track and a calorimeter cluster can be associated with multiple high-level objects in order to maximize the efficiency of high-level objects. Multiple inclusion of the same low-level object needs to be resolved in the calculation of $E_{\mathrm{T}}^{\mathrm{miss}}$. The overlap removal of calorimeter clusters is performed between jet and e/γ, and also between jet and muon. The most common order for the $E_{\mathrm{T}}^{\mathrm{miss}}$ reconstruction sequence for the hard object starts with muons, electrons, photons, hadronically decaying τ-leptons, and finally jets. The selection of hard objects depends on the physics analysis. Several values of $E_{\mathrm{T}}^{\mathrm{miss}}$ can be defined for a given event depending on the selection of objects. The following describes the example selections used in the electron channel analysis of this thesis:

- Electrons: Reconstructed electrons with the selection described in Section 8.3.2.
- Muons: Reconstructed muons with a loosened version of the *medium* muon selection described in Section 8.4.2. The p_{T} threshold is lowered to 20 GeV and the identification requirement is loosened to the *medium* or high-p_{T} identification working point.
- Photons: Reconstructed photons with the *Tight* identification [45], $p_{\mathrm{T}} > 25$ GeV, $|\eta| < 2.47$ (excluding the crack region $1.37 < |\eta| < 1.52$), and without signal overlap with electrons.
- Hadronically decaying τ-leptons: Reconstructed τ-leptons with the *medium* identification [46], $p_{\mathrm{T}} > 20$ GeV, $|\eta| < 2.47$ (excluding the crack region $1.37 < |\eta| < 1.52$), and without signal overlap with electrons or photons.

- Jet: Reconstructed EMTopo jets. The selection of jets is made by the $E_{\mathrm{T}}^{\mathrm{miss}}$ working point as discussed in Section 4.3.4. The jet is excluded if it overlaps with any of above objects.

The $E_{\mathrm{T}}^{\mathrm{miss}}$ Soft Term

The soft term consists of all detector signals which are not matched to hard objects. The following configurations are available for the soft term reconstruction:

- Track-based Soft Term (TST): The soft term reconstructed exclusively from ID tracks which are associated with the hard-scatter vertex. The TST performs better than the Calorimeter-based Soft Term due to better treatment of pile-up contribution to the soft term. The TST soft term is defined for both EMTopo jets and PFlow jets:
  - TST for EMTopo $E_{\mathrm{T}}^{\mathrm{miss}}$: Tracks are selected with $p_{\mathrm{T}} > 0.4$ GeV, $|\eta| < 2.5$, d_0 significance < 2, and $|\Delta z_0 \sin\theta| < 3.0$ mm. The tracks which are close to the hard objects are removed from the soft term.
  - TST for PFlow $E_{\mathrm{T}}^{\mathrm{miss}}$: Tracks are selected with $p_{\mathrm{T}} > 0.5$ GeV, $|\eta| < 2.5$, and $|\Delta z_0 \sin\theta| < 2.0$ mm. The TST for PFlow $E_{\mathrm{T}}^{\mathrm{miss}}$ uses tracks associated to charged PFlow constituents which are not associated to any hard object.
- Calorimeter-based Soft Term (CST): The soft term reconstructed from topo-clusters. The CST is a more inclusive soft term due to an inclusion of soft neutral particles.

Working Points for $E_{\mathrm{T}}^{\mathrm{miss}}$

The performance of $E_{\mathrm{T}}^{\mathrm{miss}}$ is mostly affected by the selection of jets used to reconstruct the $E_{\mathrm{T}}^{\mathrm{miss}}$. ATLAS provides the following working points for physics analyses with different jet requirements [47]:

- *Loose* $E_{\mathrm{T}}^{\mathrm{miss}}$ working point: All jets with $p_{\mathrm{T}} > 20$ GeV and also pass the JVT criteria when the jet has $|\eta| < 2.4$ and $p_{\mathrm{T}} < 60$ GeV.

- *Tight* $E_{\mathrm{T}}^{\mathrm{miss}}$ working point: Exclude forward jets with $|\eta| > 2.4$ and $p_{\mathrm{T}} < 30$ GeV. This working point is designed to reduce pile-up dependence as jets from pile-up tend to populate in the forward region. On the other hand, the scale of $E_{\mathrm{T}}^{\mathrm{miss}}$ is degraded by this selection.

- Forward-JVT (fJVT) $E_{\mathrm{T}}^{\mathrm{miss}}$ working point: In addition to the *Loose* $E_{\mathrm{T}}^{\mathrm{miss}}$ working point, reject forward jets with $|\eta| > 2.5$ and $20 < p_{\mathrm{T}} < 50$ GeV if they fail the *Loose* fJVT criteria [48].

In the analysis of this thesis, EMTopo jets with the *Tight* working point and the TST for EMTopo $E_{\mathrm{T}}^{\mathrm{miss}}$ are used for the reconstruction of $E_{\mathrm{T}}^{\mathrm{miss}}$.

Correction to $E_{\mathrm{T}}^{\mathrm{miss}}$

Corrections to the soft term of $E_{\mathrm{T}}^{\mathrm{miss}}$ are applied to MC. Other contributions from the hard terms to the $E_{\mathrm{T}}^{\mathrm{miss}}$ are calibrated before the calculation of $E_{\mathrm{T}}^{\mathrm{miss}}$.

5. Monte Carlo Simulation

Monte Carlo (MC) simulation is one of most important ingredients in particle physics experiment as it provides a crucial method to actualize our understanding of particle physics. In the real world, the particle accelerator produces proton-proton collision events. The generate particles from the proton-proton collisions are then measured by the detectors. In the virtual world, event generators play the role of particle accelerators, and the detector simulation and digitization to simulate detector responses. Figure 5.1 shows a schematic representation of the full production chain for the simulation and the data. In this chapter, the event generation is discussed in Section 5.1, and the GEANT simulation and the digitization are briefly discussed in Section 5.2. The last step, from reconstruction to analysis object data, is shared between simulation and data, and the detail of reconstruction is discussed in Chapter 4.

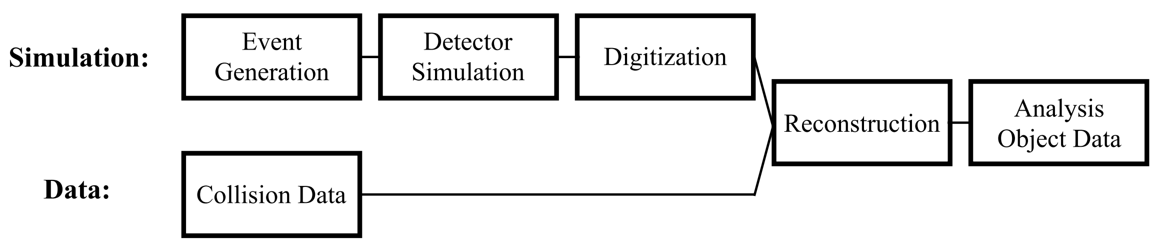

Figure 5.1. Schematic representation of the full production chain.

5.1 Monte Carlo Generator

The first step of the simulation is event generation as shown in Figure 5.1. An event generation of the proton-proton collision requires several steps, and the following summarizes this in a nutshell [49]:

- A collision between two partons, one from each proton, gives the hard process of interest such as $u\bar{d} \to W^+$, $gg \to t\bar{t}H$, $u\bar{d} \to W'$, etc. The hard process can be calculated from the Lagrangian of a theory using the Feynman rules which lead to the matrix element (ME) of the corresponding process. The decay of short-lived resonance particles, such as top, W or Z, from the hard process are included in the calculation.

- Emissions that can be associated with the two incoming colliding partons are called Initial-State Radiation (ISR).

- Emissions that can be associated with the two outgoing partons are called Final-State Radiation (FSR).

- Successive emission leads a parton cascade, which is called parton shower (PS).

- Partons which are not associated to the hard process may still collide within one single proton-proton collision. Such cases are referred to as multiple parton interactions.

- Each parton moves freely when they are close to each other based on the principle of aymptotic freedom, but color confinement forces become significant as partons recede from each other. Partons form hadrons by a process called hadronization.

The MC generators iteratively execute all or part of the steps described above. MC generators used in this analysis are described briefly below.

- Pythia [50]: A general-purpose event generator which can perform the whole event generation steps as described above. It has been extensively used for $pp/p\bar{p}$, e^+e^-, and ep physics during the last 20 years. Pythia performs a hard process calculation at leading-order (LO), and thus Pythiais often interfaced to other event generators with the higher order calculations.

- Powheg [51]: A hard process calculation at next-to-leading order (NLO) accuracy. Powheg can be interfaced with all modern shower Monte Carlo programs that support the Les Houches Interface [52] for user generated processes.

- SHERPA [53]: A general-purpose event generator for lepton-lepton, lepton-photon, photon-photon, lepton-hadron and hadron-hadron collisions. The hard process can be calculated up to NLO and next-to-next-to-leading order (NNLO) in QCD for some processes in recent SHERPA versions.

5.2 Detector Simulation

The MC generators produce events in standard HepMC format [54], which contains comprehensive information of the event such as the Lorentz vector of particles, vertices and the history of event. The detector simulation then follows as shown in Figure 5.1.

5.2.1 Full Simulation

The standard simulation of ATLAS utilizes the GEANT4 particle simulation toolkit [55] for simulating the passage of particles through material, which includes various types of interactions such as energy deposits in the sensitive detector volumes, multiple scatterings, energy losses in the magnet, and the shower evolution in the calorimeters. GEANT4 provides a detailed simulation which leads to accurate interactions, but it requires several minutes of the CPU time per event.

5.2.2 Fast Simulation

Fast simulation programs have been developed to complement the GEANT4 simulation. The most common framework is ATLFAST-II, which trys to simulate events as fast as possible while still being able to run the standard ATLAS reconstruction. ATLFAST-II consists of the Fast ATLAS Tracking Simulation (Fatras) for the ID and MS simulation and the Fast calorimeter Simulation (FastCaloSim) for the calorimeter simulation. Fatras provides a simplified reconstruction geometry as a simulation geometry model, which leads to a significant reduction of CPU time. FastCaloSim provides a parameterized simulation of the particle energy response and of the energy distribution. A factor of 100 reduction in CPU time is achieved with Fatras and FastCaloSim. ATLFAST-II shows a few percent deviations for observables such as electron identification efficiencies. It is generally left to the physics groups to evaluate if the fast simulation is acceptable in their analysis. Further details on the detector simulation in ATLAS are described in reference [56].

5.3 Digitization

The digitization is the last step before the reconstruction as shown in Figure 5.1. GEANT4 produces "Hits", which are energy deposits in sensitive detector volumes. The digitization software then converts these energy deposits into the detector responses, such as voltages or times. Hence, the peculiarities of each detector are modeled in the digitization software. As a simplified example, TRT uses energy deposits of charged particles from the Photoabsorption Ionization (PAI) model to produce ionization clusters. The charge from the ionization clusters is amplified and shaped, then the readout with a time window of 75 ns checks whether the shaped signal exceeds the threshold of 300 eV every 3.125 ns. The first active bin in the readout is converted to the position of a track in the TRT straw, which is then used as a TRT hit in the reconstruction algorithm as discussed in Section 4.1.

6. Signal Process

In this chapter, the experimental signature of the signal process is discussed in Section 6.1, and the benchmark model for the signal is discussed in Section 6.2.

6.1 Experimental Signature

The experimental signature of a new heavy gauge boson decaying into one lepton and one neutrino is, events with:

- a high-p_{T} lepton,
- large missing energy from the neutrino in the W' decay,
- a large lepton-neutrino invariant mass.

The invariant mass of the final state with one lepton and one neutrino cannot be reconstructed since only the transverse component of the neutrino momentum can be reconstructed indirectly as discussed in Section 4.3.4. Hence, the transverse mass is reconstructed from the high p_{T} lepton and missing transverse momentum. The transverse mass can be written, neglecting the mass of the leptons, as

$$m_{\mathrm{T}} = \sqrt{2 p_{\mathrm{T}} E_{\mathrm{T}}^{\mathrm{miss}} (1 - \cos \Delta\phi_{\ell, E_{\mathrm{T}}^{\mathrm{miss}}})} \tag{6.1}$$

where p_{T} is the transverse momentum of the lepton, $E_{\mathrm{T}}^{\mathrm{miss}}$ is the missing transverse energy in the event, and $\Delta\phi_{\ell, E_{\mathrm{T}}^{\mathrm{miss}}}$ is the angle between the lepton and the missing transverse momentum in the transverse plane. In the analysis of this thesis, final states with one electron or one muon and one neutrino are considered. The search in the final state with one τ-lepton and one neutrino is performed in a separate analysis.

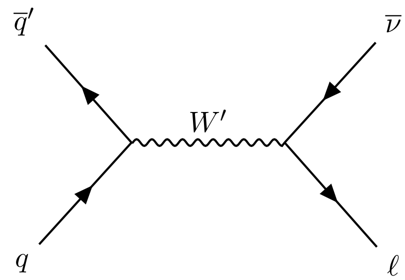

Figure 6.1. Feynman diagram of SSM W' production.

6.2 Signal Model

In principle, the search can be performed model independently as one searches for a deviation from the SM prediction in the high transverse mass region. Nevertheless, it is beneficial to have a reference model to compare with previous results or other experiments. Among the BSM models which predict a new heavy gauge boson, the SSM is chosen because it serves as a benchmark model and the result can be interpreted by other models as discussed in Section 2.3.

The SSM $W' \to e\nu$ and $W' \to \mu\nu$ processes are generated at leading-order (LO) in QCD using the Pythia 8.183 [50] with the NNPDF2.3 LO PDF sets [57]. Higher order QCD corrections are applied by a mass-dependent QCD K-factor which is calculated as the ratio of the next-to-next-to-leading order (NNLO) cross section to the LO cross section of the W boson. The higher order QCD correction derived from the W process is assumed to be valid for the W' process as the same Feynman diagrams can be considered in the higher order due to the similarity between the SSM W' and W boson. The NNLO cross section is calculated using the VRAP [58] with the CT14 NNLO PDFs [59], and the LO cross section is calculated using the same PDF set and MC generator as W' processes. The QCD K-factors are 1.34, 1.42, and 1.23 for W'^{+} and 1.37, 1.35, and 1.10 for W'^{-} at 0.5 TeV, 2 TeV, and 4 TeV, respectively. The higher order electroweak (EW) correction for the final state photon radiation (QED FSR) is modeled by Pythia. The width-to-mass ratio is 2.8%, 3.3%, and 3.4% at $m_{W'}$ = 150 GeV, 1 TeV, and 5 TeV, respectively. The branching

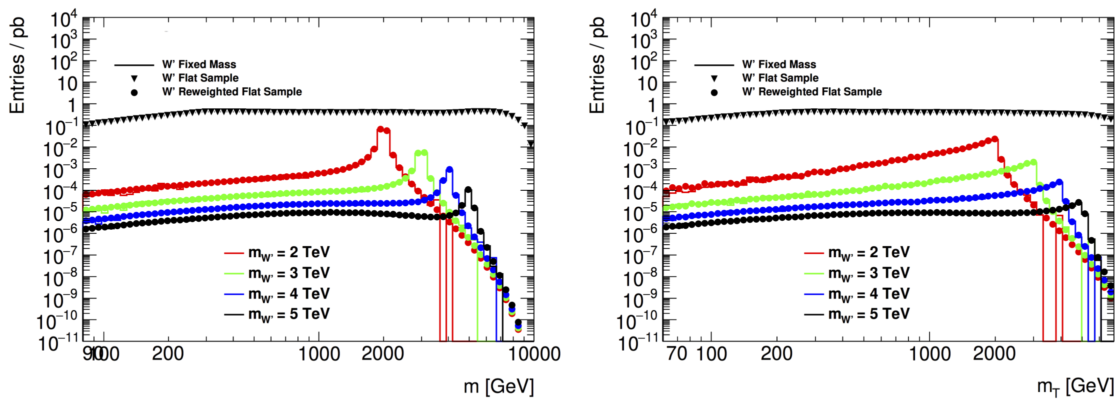

Figure 6.2. The truth invariant mass and truth transverse mass distributions of the flat W' samples, the fixed mass W' samples, and the reweighted to the same mass points from the flat W' samples.

fraction to the leptonic channels is approximately 8.2% for W' mass higher than 1 TeV, and approaches to 10.5% at low W' mass.

The search is performed for a wide range of m_{T}, from 350 GeV to 6 TeV, which requires numerous signal samples in order to test various W' pole masses. Hence, the W' samples are generated with a relatively flat distribution in the invariant mass of the $m_{\ell\nu}$ system, which can be reweighted to any W' resonant mass at the analysis level. This is achieved by the removal of the Breit-Wigner term from the Pythia event generation, which results in a flat falling distribution without resonance. In addition, the square of the matrix element is divided by a function of $m_{\ell\nu}$ in order to remove a falling distribution as a function of $m_{\ell\nu}$. Fixed mass W' samples are also produced for few mass points to validate the W' signal reweighting. Figure 6.2 shows the truth invariant mass distribution on the left-hand side and the truth transverse mass distribution on the right-hand side for the flat W' samples, some fixed mass W' samples, and the flat W' sample reweighted to the fixed mass points displayed. The transverse mass distribution from the SSM W' shows a Jacobian peak with an edge at the W' mass. The low-mass tail of the W' invariant mass distribution is due to off-shell productions, and the fraction of the low-mass tail increases with the W' mass as the parton luminosity is steeply falling with the invariant mass [60].

7. Background Processes

An accurate estimation of the background contributions from SM processes is crucial in the analysis of this thesis as a deviation from the SM processes indicates a potential new physics. The SM background processes contain one prompt lepton or misidentified lepton in the final state, and each background can be classified as reducible or irreducible background. Reducible backgrounds arise from misinterpretation in the detector leading to fake candidates, e.g. jets which mimic electrons. In principle, they can be rejected completely, but in reality this is not the completely possible. On the other hand, the irreducible backgrounds share the same final state and the same kinematics as the signal process, and thus one cannot reject them completely.

7.1 Irreducible Background

7.1.1 W Boson Production

The dominant and only irreducible background arises from the SM W boson production with final states of an electron or muon and neutrino as the signal process shares the same final state. Figure 7.1 shows some leading-order (LO) Feynman diagrams contributing to

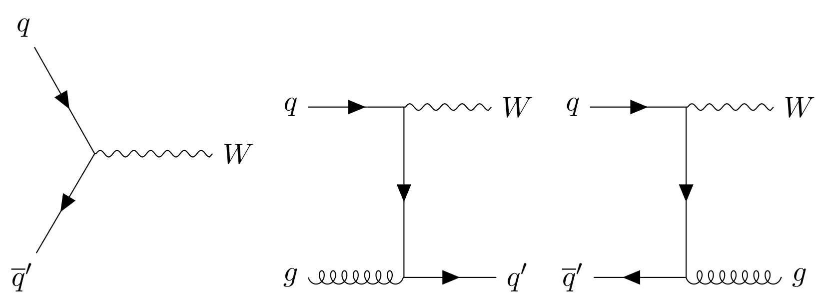

Figure 7.1. Leading order Feynman diagrams of W production.

the W production. The production cross section of W is large as shown in Figure 3.2, and the branching ratios are $10.71 \pm 0.16\%$ [61] for the decay of $W \to e\nu$ and $10.63 \pm 0.15\%$ [61] for $W \to \mu\nu$.

The backgrounds from $W \to \ell\nu$ where $\ell = e$, μ, or τ are simulated using the POWHEG-BOX for the matrix-element calculation at next-to-leading order (NLO) in perturbative quantum chromodynamics (pQCD), then interfaced to the PYTHIA 8 for parton showering using the CT10 NLO parton distribution functions (PDFs). The QED Final State Radiation (FSR) due to bremsstrahlung is separately modeled by the PHOTOS MC simulation. The cross section is calculated to next-to-next-to-leading order (NNLO) in pQCD as a function of W boson mass using VRAP with the CT14 NNLO PDFs, then a mass-dependent QCD K-factor is calculated by taking the ratio of the NNLO cross section to the NLO cross section. The resulting QCD correction factors are 1.03/1.04, 1.02/1.01 and 1.09/0.87 for W^+/W^- at 0.5 TeV, 2 TeV and 4 TeV, respectively. In addition to the QCD K-factor, the electroweak (EW) K-factor is derived at NLO as a function of W boson mass using the MCSANC which includes Initial State Radiation (ISR), ISR/FSR interference, and Sudakov logarithm single-loop correction. The resulting EW correction factors are 0.95/0.95, 0.86/0.86 and 0.81/0.80 for W^+/W^- production at 0.5 TeV, 2 TeV and 4 TeV, respectively. The final correction factor to the cross section is calculated in the so-called additive approach defined by $1+\delta_{EW} + \delta_{QCD}$ where $\delta_{EW} = K_{EW} - 1$ and $\delta_{QCD} = K_{QCD} - 1$. The $W \to \ell\nu$ samples are produced for all three lepton flavors separately from W^+ and W^-. The statistical precision at high transverse mass is limited as the cross section for off-shell W production falls steeply as a function of W boson mass. Thus, W samples are produced in the bins of truth invariant mass of the lepton-neutrino pair $m_{\ell\nu}^{\text{truth}}$ starting from 120 GeV to populate sufficient statistics in the high invariant mass region. Inclusive W samples are also produced to cover $m_{\ell\nu}^{\text{truth}} < 120$ GeV. Figure 7.2 shows the $W^+ \to e\nu$ backgrounds binned in truth invariant mass distribution on the left and the truth transverse mass distribution on the right. Table A.2, Table A.3, Table A.4, Table A.5, Table A.6, and Table A.7 in Appendix A provide a summary of the samples used to model the $W \to \ell\nu$ background component.

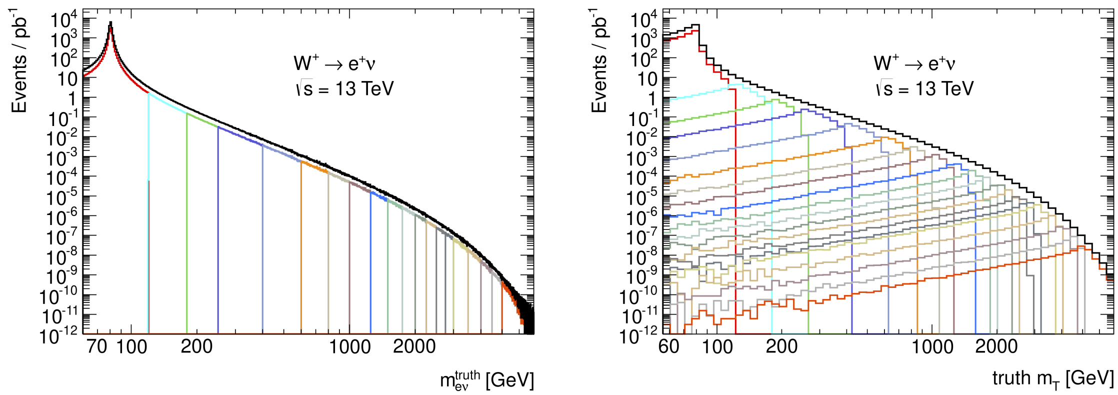

Figure 7.2. The truth invariant mass and truth transverse mass distributions of the invariant mass-binned W samples.

7.2 Reducible Backgrounds

7.2.1 Top Quark Pair and Single Top Production

The largest reducible background arises from top quark pair, $t\bar{t}$, production as the top quark decays almost 100% into a W boson and a b-quark. The final state can be one lepton from the first W boson, missing transverse momentum from a neutrino of the first W boson, and few jets from two b-quarks and the other W boson. Figure 7.3 shows LO Feynman diagrams contributing to the $t\bar{t}$ production.

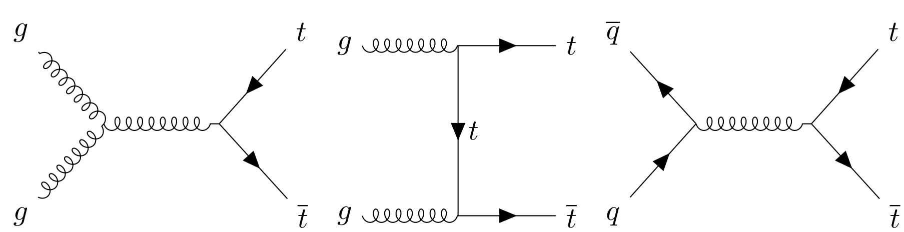

Figure 7.3. Leading order Feynman diagrams of $t\bar{t}$ production.

The background from $t\bar{t}$ production is generated at NLO in pQCD using Powheg-Box, then interfaced to the Pythia 8 for parton showering using the NNPDF [57] PDF set and the A14 tune. The $t\bar{t}$ cross section is normalized to $\sigma_{t\bar{t}} = 832$ pb, which is calculated using the program `Top++` 2.0 at NNLO in pQCD including resummation of soft-gluon terms at next-to-next-to-leading logarithmic (NNLL) order. The $t\bar{t}$ sample is produced for the final state with at least one lepton, and Table A.1 provides a summary of the samples used to model the $t\bar{t} \to \ell X$ background component.

Single top production is an additional background, which includes Wt, s- and t-channel production as shown in Figure 7.4. Wt production has a similar final state to $t\bar{t}$ production as two W bosons are involved in the process. Both s- and t-channel production involve a W boson from top-quark with additional jets, which also share the final state with the signal process. The s-channel single top production cross section is about 10 times smaller than the t-channel single top production cross section [62] [63].

The background from t-channel production is simulated using the same event generators and PDF sets as for the $t\bar{t}$ production, while Wt process is generated at NLO in pQCD using Powheg-Box, then interfaced to the Pythia 6 using the CT10 PDF set. The Wt and t-channel single top samples are produced for t and $\bar{t}$ separately. Table A.1 provides a summary of the samples used to model the $Wt \to X$ and $t \to \ell X$ background component.

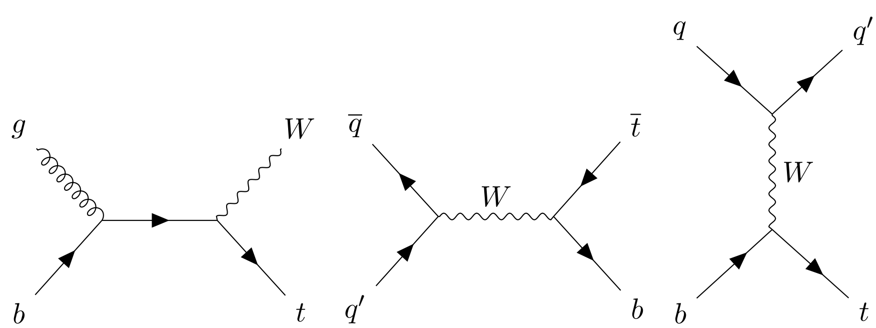

Figure 7.4. Leading order Feynman diagrams of single top productions for Wt (left), s-channel (middle), and t-channel (right) processes.

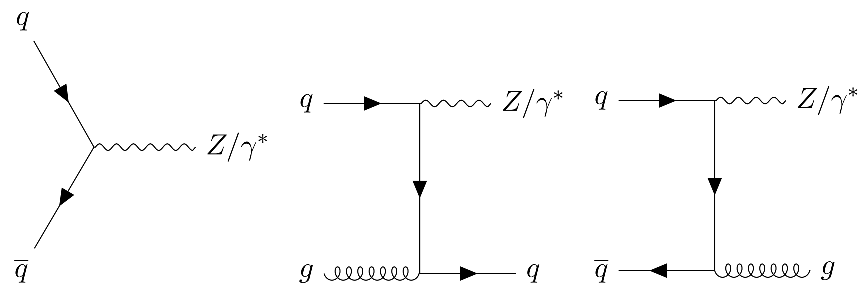

Figure 7.5. Leading order Feynman diagrams of Z/γ^* production

7.2.2 Z/γ^* Production

Neutral current Drell-Yan production is another of the reducible backgrounds. Although dielectron and dimuon events can be suppressed by rejecting events with an additional lepton in the event selection, one lepton can fall outside of the detector acceptance, which leads to large missing transverse momentum in the event. The background from $Z/\gamma^* \to \tau\tau$ arises in the final state of one lepton from the leptonic decay of one tau-lepton and the hadronic decay of the other tau-lepton. Figure 7.5 shows some LO Feynman diagrams contributing to the Z/γ^* production.

The backgrounds from $Z/\gamma^* \to \ell\ell$ are simulated using the same event generators, PDF sets, and corrections as for W production. The $Z/\gamma^* \to \ell\ell$ samples are produced for all three lepton flavors in the bins of truth invariant mass of the dilepton pair $m_{\ell\ell}^{\text{truth}}$ as for W production. Table A.8, Table A.9, and Table A.10 provides a summary of the samples used to model the $Z \to \ell\ell$ background component.

7.2.3 Diboson Production

A minor background arises from diboson productions, i.e., WW, WZ, and ZZ. The following processes which contains at least one lepton in the final state are simulated: $WW/WZ \to \ell\nu qq$, $WZ \to \ell\nu\nu\nu$, $WZ/ZZ \to qq\ell\ell$, $WW/ZZ \to \ell\ell\nu\nu$, $WZ \to \ell\ell\ell\nu$, and $ZZ \to \ell\ell\ell\ell$. The final states with one lepton share the same final state as the signal process. Besides, the final states with more than one lepton can fake the signal process for the same reason as the dilepton production. Even though the various diboson processes contribute to the background, background from diboson processes is a minor contribution as the production cross section of diboson processes is small as shown in Figure 3.2.

The backgrounds from diboson processes are simulated with the SHERPA 2.2 using the NNPDF3.0 NNLO PDF set. The diboson samples are produced for all processes mentioned above, and Table A.1 provides a summary of the samples.

7.2.4 Multijet Background

The predominant process at hadron colliders is QCD multijet events due to abundant light quarks and gluons in colliding hadrons. Many different diagrams can contribute to the background, and some of LO Feynman diagrams for dijet production are shown in Figure 7.6. Final states with light-flavor jets can fake the final state of the signal as one jet can be misidentified as a lepton. It is a sizable contribution for the electron channel but very unlikely for the signal final state of muon channel as the probability of particles from a light flavor jet traversing all of the calorimeter material without being absorbed and reaching the muon chambers is very small. However, the background from multijet still contributes to the muon channel as a heavy flavor jet can have an energetic muon in the final state or a light hadron (like $\pi^{\pm}, K^{\pm}$), which decays into a muon.

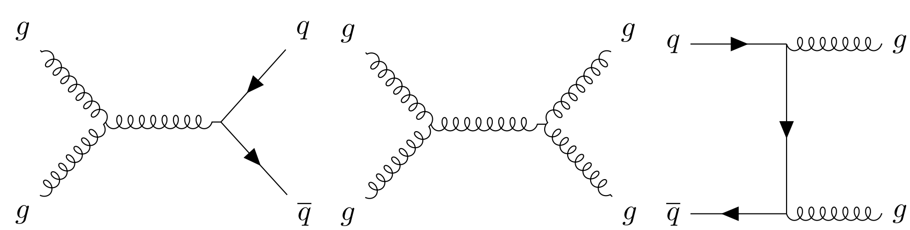

Figure 7.6. Some leading order Feynman diagrams of QCD dijet production

The background from QCD multijet is estimated from data using a data-driven technique as uncertainties on the predicted cross-section, QCD modeling, and modeling hadronic activity not associated with the hard-scattering are considerable.

8. Event Selection

In this chapter, the collision data used in the analysis is discussed in Section 8.1. The event selection for the event topology of a high transverse momentum lepton and high missing transverse momentum is discussed from Section 8.2 to Section 8.4. The event selection efficiency for the W' signal is discussed in Section 8.5.

8.1 Collision Data

This analysis uses the pp collision data collected with the ATLAS detector from 2015 to 2017 at a center-of-mass energy of $\sqrt{s} = 13$ TeV with a bunch spacing of 25 ns. The total integrated luminosity used in the analysis is 79.8 fb^{-1}, which is the sum of 3.2 fb^{-1} in 2015, 33.0 fb^{-1} in 2016, and 43.6 fb^{-1} in 2017. The cumulative integrated luminosity as a function of time is shown on the left-hand side of Figure 8.1. The ATLAS Recorded

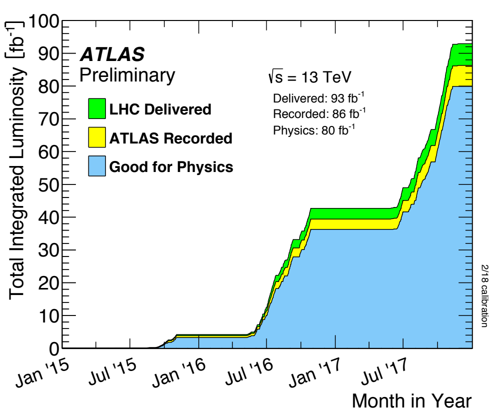

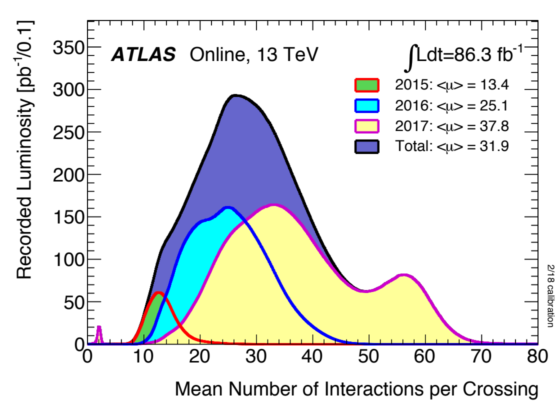

Figure 8.1. Left: Cumulative integrated luminosity delivered to ATLAS (green), recorded by ATLAS (yellow), and certified to be good quality data (blue) versus time from 2015 to 2017. Right: Mean number of interactions per bunch crossing distributions from 2015 to 2017.

luminosity reflects the losses due to the DAQ inefficiency and the ramp-up time of the tracking detectors as they ramp after the stable beam flag for protection purpose. The "Good for Physics" categorization requires that all detector components used to reconstruct physics objects for the analysis were producing good data. The mean pile-up is shown on the right-hand side of Figure 8.1. The mean pile-up from 2015 to 2017 is about 32 collisions per bunch crossing, and the higher pile-up fundamentally corresponds to the steeper slope in the cumulative integrated luminosity distribution.

8.2 Preselection

The analysis is performed on a subset of the full dataset preselected to be of interest to the analysis to significantly reduce the computing time used. The events are preselected with the requirement of at least one electron candiate with p_{T} above 60 GeV in the electron channel and at least one muon candidate identified as a combined muon with p_{T} above 50 GeV in the muon channel.

8.2.1 Data Quality

The fundamental time unit of ATLAS detector configuration and status is the luminosity block (LB), which is roughly one minute of data with constant luminosity [64]. The physics analysis uses all events in the list of LBs which fulfill quality requirements of the reconstructed physics objects. The list of good quality LBs is called Good Run List (GRL), and three GRLs[1] for 2015 to 2017 data are used in this analysis. The GRL is applied only to the collision data.

[1] data15_13TeV.periodAllYear_DetStatus-v89-pro21-02_Unknown_PHYS_StandardGRL_All_Good_25ns.xml, data16_13TeV.periodAllYear_DetStatus-v89-pro21-01_DQDefects-00-02-04_PHYS_StandardGRL_All_Good_25ns.xml, data17_13TeV.periodAllYear_DetStatus-v97-pro21-13_Unknown_PHYS_StandardGRL_All_Good_25ns _Triggerno17e33prim.xml

8.2.2 Event Cleaning

Events are discarded if any of the following conditions are satisfied. The SCT implemented effective recovery of SEU-induced bit flips to minimize noisy chips, and tracking information is missing for events collected during the recovery procedure. The LAr suffers bursts of coherent noise over a large region of the detector, and events within a time window of a burst are rejected since energy measurements are corrupted. The Tile contains corrupted data due to the non-optimal algorithm which rejects problematic events. Incomplete events due to a recovery process of a specific detector system during a run and events without a primary vertex which requires to have at least two tracks associated to it are also discarded. The efficiency of the event cleaning is above 99% for both electron and muon channels as shown in Table 8.2 and Table 8.3, respectively.

8.3 Electron Channel

8.3.1 Trigger Configuration

Only events that pass the electron triggers shown in Table 8.1 are accepted for analysis. The trigger configuration for the 2015 data-taking period is the logical OR of the three following triggers. The first trigger is seeded by an Level-1 trigger that uses η-dependent energy thresholds in the electromagnetic calorimeter and cuts on the amount of energy deposited in the hadronic calorimeter directly behind the core electromagnetic cluster [65] is less than a certain value. The trigger then requires one electron with $p_{\mathrm{T}} > 24$ GeV

Data-taking period	Trigger
2015 data	e24_lhmedium_L1EM20VH OR e60_lhmedium OR e120_lhloose
2016 data	e60_lhmedium_nod0 OR e140_lhloose_nod0
2017 data	e60_lhmedium_nod0 OR e140_lhloose_nod0

Table 8.1. Trigger configuration of electron channel for each data-taking period

and the *medium* likelihood identification operating point. The second trigger requires one electron with $p_{\mathrm{T}} > 60$ GeV and the *medium* likelihood identification operating point. The third trigger requires one electron with $p_{\mathrm{T}} > 120$ GeV and the *loose* likelihood identification operating point. The trigger configurations for the 2016 and 2017 data-taking periods are the same and the logical OR of two triggers. The first trigger requires one electron with $p_{\mathrm{T}} > 60$ GeV and the *medium* likelihood identification operating point where likelihood is calculated without d_0 information. The second trigger requires one electron with $p_{\mathrm{T}} > 140$ GeV and the *loose* likelihood identification operating point where likelihood is calculated without d_0 information. The efficiency of the trigger with respect to the preselected events is about 35% as shown in Table 8.2.

8.3.2 Electron Object Selection

An event with at least one electron candidate which satisfies all of the following selections is accepted.

Pseudorapidity

The event is required to have an electron candidate within $|\eta| < 2.47$, which is motivated by the coverage of the Inner Detector and the calorimeters. An electron candidate in the transition region between the barrel and endcap of electromagnetic calorimeters, $1.37 < |\eta| < 1.52$, is discarded due to the worse energy resolution caused by a large amount of material in front of the first active calorimeter layer in this region.

Electron Quality

The electron candidate is rejected if it is associated with a bad cluster in the electromagnetic calorimeter, which is affected by the presence of a dead Front End Board or a dead High Voltage or a masked cell in the core.

Transverse Momentum

The transverse momentum threshold on the electron candidate is set to $p_{\mathrm{T}} > 65$ GeV, which is 5 GeV higher than the lower p_{T} trigger threshold in 2016 and 2017 in order to reflect a possible difference on the p_{T} measurements at the trigger-level and reconstruction-level.

Impact Parameters

In order to ensure the electron candidate is coming from the collision vertex, the electron candidate is required to have a transverse impact parameter significance, d_0 significance $<$ 5. The top left plot in Figure 8.2 shows the distribution of d_0 significance for electrons from the $W' \rightarrow e\nu$ decay in the W' flat sample, and the top right plot shows for the same distribution for backgrounds and data at final selection. The d_0 significance distribution for electrons from the W' decay is very narrow and steeply falling. On the other hand, the distribution for backgrounds and data is relatively wide, and the multijet background dominates for d_0 significance larger than 3. The cut efficiency of d_0 significance is above 99.5% and close to 100% for high p_{T} electrons as shown on the left-hand side of Figure 8.3. The cut on the longitudinal impact parameter is recommended by the ATLAS *Tracking Combined Performance* group to identify tracks from the primary vertex. However, the cut on the longitudinal impact parameter is not applied as the cut of $|\Delta z_0 \sin\theta| < 0.5$ mm leads a noticeable efficiency reduction of about 4%. It is due to the difficulty of finding the primary vertex under high pile-up condition as shown on the right-hand side of Figure 8.3.

Electron Identification

The electron candidate is required to satisfy the *tight* likelihood identification operating point, which is discussed in Section 4.3.1, in order to achieve high purity and low background efficiency.

Electron Isolation

Electron isolation is required in order to discriminate prompt electrons from non-isolated electron candidates such as electrons from heavy flavor decays and misidentified light quark jets. The electron candidate is required to fulfill the *Loose* isolation operating point which varies selection requirements on the calorimetric isolation, $E_{\mathrm{T}}^{\mathrm{cone0.2}}/E_{\mathrm{T}}$, and the track isolation, $p_{\mathrm{T}}^{\mathrm{varcone0.2}}/E_{\mathrm{T}}$, to obtain an isolation efficiency of about 98%.

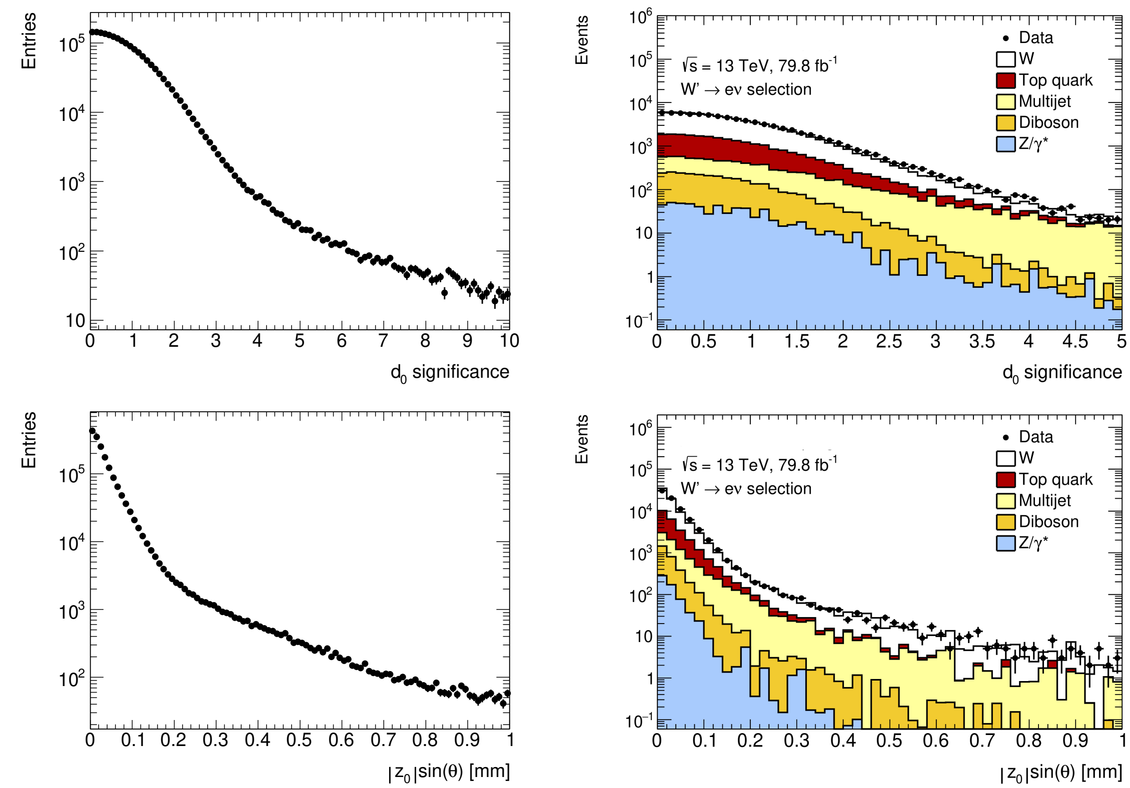

Figure 8.2. The distributions of d_0 significance on the top and $|\Delta z_0 \sin\theta|$ on the bottom. The left plots show the distributions for electrons with a truth matching requirement ($\Delta R < 0.2$) in the W' flat sample. The right plots show the distributions for backgrounds and data at final selection.

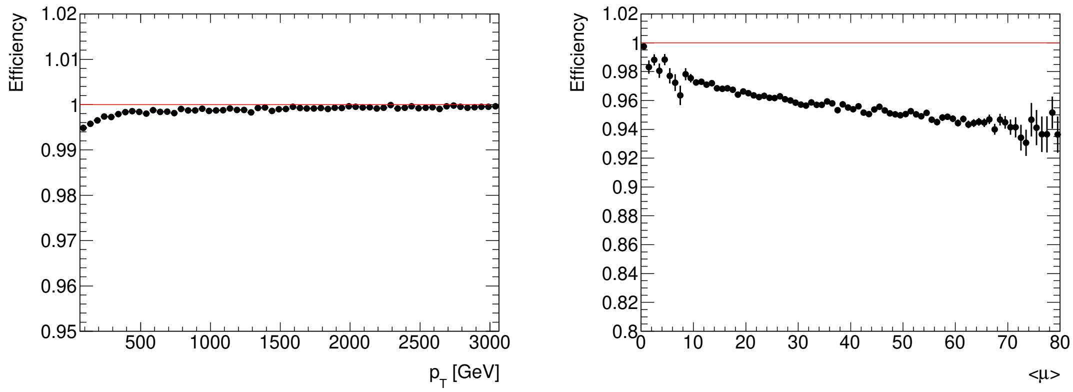

Figure 8.3. The cut efficiency of d_0 significance as a function of p_{T} (left) and the cut efficiency of $|\Delta z_0 \sin\theta|$ as a function of $\langle\mu\rangle$ (right). Both efficiencies are measured in the W' flat sample.

8.3.3 Event Topology Selection

The event is rejected if the event fails any of the following selections.

Additional Lepton Veto

The event is required to have exactly one electron which fulfills the selection described above. The event is also rejected if the event contains an additional lepton which satisfies the loosened version of electron selection or muon selection. The p_{T} threshold is lowered to 20 GeV, and the *Tight* identification is replaced by the *Medium* identification operating point for the loosened electron selection with respect to the final selection described in Section 8.3.2. The p_{T} threshold is also lowered to 20 GeV, and the high-p_{T} working point is replaced by the inclusive OR of the *medium* and high-p_{T} working point for the loosened muon selection with respect to the final selection described in Section 8.4.2. The additional lepton veto requirement effectively reduces backgrounds from Z/γ^{*}, top, and diboson events as discussed in Section 7.2.

Fake Jet Veto

The event is rejected if the event contains any jets identified as "fakes", which originate from the non-collision backgrounds such as beam-gas scattering or cosmic muon induced showers. The presence of fake jets could contaminate the measurement of missing transverse energy. Hence not only the fake jet but the whole event is rejected.

Transverse Missing Momentum

The event is required to have $E_{\mathrm{T}}^{\mathrm{miss}} > 65$ GeV. The background processes without neutrinos in the final state are suppressed with this requirement.

Transverse Mass

The event is finally required to have $m_{\mathrm{T}} > 300$ GeV, from the selected electron and the $E_{\mathrm{T}}^{\mathrm{miss}}$. The threshold was chosen to focus on the search in the high-mass region.

8.3.4 Cut-flow in the Electron Channel

Table 8.2 shows the cut-flow at the signal selection in the electron channel.

	Cut	Electron channel
Preselection	Good Run List	265,967,040 (-)
	Event cleaning	265,737,152 (99.9%)
	Trigger	92,827,552 (34.9%)
Electron object selection	Pseudorapidity	92,487,968 (99.6%)
	Electron quality	92,474,880 (99.9%)
	$p_{\mathrm{T}} > 65$ GeV	70,233,120 (76.0%)
	d_0 significance	67,852,608 (96.6%)
	Electron identification	44,358,488 (65.4%)
	Isolation	41,487,696 (93.53%)
Event topology selection	Additional electron veto	37,500,728 (90.4%)
	Additional muon veto	37,193,600 (99.2%)
	Fake jet veto	37,152,160 (99.9%)
	$E_{\mathrm{T}}^{\mathrm{miss}} > 65$ GeV	5,018,550 (13.5%)
	$m_{\mathrm{T}} > 300$ GeV	80,081 (1.6%)

Table 8.2. Number of events after each selection in the electron channel. The numbers in the parentheses are the efficiencies with respect to the previous line.

8.4 Muon Channel

8.4.1 Trigger Configuration

Events are accepted from those who pass the single muon trigger which requires one muon with $p_{\mathrm{T}} > 50$ GeV. The efficiency of the trigger with respect to the preselected events is about 73% as shown in Table 8.3.

8.4.2 Muon Object Selection

An event with at least one muon candidate which satisfies all of the following selections is accepted.

Combined Muon

The muon candidate is required to be a combined muon, which utilizes independently reconstructed tracks in the ID and MS to perform a global fit of the hits from both the ID and MS subdetectors. The pseudorapidity coverage is limited to the coverage of ID, $|\eta| < 2.5$, accordingly.

Transverse Momentum

The transverse momentum threshold on the muon candidate is set to $p_{\mathrm{T}} > 55$ GeV, which is 5 GeV higher than the trigger threshold. The efficiency of p_{T} cut reflects the preselection which requires a combined muon with $p_{\mathrm{T}} > 50$ GeV.

Impact Parameters

The muon candidate is required to have a transverse impact parameter significance, d_0 significance < 3. The top left plot in Figure 8.4 shows the distribution of d_0 significance for muons from the $W' \rightarrow \mu\nu$ decay in the W' flat sample, and the top right plot shows the

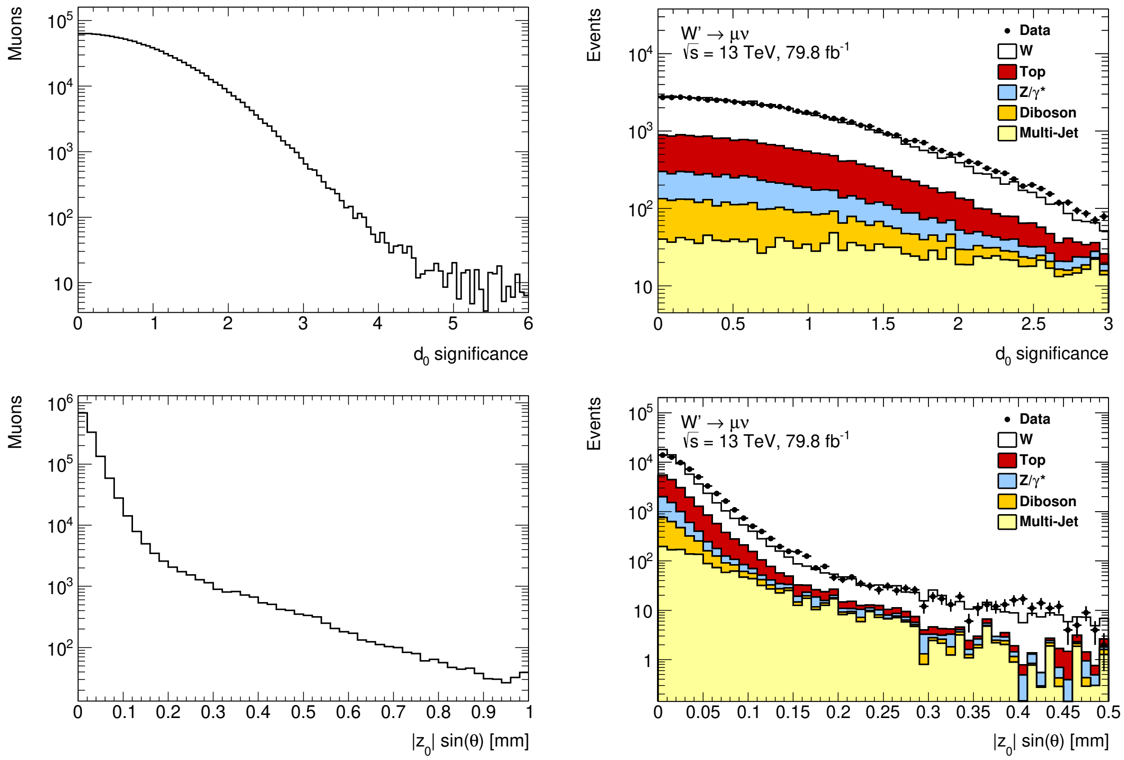

Figure 8.4. The distributions of d_0 significance on the top and $|\Delta z_0 \, \sin\theta|$ on the bottom. The left plots show the distributions for muons with a truth matching requirement ($\Delta R < 0.2$) in the W' flat sample. The right plots show the distributions for backgrounds and data at final selection.

same quantity for backgrounds and data at the final selection. A muon candidate is also required to have longitudinal impact parameter significance, $|\Delta z_0 \, \sin\theta| < 0.5$ mm. The bottom plots in Figure 8.4 show the $|\Delta z_0 \, \sin\theta|$ distributions in the W' flat sample on the left-hand side and the data at the final selection on the right-hand side. Unlike the electron channel, the efficiency of $|\Delta z_0 \, \sin\theta|$ cut stays over 98%, hence the cut is kept in the muon channel.

Muon Identification

The muon candidate is required to satisfy the *High-*p_{T} muons identification selection, which is discussed in Section 4.3.2.

Muon Quality

The muon candidate is rejected if the relative q/p error of the combined track fit is too large. Muon candidates within $1.01 < |\eta| < 1.1$ are rejected as the transition region between the barrel and endcap of the MS experiences some reconstruction issues.

Muon Isolation

The muon candidate is required to satisfy the *LooseTrackOnly* isolation working point which varies selection requirement on the track isolation to obtain an isolation efficiency of about 99%.

8.4.3 Event Topology Selection

The event is rejected if the event fails any of the following topological selections.

Additional Lepton Veto

The event is required to have exactly one muon which fulfills the selection described above. The event is also rejected if the event contains an additional lepton which satisfies the loosened version of muon selection or electron selection. The p_{T} threshold is also lowered to 20 GeV, and the high-p_{T} working point is replaced by the inclusive OR of the *medium* and high-p_{T} working point for the loosened muon selection with respect to the final selection described in Section 8.4.2. The p_{T} threshold is lowered to 20 GeV, and the *Tight* identification is replaced by the *Medium* identification operating point for the loosened electron selection with respect to the final selection described in Section 8.3.2.

The additional lepton veto requirement effectively reduces backgrounds from Z/γ^*, top, and diboson events as discussed in Section 7.2.

Fake Jet Veto

An event which contains any jets identified as "fake" is rejected, as in the electron channel, in order to prevent a wrong $E_{\mathrm{T}}^{\mathrm{miss}}$ estimation.

Transverse Missing Momentum

The event is required to have $E_{\mathrm{T}}^{\mathrm{miss}} > 55$ GeV. Background processes without neutrinos in the final state are suppressed with this requirement.

Transverse Mass

The event is finally required to have $m_{\mathrm{T}} > 300$ GeV, from the selected muon and the $E_{\mathrm{T}}^{\mathrm{miss}}$. The threshold was chosen to focus on the search in the high-mass region.

8.4.4 Cut-flow in the Muon Channel

Table 8.3 shows the cut-flow at the signal selection in the muon channel.

	Cut	Muon channel
Preselection	Good Run List	239,608,981 (-)
	Event cleaning	239,420,954 (99.9%)
	Trigger	174,681,345 (73.0%)
Muon object selection	Combined muon	174,681,341 (100.0%)
	$p_{\mathrm{T}} > 55$ GeV	117,564,305 (67.3%)
	d_0 significance	86,341,056 (73.4%)
	$\lvert \Delta z_0 \sin\theta \rvert$	85,905,027 (99.5%)
	Muon identification	71,259,605 (83.0%)
	Muon quality	71,259,365 (100.0%)
	Isolation	52,211,490 (73.3%)
Event topology selection	Additional muon veto	44,093,100 (84.5%)
	Additional electron veto	43,837,937 (99.4%)
	Fake jet veto	43,787,500 (99.9%)
	$E_{\mathrm{T}}^{\mathrm{miss}} > 55$ GeV	9,511,312 (21.7%)
	$m_{\mathrm{T}} > 300$ GeV	60,067 (0.6%)

Table 8.3. Number of events after each selection in the muon channel. The numbers in the parentheses are the efficiencies with respect to the previous line.

8.5 Event Selection Efficiency for the W' Signal

The event selections are applied to the $W' \to e\nu$ channel and the $W' \to \mu\nu$ channel. The cut efficiency flow for the W' masses of 3 TeV, 4 TeV, and 5 TeV is shown in Table 8.4 for the $W' \to e\nu$ channel and Table 8.5 for the $W' \to \mu\nu$ channel. The selection efficiencies

Cut	SSM W' (3 TeV)	SSM W' (4 TeV)	SSM W' (5 TeV)
Total events	(909)	(489)	(32.7)
Event cleaning	100.0%	100.0%	100.0%
Trigger	91.2%	90.8%	82.9%
Pseudorapidity	99.5%	99.3%	99.3%
Electron quality	99.9%	99.9%	99.9%
$p_{\mathrm{T}} > 65$ GeV	96.5%	96.4%	95.6%
d_0 significance	99.9%	99.9%	99.8%
Electron identification	92.7%	92.7%	92.7%
Isolation	99.4%	99.3%	99.3%
Additional electron veto	100.0%	99.9%	99.9%
Additional muon veto	100.0%	100.0%	100.0%
Fake jet veto	100.0%	100.0%	100.0%
$E_{\mathrm{T}}^{\mathrm{miss}} > 65$ GeV	99.7%	99.7%	98.8%
$m_{\mathrm{T}} > 300$ GeV	97.4% (710)	97.0% (378)	90.4% (21.0)
Total efficiency	78.1%	77.2%	64.4%

Table 8.4. Cut efficiency flow of W' signals in the electron channel. The efficiencies are with respect to the previous line. The numbers in parentheses are the number of events normalized to the integrated luminosity of the data, but without corrections such as K-factors, efficiency scale factors, and pileup reweighting.

Cut	SSM W' (3 TeV)	SSM W' (4 TeV)	SSM W' (5 TeV)
Total events	(922)	(144)	(32.5)
Event cleaning	100.0%	100.0%	100.0%
Trigger	72.2%	70.4%	67.8%
Combined muon	100.0%	100.0%	100.0%
$p_{\mathrm{T}}> 55$ GeV	99.5%	99.1%	98.4%
d_0 significance	99.7%	99.7%	99.7%
$\lvert z_0\rvert \sin\theta$	98.3%	98.3%	98.2%
Muon identification	82.7%	82.4%	82.6%
Muon quality	99.2%	98.8%	98.4%
Isolation	99.5%	99.5%	99.4%
Additional muon veto	100.0%	100.0%	100.0%
Additional electron veto	99.9%	99.9%	99.9%
Fake jet veto	100.0%	99.9%	99.9%
$E_{\mathrm{T}}^{\mathrm{miss}} > 55$ GeV	99.7%	99.4%	98.8%
$m_{\mathrm{T}} > 300$ GeV	96.6% (498)	93.3% (72.1)	87.5% (14.5)
Total efficiency	54.1%	50.0%	44.6%

Table 8.5. Cut efficiency flow of W' signals in the muon channel. The efficiencies are with respect to the previous line. The numbers in parentheses are the number of events normalized to the integrated luminosity of the data, but without corrections such as K-factors, efficiency scale factors, and pileup reweighting.

are generally well above 95%, but the trigger and identification efficiencies are relatively low in both channels. Hence, the total efficiency is mainly determined by the trigger and identification efficiencies. The total efficiency is about 20% higher in the electron channel than in the muon channel due to about 20% lower trigger efficiency and about 10% lower identification efficiency in the muon channel. In addition, a decrease in the total efficiency is observed with W' mass, which is driven by the lower trigger efficiency in higher W' mass.

Figure 8.5 shows the total acceptance times efficiency as a function of W' pole mass. The total acceptance times efficiency is defined as the number of reconstructed candidates divided by all generated candidates. The total acceptance times efficiency increases radically from the low pole mass to the intermediate pole mass around 1 TeV as the high kinematic cut of p_{T}, $E_{\mathrm{T}}^{\mathrm{miss}}$, and m_{T} rejects a significant fraction of events for the low W' pole masses. The total acceptance times efficiency rises with the W' pole masses and it starts to decrease for the high W' pole masses above 2 TeV. This is due to the dominant off-shell productions for the high W' pole masses as shown in Figure 6.2. Although the Jacobian peaks move to higher masses with increasing W' pole masses, the fraction of off-shell production also rises with increasing W' pole mass.

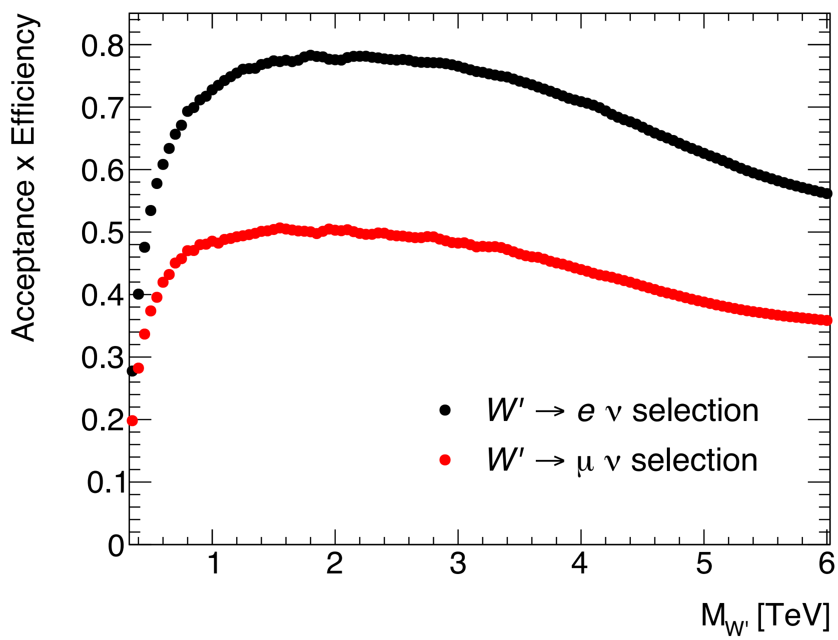

Figure 8.5. Total W' signal acceptance $\times$ efficiency as a function of SSM W' pole mass in the electron channel and the muon channel.

9. Background Estimation

In this chapter, the methods used to estimate the contribution of each background process to the observed events are presented. The multijet background estimation using a data-driven approach is discussed in Section 9.1. The other backgrounds modeled by MC simulations are discussed in Section 9.2. The background extrapolation to very high m_{T} for the statistically limited backgrounds is discussed in Section 9.3.

9.1 Multijet Background Estimation

The multijet background arises from misidentified leptons as discussed in Section 7.2.4. A data-driven background estimation technique, the matrix method, is used to estimate the multijet background in the electron and muon channel.

9.1.1 Principle of the Matrix Method

The matrix method is a powerful technique to estimate a fake contribution in the signal object selection. It utilizes a loosened object selection in addition to the signal or tight object selection, and measures the efficiencies of loose objects to pass the tight selection. This allows an estimation of the fake contribution in the tight selection. The fake contribution is estimated on an event-by-event basis by counting number of loose and tight leptons, while the efficiencies should be measured in advance.

The basic quantities measured or calculated for each event are:

- N_T = number of lepton candidates in the tight selection (measured in data)
- N_L = number of lepton candidates in the loose selection (measured in data)
- N_R = number of real leptons in the *Loose* sample(to be determined)
- N_F = number of fake leptons in the *Loose* sample (to be determined)

The efficiency is defined separately for real leptons (real efficiency ϵ_R) and fake leptons (fake efficiency ϵ_F):

$$\epsilon_F = \frac{N^{\text{fake}}_{\text{tight}}}{N^{\text{fake}}_{\text{loose}}}, \qquad \epsilon_R = \frac{N^{\text{real}}_{\text{tight}}}{N^{\text{real}}_{\text{loose}}}. \tag{9.1}$$

The real efficiency is measured from MC as truth information of real leptons is available. On the other hand, the fake efficiency is usually measured from data in a fake enriched control region. The connection between each quantity is represented in Equation 9.2.

$$\begin{pmatrix} N_T \\ N_L \end{pmatrix} = \begin{pmatrix} \epsilon_R & \epsilon_F \\ 1 & 1 \end{pmatrix} \begin{pmatrix} N_R \\ N_F \end{pmatrix} \tag{9.2}$$

The equation can be expressed for the truth quantities by inverting the matrix:

$$\begin{pmatrix} N_R \\ N_F \end{pmatrix} = \frac{1}{\epsilon_R - \epsilon_F} \begin{pmatrix} 1 & -\epsilon_F \\ -1 & \epsilon_R \end{pmatrix} \begin{pmatrix} N_T \\ N_L \end{pmatrix} \tag{9.3}$$

Finally, the fake contribution to the signal selection can be expressed by multiplying the second line of Equation 9.3 by the fake efficiency:

$$\epsilon_F N_F = \frac{\epsilon_F \epsilon_R}{\epsilon_R - \epsilon_F} N_L - \frac{\epsilon_F}{\epsilon_R - \epsilon_F} N_T \tag{9.4}$$

9.1.2 Multijet Background Estimation in the Electron Channel

The multijet background in the electron channel arises mainly from light-flavor jets as discussed in Section 7.2.4. The matrix method requires both a loose and a tight selection. The tight selection is the signal selection described in Section 8.3.2. The loose selection of the electron object which allows more QCD jets can be achieved by removing isolation requirement and by a looser identification requirement. The electron identification requirement in the trigger restricts the identification operating point for the loose selection. The trigger requires the *medium* identification operating point for $p_{\text{T}} < 145$ GeV and the *loose* identification operating point for $p_{\text{T}} > 145$ GeV as discussed in Section 8.3.1. Thus, the loose selection removes the isolation requirement from the tight selection and replaces the *tight* identification with the *medium* identification excluding candidates that fail the *tight* identification for $p_{\mathrm{T}} < 145$ GeV or with the *loose* identification excluding candidates that fail the *tight* identification for $p_{\mathrm{T}} > 145$ GeV.

Real Efficiency Estimation

The real efficiency is the probability for real electrons to pass the tight selection. Hence, the real efficiency is estimated using electrons from the W MC sample with an additional truth-matching requirement which is $\Delta R < 0.2$ between reconstructed and truth electron. The real efficiency is measured as a function of p_{T} and η as shown in Figure 9.1. The real efficiency lies between 95% to 99% for both p_{T} and η except in the transition region between the barrel and end-cap calorimeters. The two dimensional real efficiency in η and p_{T}, shown in Figure 9.2, is used for the fake contribution calculation in Equation 9.4, and the binning in η is motivated by the detector geometry: barrel region ($|\eta| < 1.37$), endcap region with TRT ($1.52 < |\eta| < 2.01$), and endcap region without TRT ($2.01 < |\eta| < 2.47$). The binning in p_{T} is motivated by the fake efficiency which will be discussed in the following section.

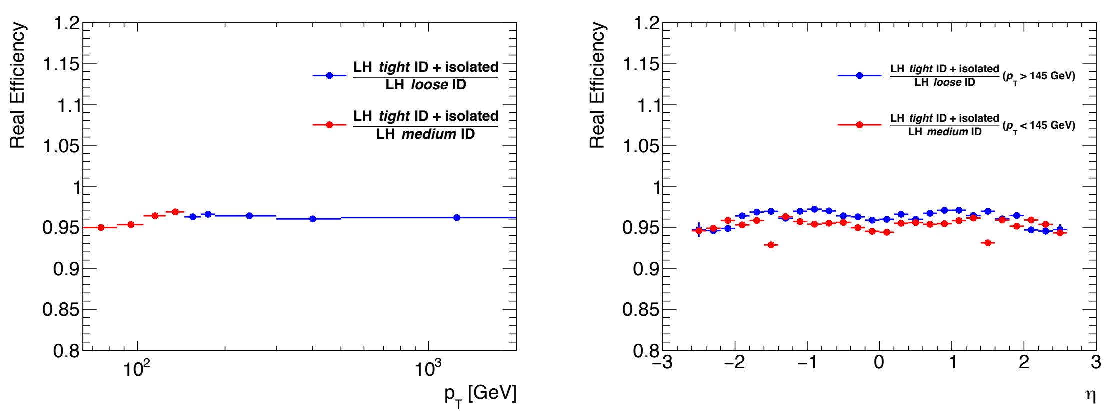

Figure 9.1. Real efficiency as a function of p_{T} and η estimated from W MC sample.

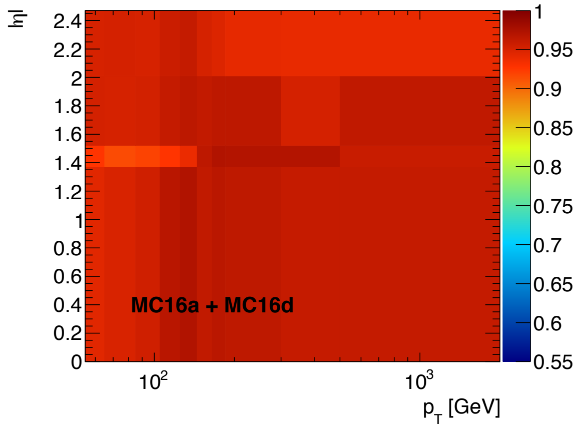

Figure 9.2. Real efficiency as a function of p_{T} and η estimated from W MC sample.

Fake Efficiency Estimation

The fake efficiency is the probability for fake electrons to pass the tight selection. The fake efficiency is estimated using data as fake electrons cannot be reliably defined in simulation as discussed in Section 7.2.4. In principle, the fake efficiency should be measured in a high purity "fake" electron sample using a set of cuts that reduce the "real" electron contamination, but getting this contamination to a negligible level is difficult. Therefore, a fake enriched sample is defined with cuts which maximize "fake" electrons, and then the "real" electron contamination is subtracted using MC samples as we rely on the MC samples to model "real" electron contributions.

The fake enriched sample is defined by modifying the following cuts with respect to the event selection described in Section 8.3 to accommodate more fake electrons. The cut on the p_{T} is kept the same as the signal sample. The cut on the $E_{\mathrm{T}}^{\mathrm{miss}}$ is changed to $E_{\mathrm{T}}^{\mathrm{miss}} <$ 60 GeV as multijet events are not expected to have a large $E_{\mathrm{T}}^{\mathrm{miss}}$ in the final state. The cut on the m_{T} is removed accordingly. In order to suppress events from Z decay, the event is rejected if the invariant mass of electron pairs falls into the mass window of 71 GeV $< m_{ee}$ $<$ 111 GeV with electrons passing the *loose* identification and $p_{\mathrm{T}} >$ 20 GeV.

The fake enriched sample still contains "real" electron contamination from processes like W or top. Hence, contributions from real electrons are subtracted for the calculation of the fake efficiency. The real electron contributions are estimated from MC in p_{T}, $E_{\mathrm{T}}^{\mathrm{miss}}$, and $\Delta\phi$ as shown in Figure 9.3 and Figure 9.4. The dilution, which shows "real" electron contributions in the fake enriched sample, for the loose selection is shown in Figure 9.3 for $p_{\mathrm{T}} < 145$ GeV on the left hand side and $p_{\mathrm{T}} > 145$ GeV on the right hand side. The dilution from real electrons is higher for $p_{\mathrm{T}} < 145$ GeV as the *medium* identification rejects more QCD jets compared to the *loose* identification for $p_{\mathrm{T}} > 145$ GeV. The shape of the $\Delta\phi$ distributions is different for $p_{\mathrm{T}} < 145$ GeV and $p_{\mathrm{T}} > 145$ GeV as W production with a back-to-back topology for $p_{\mathrm{T}} > 145$ GeV is suppressed by the $E_{\mathrm{T}}^{\mathrm{miss}} < 60$ GeV requirement for the fake enriched sample. Figure 9.4 shows the dilution in the tight selection. The dilution is higher compared to the loose selection for both p_{T} regions due to the higher background rejection in the tight selection. The fake efficiency is finally calculated using the tight selection as the numerator and the loose selection as the denominator of Equation 9.1 after subtracting the real electron dilutions.

Figure 9.5 shows the measured fake efficiencies as a function of p_{T}, η, $E_{\mathrm{T}}^{\mathrm{miss}}$, and $\Delta\phi$. Fake efficiencies are measured separately for $p_{\mathrm{T}} < 145$ GeV and for $p_{\mathrm{T}} > 145$ GeV as each p_{T} region uses different electron identification working points. The fake efficiency is much higher in the low p_{T} region ($p_{\mathrm{T}} < 145$ GeV) than the high p_{T} region ($p_{\mathrm{T}} > 145$ GeV) due to the higher probability of passing the tight selection for fake electrons with the *medium* identification than the *loose* identification. In the high p_{T} region the dependency on $E_{\mathrm{T}}^{\mathrm{miss}}$ is stable and stays around 20%, while a noticeable rise is observed in the low p_{T} region. The fake efficiency is measured for $E_{\mathrm{T}}^{\mathrm{miss}} < 60$ GeV region and applied to the $E_{\mathrm{T}}^{\mathrm{miss}} > 65$ GeV region. A contant fake efficiency is required to have a reliable estimation of fake efficiency. Thus, the fake efficiency for $p_{\mathrm{T}} < 145$ GeV could be less stable. The fake efficiency in $\Delta\phi$ increases slightly from the collinear topology to the back-to-back topology in the high p_{T} region. On the other hand, the back-to-back topology show around 20% higher fake effieciency than the collinear topology in the low p_{T} region.

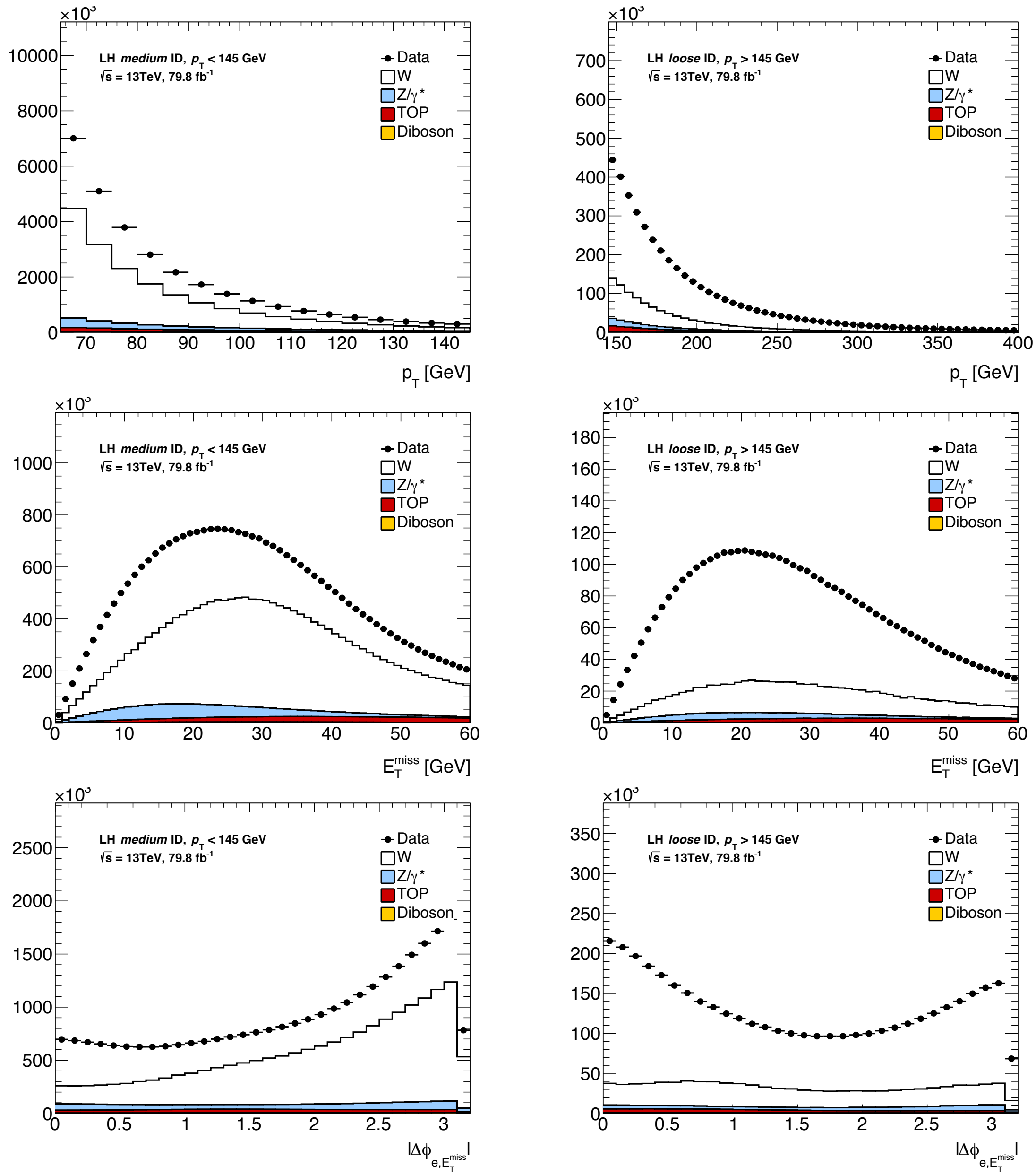

Figure 9.3. Dilution in p_{T}, $E_{\mathrm{T}}^{\mathrm{miss}}$, and $\Delta\phi$ for the loose selection with $p_{\mathrm{T}} < 145$ GeV (left) and with $p_{\mathrm{T}} > 145$ GeV (right).

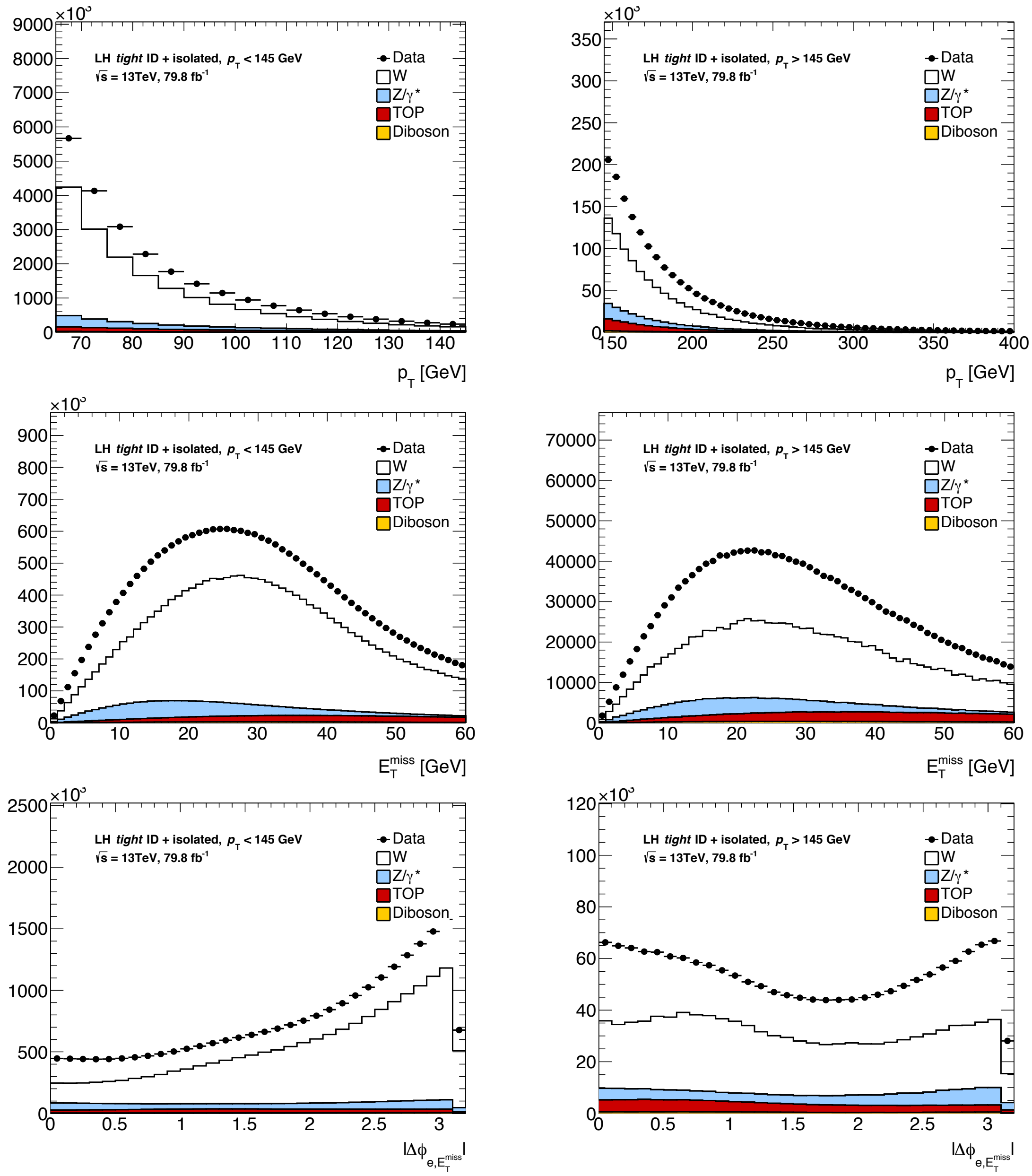

Figure 9.4. Dilution in p_T, E_T^{miss}, and $\Delta\phi$ for the tight selection with $p_T < 145$ GeV (left) and with $p_T > 145$ GeV (right).

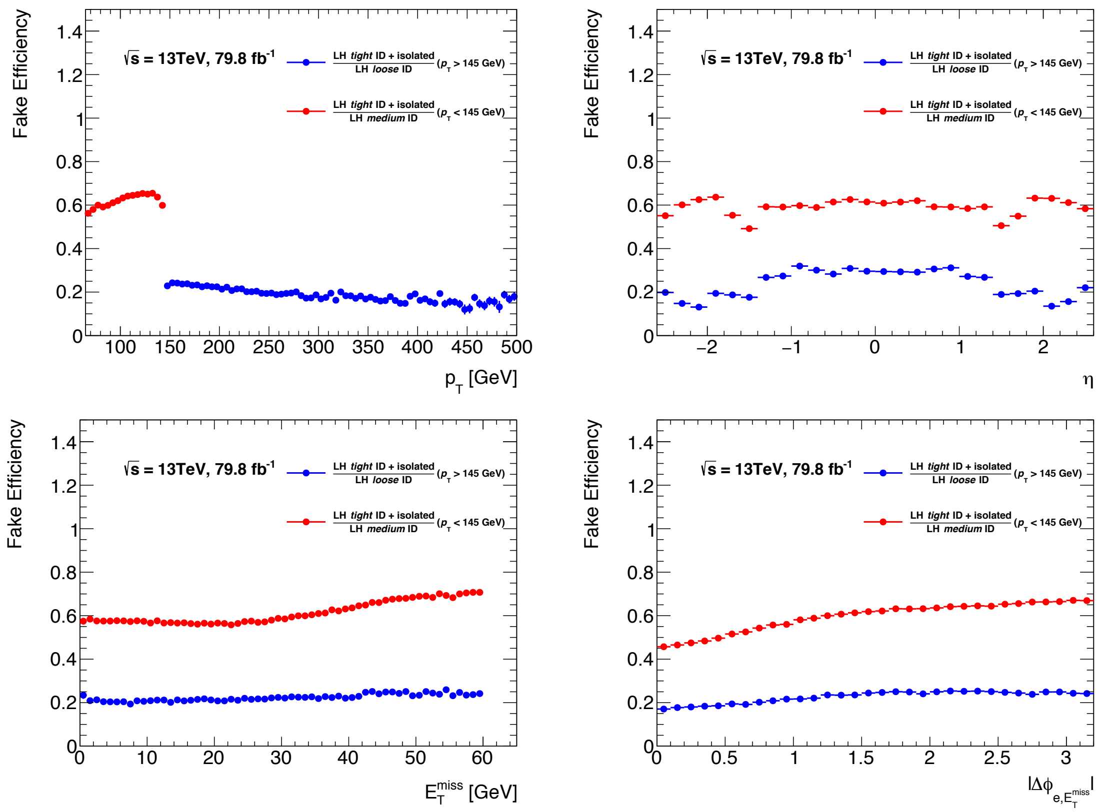

Figure 9.5. Fake efficiency as a function of p_{T}, η, $E_{\mathrm{T}}^{\mathrm{miss}}$, and $\Delta\phi$.

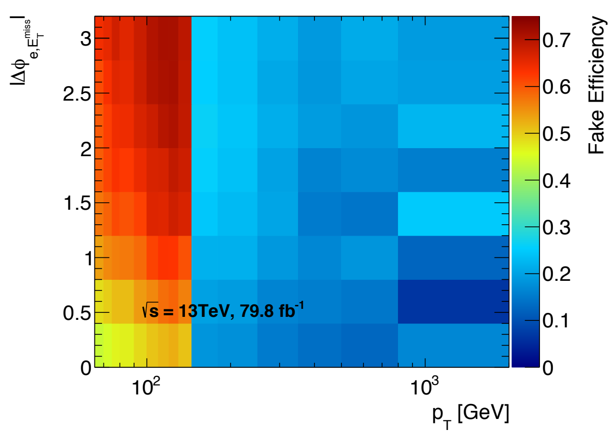

Figure 9.6. Fake efficiency as a function of $\Delta\phi$ vs. p_{T}

The two dimensional fake efficiency in $\Delta\phi$ and p_{T}, shown in Figure 9.6, is used for the fake contribution calculation in Equation 9.4. The fake efficiency is rising as $\Delta\phi$ gets closer to π, and it exceeds 70% around p_{T} of 130 GeV.

Validation of the Multijet Background

A multijet validation region is defined in order to test the method in the multijet enhanced region. The $E_{\mathrm{T}}^{\mathrm{miss}}$ and m_{T} requirements are removed as the multijet contribution is dominant in the low $E_{\mathrm{T}}^{\mathrm{miss}}$ region. Figure 9.7 shows the η, ϕ, p_{T}, $E_{\mathrm{T}}^{\mathrm{miss}}$, m_{T}, and, $\Delta\phi$ distributions for data and backgrounds in the multijet validation region. The top panels show the distributions of data and backgrounds, the middle panels show the data to the total background ratio, and the bottom panels show the fraction of certain background with respect to the total background. The η distribution shows a reasonable agreement in the central region with a slight constant underestimation of background. The holes around $|\eta|$ of 1.4 are due to the exclusion of the transition region of electromagnetic calorimeters. The different shape in the endcap region is caused by mismodeling of the shower shapes in the MC. The multijet contribution reaches 40% in the endcap region, while it stays around 20% in the barrel region. The ϕ distribution shows a very good agreement between data and backgrounds. The p_{T} distribution shows good agreement in general, and a small underestimation in MC is observed between 120 GeV and 300 GeV. The fraction of multijet contribution increases with p_{T}, and the multijet contribution is around 50% at p_{T} of 500 GeV. The $E_{\mathrm{T}}^{\mathrm{miss}}$ distribution shows a small overestimation of about 5% for $E_{\mathrm{T}}^{\mathrm{miss}} < 30$ GeV, and the background is underestimated for $E_{\mathrm{T}}^{\mathrm{miss}} > 30$ GeV by up to 10%. The data distribution peaks at a bit higher value of $E_{\mathrm{T}}^{\mathrm{miss}}$ than the background, which indicates some mismodeling of $E_{\mathrm{T}}^{\mathrm{miss}}$. The multijet background is not the main source of this mismodeling as its contribution decreases monotonically with $E_{\mathrm{T}}^{\mathrm{miss}}$ and is less than 20% of the total background. Moreover, a rise of the multijet contribution at higher $E_{\mathrm{T}}^{\mathrm{miss}}$ is very unlikely as small $E_{\mathrm{T}}^{\mathrm{miss}}$ is expected from the event topology of multijet background. The m_{T} distribution shows a reasonable agreement for $m_{\mathrm{T}} < 90$ GeV and $m_{\mathrm{T}} > 200$ GeV. The localized

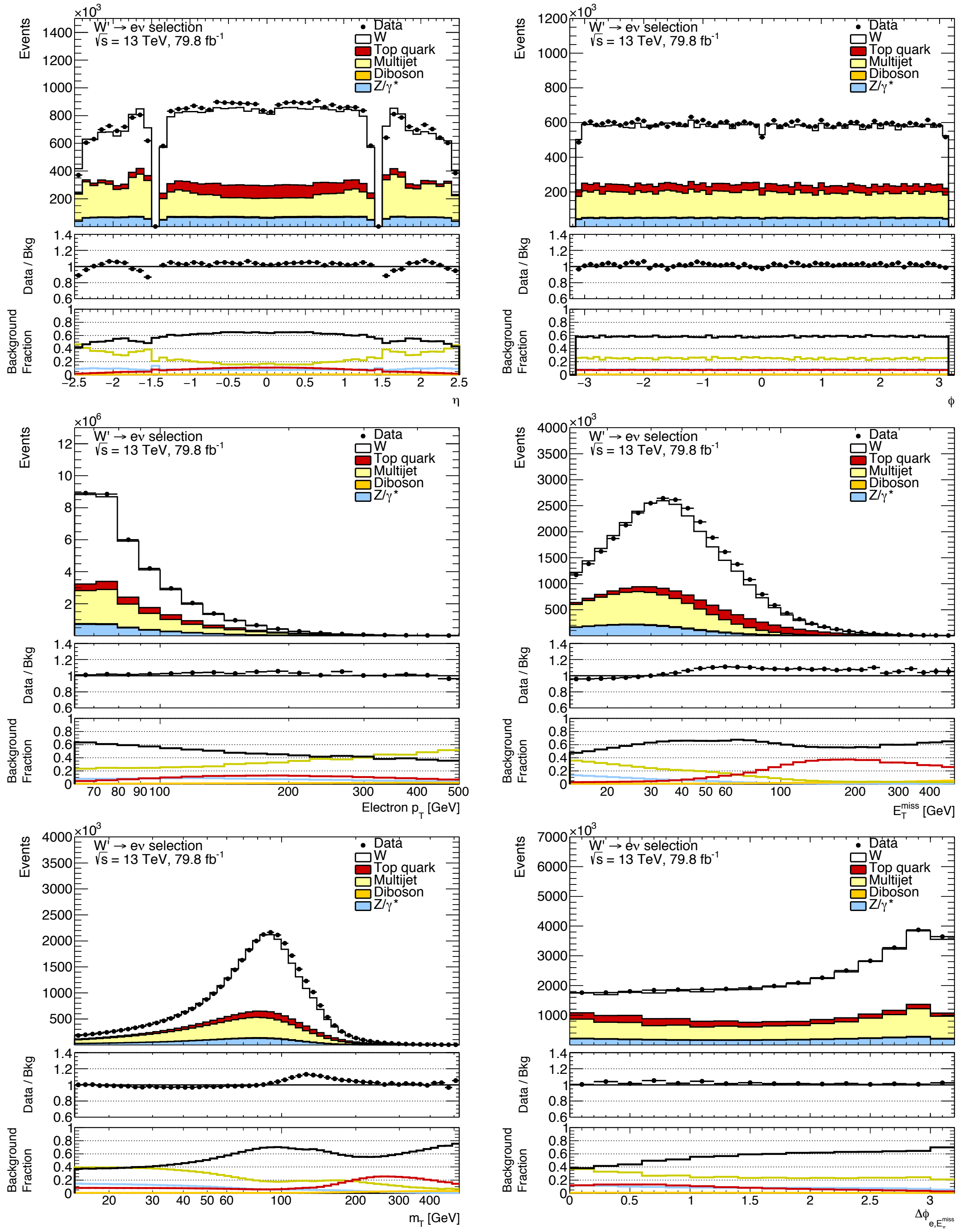

Figure 9.7. The η, ϕ, p_{T}, $E_{\mathrm{T}}^{\mathrm{miss}}$, m_{T}, and $\Delta\phi$ distributions in the multijet validation region

bump in the m_{T} distribution between 100 GeV and 200 GeV is caused by mismodeling of $E_{\mathrm{T}}^{\mathrm{miss}}$. The discrepancies are not yet fully understood and extensive studies are ongoing. As the search is focusing in the high m_{T} region, it was decided to apply a cut of $m_{\mathrm{T}} > 300$ GeV for this analysis. The $\Delta\phi$ distribution shows a good agreement. The W background prefers the back-to-back topology as expected, while the multijet background contributes uniformly.

Multijet Background in the Signal Region

Figure 9.8 shows the transverse mass distribution of the multijet background in the signal region. The distribution falls smoothly until m_{T} around 600 GeV, after which statistical

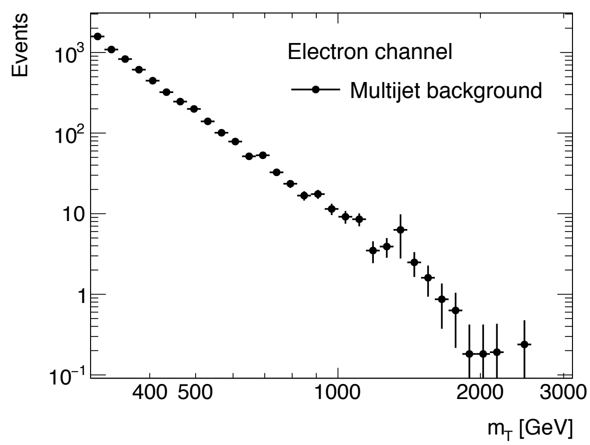

Figure 9.8. The multijet background in the electron channel

fluctuations begin to dominate. Thus, the multijet background in the high m_{T} region is estimated from an extrapolation which will be discussed in Section 9.3.

9.1.3 Multijet Background Estimation in the Muon Channel

The multijet background in the muon channel arises mainly from heavy flavor hadron decays to real muons as discussed in Section 7.2.4. The tight selection is the signal object selection described in Section 8.4.2. A loose selection is achieved by removing the isolation requirement from the signal object selection as muons from heavy flavor hadron decays tend to be surrounded by other particles from the jet associated with the hadron.

Real Efficiency Estimation

The real efficiency is estimated using muons from the W MC sample by taking the ratio of the number of muons in a given bin of p_{T} before and after the isolation requirement. The real efficiency is very high and ranges from 98.2% to 99.7% as shown in Figure 9.9.

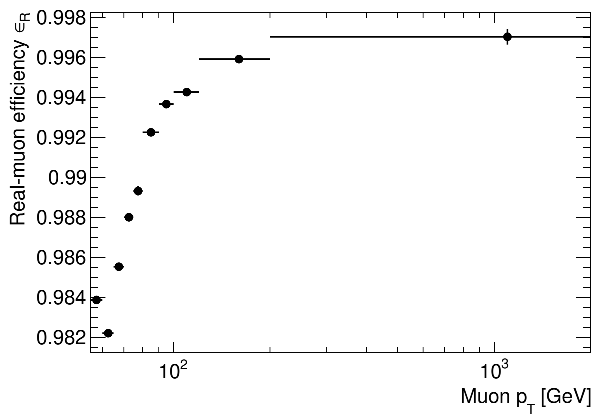

Figure 9.9. The real efficiency as a function of p_{T} in the muon channel.

Fake Efficiency Estimation

The fake efficiency is measured in a fake enriched control region using data as in the electron channel. The fake enriched control region is defined by modifying the following selections with respect to the muon selection described in Section 8.4. The cut on m_{T} is removed, and the cut on $E_{\mathrm{T}}^{\mathrm{miss}}$ is changed to $E_{\mathrm{T}}^{\mathrm{miss}} < 55$ GeV. The cut on d_0 significance is changed to d_0 significance > 1.5 to enhance heavy flavor decays to muons where the decay often produces a displace vertex and hence particles with large impact parameters. The event is also required to have at least one jet with $p_{\mathrm{T}} > 40$ GeV which does not overlap with the selected muon by requiring $\Delta R_{\mu,jet} > 0.2$, as would be present in $b\bar{b}$ production. The opening angle in the transverse plane between the muon and the $E_{\mathrm{T}}^{\mathrm{miss}}$ should be smaller than 0.5. Lastly, events with $Z \to \mu\mu$ decays are suppressed by rejecting events with two muons whose invariant mass falls in the region 80 GeV $< m_{\mu\mu} <$ 100 GeV. The real muon contribution estimated from MC in the fake enriched control region is approximately 12% in the loose selection and 52% in the tight selection. The real muon contributions are subtracted to calculate the fake efficiency. The measured fake efficiency as a function of p_{T} is shown in Figure 9.10.

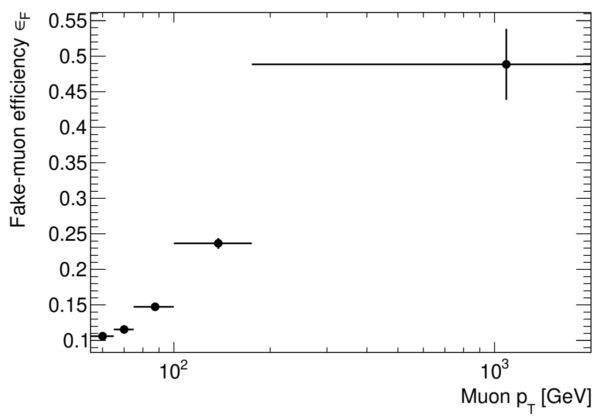

Figure 9.10. The fake efficiency as a function of p_{T} in the muon channel.

Validation of the Multijet Background

The multijet validation region is defined by removing the $E_{\mathrm{T}}^{\mathrm{miss}}$ and m_{T} selections from the signal selection described in Section 8.4. Figure 9.11 shows the number of jets with $p_{\mathrm{T}} > 40$ GeV, d_0 significance, p_{T}, $E_{\mathrm{T}}^{\mathrm{miss}}$, m_{T}, and $|\Delta\phi_{\mu,E_{\mathrm{T}}^{\mathrm{miss}}}|$ distributions for data and backgrounds in the multijet validation region. The largest discrepancy is observed in the number of jets distribution, and the disagreement is localized in the region of $2 \leq N_{jet} \leq 4$ where the W background dominates. On the other hand, the multijet background is widely distributed and reaches approximately 10% for $N_{jet} > 1$. The discrepancy observed

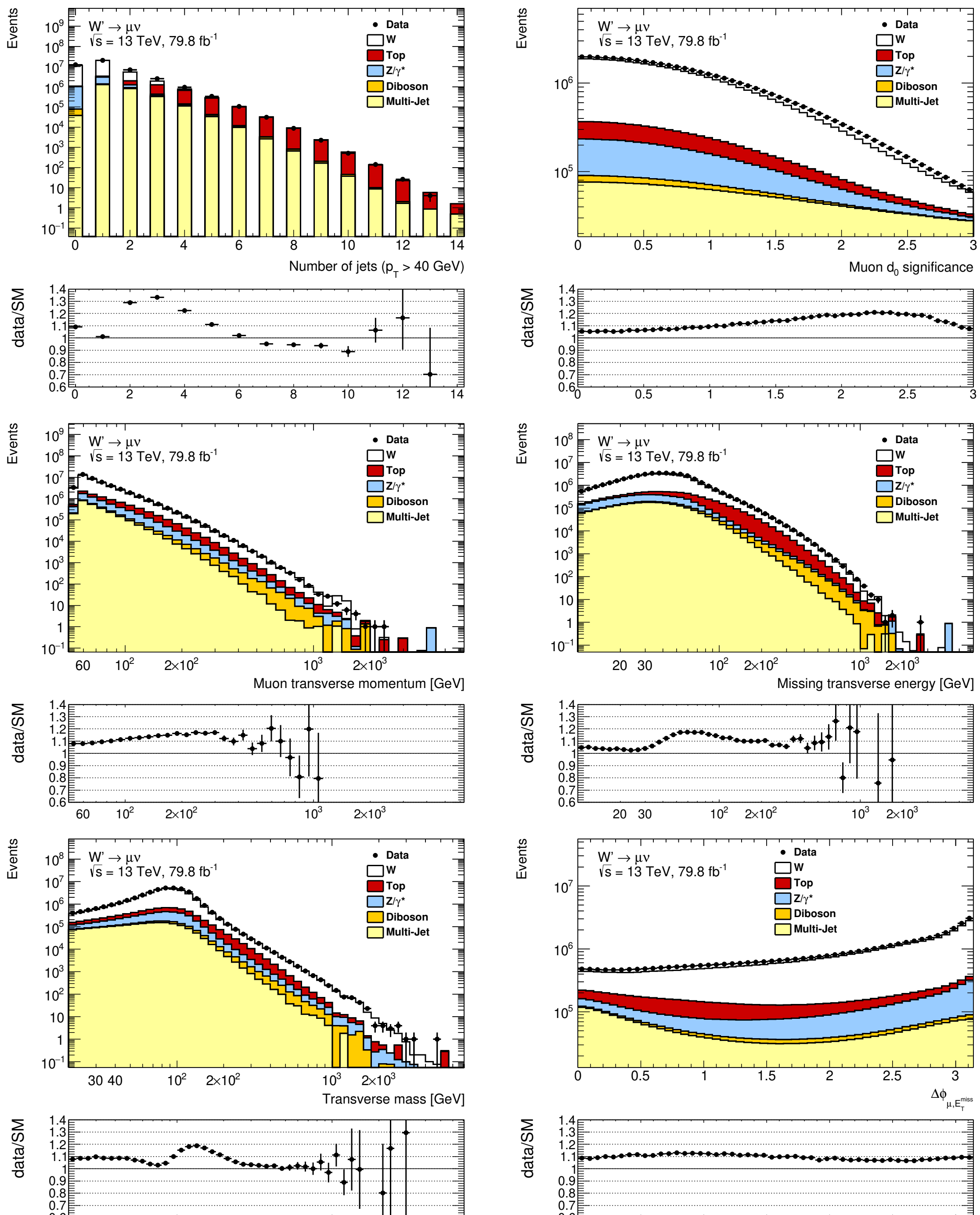

Figure 9.11. The number of jets, d_0 significance, p_{T}, $E_{\mathrm{T}}^{\mathrm{miss}}$, m_{T}, and $|\Delta\phi_{\mu,E_{\mathrm{T}}^{\mathrm{miss}}}|$ distributions in the multijet validation region

in the $E_{\mathrm{T}}^{\mathrm{miss}}$ and m_{T} distributions are very comparable with the ones in the electron channel shown in Figure 9.7. This implies that the discrepancy is driven by the W backgrounds for both channels.

Multijet Background in the Signal Region

Figure 9.12 shows the transverse mass distribution of the multijet background in the signal region. The multijet background is about a factor of three smaller in the muon

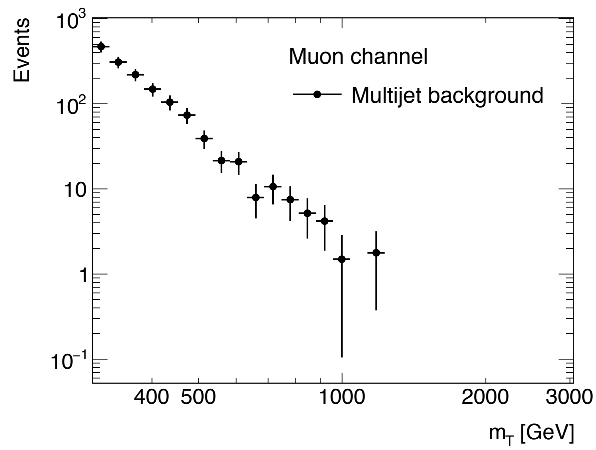

Figure 9.12. The multijet background in the muon channel

channel than the electron channel due to the smaller cross-section for heavy flavor production compared to light flavor production and the better rejection from the combined muon requirement.

9.2 Backgrounds from MC Simulation

The background contributions from W, Z/γ^{*}, top, and diboson are estimated using MC simulation as discussed in Section 7. The event selections described in Section 8.2, Section 8.3, and Section 8.4 are applied to the MC samples to estimate the background contributions in the signal region. Table 9.1 and Table 9.2 show the cut efficiency flows for each background in the electron channel and the muon channel. The efficiencies are with respect to the previous line. The numbers in parentheses are the number of events normalized to the integrated luminosity of the data, but without corrections such as K-factors, efficiency scale factors, and pileup reweighting. All samples are skimmed with the requirement of at least one electron satisfying the loose likelihood operating point with p_{T} > 60 GeV for the electron channel and at least one combined muon with $p_{\mathrm{T}} > 50$ GeV for the muon channel.

In the electron channel, cut efficiencies are quite comparable between backgrounds up to the isolation cut, as all background events contain a well-defined electron. The cut on the additional electron veto rejects more than 50% of the background events from Z and about 15% of the background from diboson which contains an additional electron in the final state. The cut on the additional muon veto rejects about 10% of events from top and diboson, but has little effect on the W and Z backgrounds. The cut on the $E_{\mathrm{T}}^{\mathrm{miss}}$ is very efficient for the background from Z as only 2.64% of events pass the cut. It also rejects about 86% of background from W as the $E_{\mathrm{T}}^{\mathrm{miss}}$ is peaking around 35 GeV. The top and diboson backgrounds are also rejected by about 60% and 70%, respectively, as one or more neutrinos are included in the final states. The most efficient cut to reject the background is the cut on the m_{T} with cut efficiencies below 5% for all backgrounds. The number of events after the m_{T} cut in Table 9.1 show the background contribution in the electron signal region.

In the muon channel, cut efficiencies show similar features as in the electron channel. Comparable efficiencies up to the isolation cut are observed. The additional muon veto rejects about 70% of the background from Z and about 15% of the background from diboson. The additional electron veto rejects about 7% of events from top and diboson. The cut on the $E_{\mathrm{T}}^{\mathrm{miss}}$ rejects 87% of the background from Z and about 80% from W. The cut efficiencies of the cut on the $E_{\mathrm{T}}^{\mathrm{miss}}$ is a bit higher in the muon channel than the electron channel, as the thresholds on p_{T} and $E_{\mathrm{T}}^{\mathrm{miss}}$ are 10 GeV lower in the muon channel. This can be also attributed to the smaller acceptance in the muon channel to detect an additional lepton.

Cut	W	Z	Top	Diboson
Total events	(3.81e+07)	(1.17e+07)	(4.31e+06)	(5.88e+05)
Event cleaning	95.24%	92.92%	100.0%	100.0%
Trigger	88.23%	88.73%	88.39%	89.66%
Pseudorapidity	99.67%	99.9%	99.98%	99.85%
Electron qualitiy	99.98%	99.99%	100.0%	99.99%
$p_{\mathrm{T}} > 65$ GeV	73.9%	73.0%	85.74%	83.59%
d_0 significance	99.55%	99.59%	99.15%	99.48%
Electron identification	93.57%	93.92%	92.6%	93.07%
Isolation	98.38%	98.44%	97.64%	98.34%
Additional electron veto	99.98%	47.12%	94.05%	84.45%
Additional muon veto	99.98%	99.94%	90.97%	89.85%
Fake jet veto	99.95%	99.95%	99.91%	99.91%
$E_{\mathrm{T}}^{\mathrm{miss}} > 65$ GeV	13.74%	2.64%	40.03%	30.52%
$m_{\mathrm{T}} > 300$ GeV	1.89% (5.59e+04)	0.77% (6.23e+02)	1.56% (1.56e+04)	4.52% (4.19e+03)
Total efficiency	0.147%	0.005%	0.362%	0.712%

Table 9.1. Cut efficiency flow in the electron channel. The efficiencies are with respect to the previous line. The numbers in parentheses are the number of events normalized to the integrated luminosity of the data, but without corrections such as K-factors, efficiency scale factors, and pileup reweighting. All samples are skimmed with the requirement of at least one electron satisfying the loose likelihood operating point with $p_{\mathrm{T}} > 60$ GeV.

The cut with the highest rejection power is the cut on m_{T} as in the electron channel with cut efficiencies below 2% for all backgrounds.

In summary, background efficiencies are mostly well below 1% for both electron and muon channels. The high background rejections are predominantly driven by the high kinematic cuts of p_{T}, $E_{\mathrm{T}}^{\mathrm{miss}}$ and, m_{T}.

Cut	W	Z	Top	Diboson
Total events	(8.40e+07)	(2.57e+07)	(5.97+e06)	(7.81e+05)
Event cleaning	100.0%	100.0%	100.0%	100.0%
Trigger	72.3%	78.8%	79.2%	79.2%
Combined muon	100.0%	100.0%	100.0%	100.0%
$p_{\mathrm{T}} > 55$ GeV	68.3%	64.7%	85.9%	83.2%
d_0 significance	99.1%	99.3%	96.9%	98.9%
$\lvert z_0 \rvert \sin\theta$	99.3%	99.7%	99.9%	99.5%
Muon identification	84.7%	85.3%	85.0%	85.0%
Muon quality	100.0%	100.0%	100.0%	100.0%
Isolation	98.8%	98.9%	96.6%	98.7%
Additional muon veto	100.0%	31.6%	94.4%	85.1%
Additional electron veto	100.0%	99.9%	92.5%	93.2%
Fake jet veto	100.0%	99.9%	99.9%	99.9%
$E_{\mathrm{T}}^{\mathrm{miss}} > 55$ GeV	19.1%	13.0%	49.1%	35.1%
$m_{\mathrm{T}} > 300$ GeV	0.7% (4.43e+04)	0.8% (3.56e+03)	0.9% (1.24e+04)	1.8% (2.07e+03)
Total efficiency	0.05%	0.01%	0.2%	0.3%

Table 9.2. Cut efficiency flow in the muon channel. The efficiencies are with respect to the previous line. The numbers in parentheses are the number of events normalized to the integrated luminosity of the data, but without corrections such as K-factors, efficiency scale factors, and pileup reweighting. All samples are skimmed with the requirement of at least one combined muon with $p_{\mathrm{T}} > 50$ GeV.

9.3 Extrapolation to High Transverse Mass

The search is performed in the region of m_{T} up to several TeV. Hence backgrounds need to be estimated with a reasonable precision up to high m_{T}. The MC samples for the background from W and Z are produced in bins of truth invariant mass to have enough statistics in the high m_{T} region as discussed in Section 7. On the other hand, the MC samples for the backgrounds from top and diboson suffer limited statistics in the high m_{T} region. The multijet background is also statistically limited in the high m_{T} region as the multijet background is estimated from data. Thus, the top, diboson, and multijet backgrounds are estimated using a fit-based background extrapolation into the region of m_{T} where the statistics is limited. Two fit functions are used to make the background extrapolation. The extrapolation functions are taken from the ATLAS searches for dijet resonances [66] and for dilepton resonances [67]:

$$f(m_{\mathrm{T}}) = e^{-a} m_{\mathrm{T}}^{b+c\log(m_{\mathrm{T}})}, \tag{9.5}$$

$$f(m_{\mathrm{T}}) = \frac{a}{(m_{\mathrm{T}}+b)^c}. \tag{9.6}$$

9.3.1 Extrapolation of the Top Background

The top backgrounds from the electron and muon channels are fitted using both functions for various fit ranges. The fit with the best $\chi^2/N_{d.o.f}$ among performed fits is chosen as the extrapolated background, and the extrapolated background replaces the background estimation in the region of high m_{T}. The top plots in Figure 9.13 show the backgrounds with all fits in the electron channel on the left-hand side and the muon channel on the right-hand side. The best fit is shown as the red dashed line and the envelope of all fits is considered as the systematic uncertainty of the extrapolation. In the electron channel, the start point of the fit range is varied from 300 GeV to 360 GeV in steps of 20 GeV, and the end point of the fit range is varied from 800 GeV to 1100 GeV in steps of 20 GeV. The fit with the range from 300 GeV to 860 GeV gives the best $\chi^2/N_{d.o.f}$, hence that fit is chosen as the extrapolated background. The extrapolated background replaces the MC background for $m_{\mathrm{T}} > 900$ GeV. In the muon channel, the start point of the fit range is varied from 300 GeV to 460 GeV in steps of 20 GeV, and the end point of the fit range is varied from 950

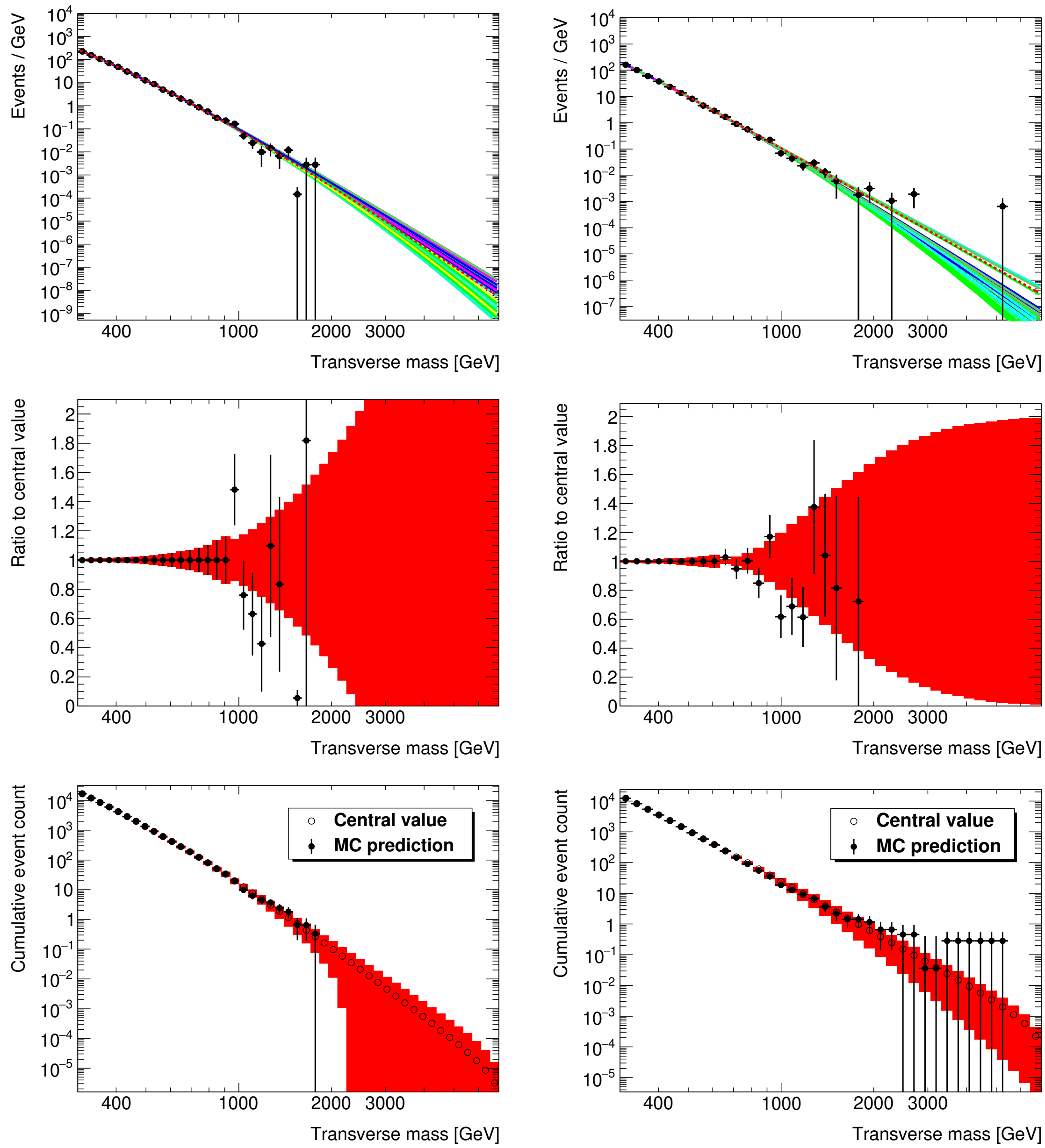

Figure 9.13. Background extrapolation of the top background in the electron channel (left) and the muon channel (right).

GeV to 2000 GeV in steps of 50 GeV. The best fit is for the fit range from 420 GeV to 950 GeV and the best fit replaces the background for $m_{\mathrm{T}} > 600$ GeV. The quality of the fits is checked from the middle and bottom plots of Figure 9.13. The middle plots show the ratio of the MC to the extrapolated background with the uncertainty band. The ratios are unity until the MC is replaced by the extrapolated background, and the uncertainty band generally covers the fluctuations. The bottom plots show the cumulative distribution of the MC and the extrapolated background. The extrapolated backgrounds agree reasonably well with the MC for both channels.

9.3.2 Extrapolation of the Diboson Background

The diboson backgrounds are extrapolated using the same method as the top background. Figure 9.14 shows the fit results of the diboson backgrounds. In the electron channel, the start point of the fit range is varied from 350 GeV to 500 GeV in steps of 20 GeV, and the end point of the fit range is varied from 1100 GeV to 1300 GeV in steps of 20 GeV. The best fit is for the fit range from 370 GeV to 1280 GeV, and the best fit replaces the background for $m_{\mathrm{T}} > 800$ GeV. In the muon channel, the start point of the fit range is varied from 300 GeV to 400 GeV in steps of 20 GeV, and the end point of the fit range is varied from 800 GeV to 1300 GeV in steps of 50 GeV. The best fit is for the fit range from 420 GeV to 950 GeV, and the best fit replaces the background for $m_{\mathrm{T}} > 600$ GeV. The ratio and cumulative plots show the extrapolated background in the electron channel agrees reasonably well with the MC. On the other hand, the extrapolated background is slightly overestimated in the muon channel as the MC populates below unity in the ratio plot but still within the uncertainty.

9.3.3 Extrapolation of the Multijet Background

The background extrapolation of the multijet background in the electron channel utilizes a different criterion to determine the best fit and the systematic uncertainty. The quantity Q is defined as:

$$Q = \frac{1}{N.o.B.} \sum_{b>b_s}^{N_b^{est}>0} \frac{\left(N_b^{est} - N_b^{fit}\right)^2}{\sigma_b^2} \tag{9.7}$$

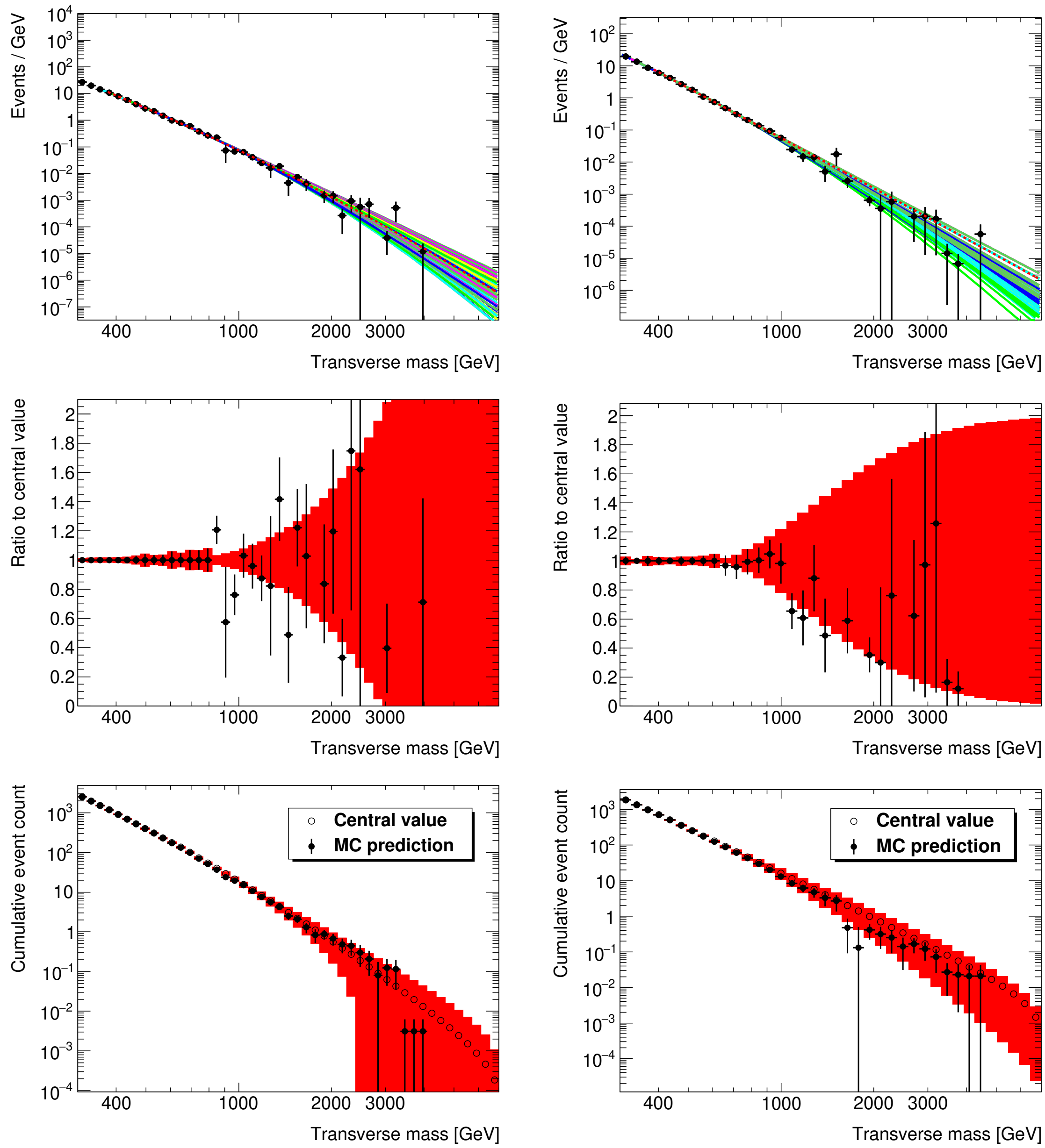

Figure 9.14. Background extrapolation of the diboson background in the electron channel (left) and the muon channel (right).

where $N.o.B.$ is the number of bins, and b_s is the bin where the fit replaces the raw estimate from the matrix method, N_b^{est} and N_b^{fit} are the number of entries in the given bin according to the matrix method and the fit, σ_b is the uncertainty in the given bin. The quantity is similar to the common χ^2 definition but it focuses on the high m_{T} tail. The fit with the lowest Q value is chosen as the extrapolated background, and the envelope of all fits with $Q < 1.5$ is considered as the systematic uncertainty of the extrapolation. The start point of the fit range is varied from 300 GeV to 400 GeV in steps of 20 GeV, and the end point of the fit range is varied from 830 GeV to 1030 GeV in steps of 25 GeV. The best fit is for the fit range from 380 GeV to 830 GeV, and the best fit replaces the background for $m_{\mathrm{T}} > 1000$ GeV. Figure 9.15 shows the fit results of the multijet background in the electron channel. The bottom plots show a reasonable agreement between the raw estimate from the matrix method and the extrapolated background. The top right plot shows the final background estimation including uncertainty band.

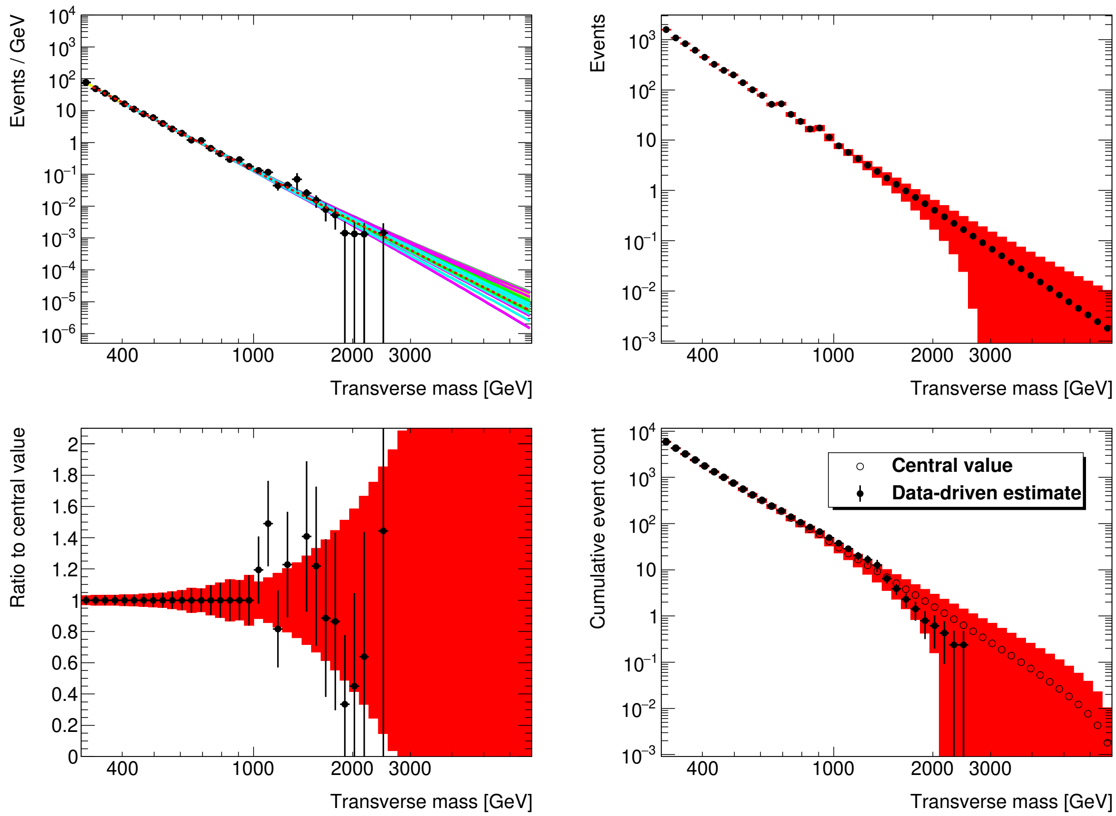

Figure 9.15. Background extrapolation of the multijet background in the electron channel.

The background extrapolation of the multijet background in the muon channel utilizes a simplified method. The fit function in Equation 9.6 is simplified as:

$$f(m_{\mathrm{T}}) = a\, m_{\mathrm{T}}^{-b}. \tag{9.8}$$

The fit is performed for the fit ranges from 300 GeV to 1000 GeV and 400 GeV to 1000 GeV, and the background is replaced by the fit for $m_{\mathrm{T}} > 500$ GeV. Figure 9.16 shows the raw background estimate from the matrix method and the fits.

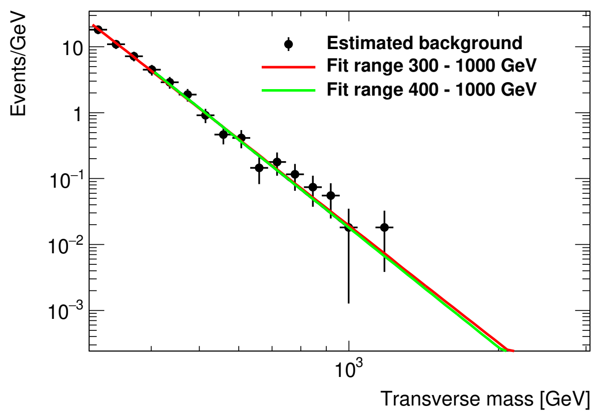

Figure 9.16. Background extrapolation of the multijet background in the muon channel.

10. Systematic Uncertainties

In this chapter, the systematic uncertainties on the background estimations and the W' signal predictions are discussed. The systematic uncertainties can be categorized as either experimental systematic or theoretical systematic. The experimental systematics originate from the method used to obtain the background or imperfect simulations or the beam conditions. The theoretical systematics arise from theoretical predictions.

A nuisance parameter is introduced for each source of systematic uncertainties. Nuisance parameters are not of direct interest (like the signal cross section), but influence the parameter of interest as both signal and background predictions depend on them.

10.1 Experimental Systematic Uncertainties

10.1.1 Electron

Systematic uncertainties on the electron are provided by the ATLAS e/γ Combined Performace (CP) group.

Electron Energy Scale

Systematic uncertainty on the electron energy scale is evaluated in MC for 60 nuisance parameters such as the calibrations of the EM calorimeter layers and the detector material. A simplified model is used in this analysis which provides one nuisance parameter with a conservative estimation of the uncertainty. The detailed procedure is described in reference [37].

Electron Energy Resolution

Systematic uncertainty on the electron energy resolution is evaluated for several nuisance parameters. A simplified model is used in this analysis which provides one nuisance parameter with a conservative estimation of the systematic uncertainty. The detailed procedure is described in reference [37].

Electron Efficiencies

Systematic uncertainties on the electron efficiencies are obtained by varying the electron selections such as an identification operating point or window of Z boson peak. The systematic uncertainties are estimated separately for the reconstruction, trigger, identification, and isolation. The detailed procedure is described in reference [33].

10.1.2 Muon

Systematic uncertainties on muons are provided by the ATLAS Muon Combined Performace (MCP) group.

Muon Momentum Scale and Resolution

Systematic uncertainties on the muon momentum resolution are estimated for several nuisance parameters, such as variations of the fit procedure and alignment. The ATLAS MCP group provides the uncertainties separately for the ID track and the MS track after summing the variations from each nuisance parameter in quadrature [68]. The systematic uncertainties on the muon momentum scale, which account for an observed charge-dependent sagitta bias, are also provided.

Muon Efficiencies

Systematic uncertainties are derived from variations of the tag and probe selection for the efficiency corrections. The ATLAS MCP group provides one nuisance parameter for the systematic uncertainty on the efficiencies. Additional uncertainty is considered due to the application of the "bad muon veto" in the *High-*p_{T} working point, which rejects muons with the large relative errors on the CB q/p measurement than the corresponding ones from the ID and the ME.

10.1.3 Jet and $E_{\mathrm{T}}^{\mathrm{miss}}$

Systematic uncertainties on the jet and $E_{\mathrm{T}}^{\mathrm{miss}}$ are provided by the ATLAS Jet/$E_{\mathrm{T}}^{\mathrm{miss}}$ CP group.

Jet Energy Scale and Resolution

Systematic uncertainties for the JES are estimated using a reduced set of three nuisance parameters derived from the full set of 80 JES systematic uncertainty terms in the calibration [40]. As this analysis is not strongly dependent on the jet identification criteria, this reduced set of JES systematic parameters is adequate to capture JES-related effects. The correction on the jet energy resolution (JER) is not applied to MC in this analysis, and the systematic uncertainty on the JER is provided as one nuisance parameter.

$E_{\mathrm{T}}^{\mathrm{miss}}$ Scale and Resolution

Systematic uncertainties on the $E_{\mathrm{T}}^{\mathrm{miss}}$ scale and resolution are provided for the soft term contribution to the $E_{\mathrm{T}}^{\mathrm{miss}}$ [47], as the systematic uncertainties of each hard term such as electron, muon, and jet are propagated to the $E_{\mathrm{T}}^{\mathrm{miss}}$ calculation.

10.1.4 Pile-up

Pile-up scaling is applied to data in order to have a comparable performance of pile-up-dependent physics observables at a given pile-up condition. The systematic uncertainty on the scale factor is provided by the ATLAS Physics Modeling group, which is based on the uncertainty on the ratio between the predicted and measured inelastic cross sections [69].

10.1.5 Luminosity

Systematic uncertainty on the integrated luminosity for the 2015-2017 dataset is 2.0%, which is provided by the ATLAS Luminosity group. It is derived from a similar methodology described in reference [70], and using the LUCID-2 detector [71] for the baseline measurements.

10.1.6 Multijet Background Estimation

Systematic uncertainty on the multijet background is estimated separately for both electron and muon channels.

Electron Channel

Systematic uncertainty of the multijet background predominantly originates from the fake efficiency as the selections to determine the fake enriched sample could change the composition of the fake enriched sample. On the other hand, the real efficiency is very stable as truth electrons are solely involved in the measurement. Thus, the selection which defines the fake enriched sample is varied with respect to the nominal selection, which is described in Section 9.1.2, to obtain the fake efficiency variations. The following changes in the selection of the fake enriched sample are performed:

- $E_{\mathrm{T}}^{\mathrm{miss}} < 20$ GeV.
- $20 < E_{\mathrm{T}}^{\mathrm{miss}} < 60$ GeV.

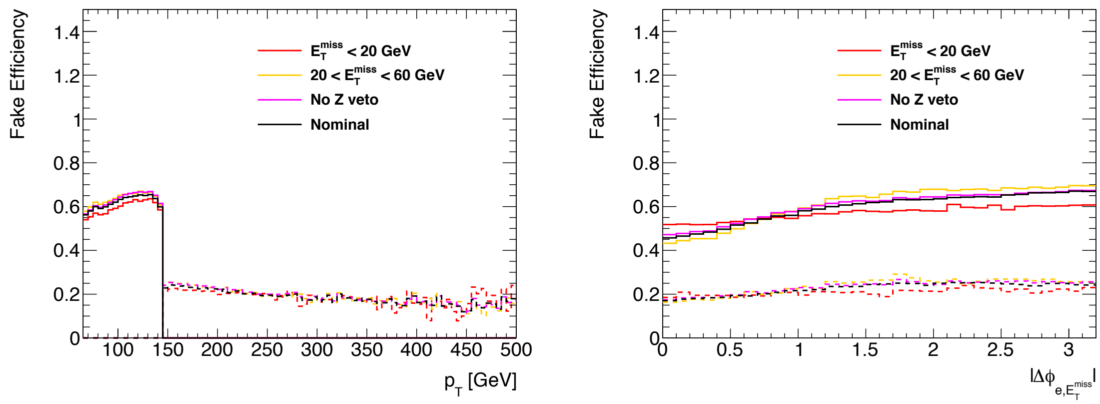

Figure 10.1. Fake efficiency variations as a function of p_{T} and $\Delta\phi$ from the fake enriched samples. The solid and dashed lines correspond to $p_{\mathrm{T}} < 145$ GeV and $p_{\mathrm{T}} > 145$ GeV respectively.

- Remove the Z veto.

Figure 10.1 shows the fake efficiency variations including the nominal selection. The impact of having events from Z bosons (no Z veto) is marginal, and a slight rise in the p_{T} between 100 GeV and 140 GeV is observed due to real electrons from Z decay. The largest change arises from the $E_{\mathrm{T}}^{\mathrm{miss}} < 20$ GeV variation. The dependency on $\Delta\phi$ is less pronounced with the $E_{\mathrm{T}}^{\mathrm{miss}} < 20$ GeV variation as the fake enriched sample contains more multijet events.

The relative uncertainties on the multijet backgrounds for the three fake efficiency variations at final selection are shown on the left-hand side of Figure 10.2. The largest deviation is observed for the variation of $E_{\mathrm{T}}^{\mathrm{miss}}$ which leads to a total difference of about 20% at m_{T} around 1 TeV. Therefore, the uncertainty of the multijet background is assumed to be 20% over the whole transverse mass range. The ratio of the total background with the fake efficiency variations to the nominal is shown on the right-hand side of Figure 10.2. The impact on the total background is below 3% over the whole transverse mass range.

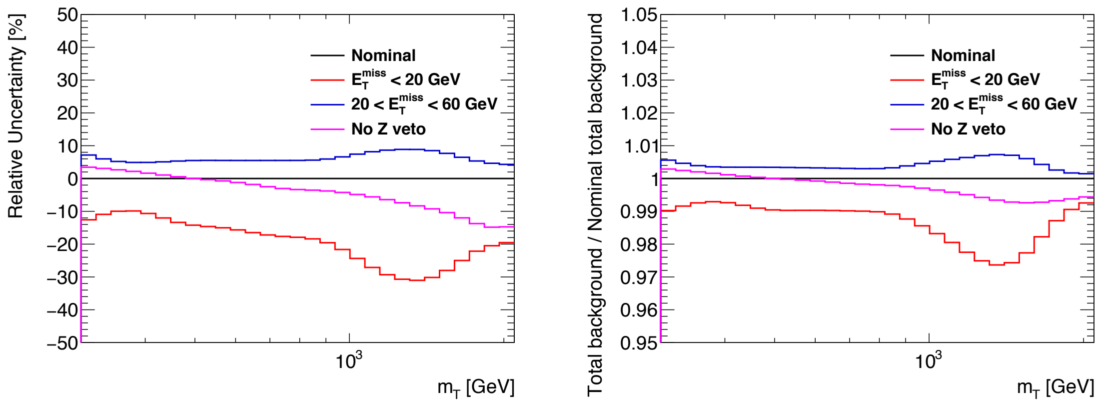

Figure 10.2. Relative uncertainty of the multijet backgrounds as a function of $E_{\mathrm{T}}^{\mathrm{miss}}$ for the fake efficiency variations at final selection (left). The ratio of the total background with the fake efficiency variations to the nominal at final selection (right).

Muon Channel

Systematic uncertainty of the multijet background is estimated from the variations of fake and real efficiency. As a systematic variation, the real efficiency is measured from data using the tag-and-probe method with muon pairs in the invariant mass window of $80 < m_{\mu\mu} < 102$ GeV. The variations of fake efficiency are performed by the following changes with respect to the nominal selection, which is described in Section 9.1.3, of the fake enriched sample:

- Remove the Z veto and $\Delta\phi_{\mu,E_{\mathrm{T}}^{\mathrm{miss}}}$ cuts.
- Remove the Z veto and $\Delta\phi_{\mu,E_{\mathrm{T}}^{\mathrm{miss}}}$ cuts, but tighten the d_0 significance cut to 2.
- Remove the d_0 significance cut.
- Use a tighter d_0 significance cut of 2.
- Remove the jet requirement.
- Remove the jet requirement, but tighten the d_0 significance cut to 2.
- $E_{\mathrm{T}}^{\mathrm{miss}} < 20$ GeV.

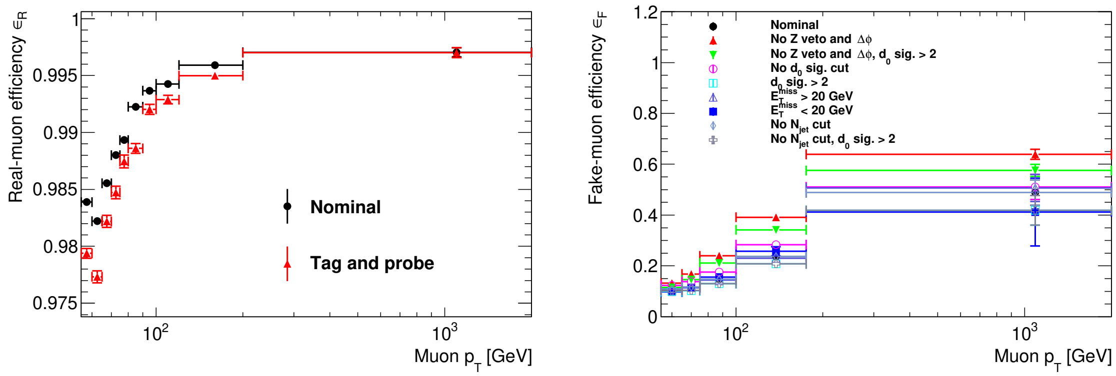

Figure 10.3. The real efficiency (left) and the fake efficiency (right) as a function of p_{T} for the systematic variations.

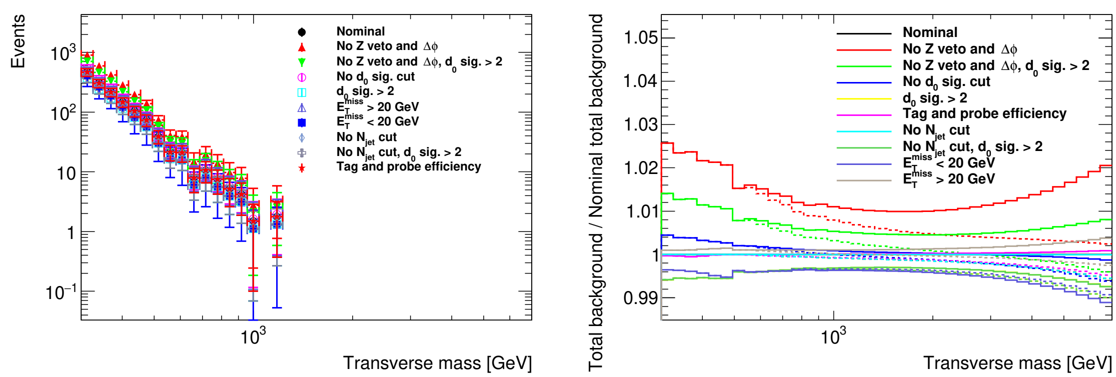

Figure 10.4. The multijet backgrounds in the m_{T} distribution at final selection under all systematic variations (left). The ratio of the total background with the systematic variations to the nominal (right). The different line styles in the right-hand side plot respresent different background extraploation ranges.

- $20 < E_{\mathrm{T}}^{\mathrm{miss}} < 55$ GeV.

The real efficiency variation is shown on the left-hand side of Figure 10.3. The difference between the two methods is marginal as only about 0.1% difference is observed in the average efficiency. On the other hand, relatively large changes are observed from the fake efficiency variations as shown on the right-hand side of Figure 10.3. The impact is largest for the selection without Z veto and $\Delta\phi_{\mu,E_{\mathrm{T}}^{\mathrm{miss}}}$ cuts.

The multijet backgrounds in the m_{T} distribution at final selection including all systematic variations are shown on the left-hand side of Figure 10.4. Finally, the ratio of the total background with the fake efficiency variations to the nominal is shown on the right-hand side of Figure 10.4. The different line styles represent different background extrapolation ranges for the multijet backgrounds. The solid and dashed lines correspond to the range 300 - 1000 GeV and 400 - 1000GeV, respectively. The most significant deviation, solid red line, is used as the systematic uncertainty on the multijet background. Even though there is a relatively large uncertainty in the fake efficiency, the impact to the total background is below 3% due to the small contribution of the multijet background to the total background.

10.1.7 Extrapolation

Systematic uncertainties on the extrapolation of the top, diboson, and the multijet backgrounds are obtained from the envelope of fits to extrapolate the backgrounds as discussed in Section 9.3.

10.2 Theoretical Systematic Uncertainties

10.2.1 W and Z Backgrounds

PDF Uncertainty

The PDF uncertainty of the CT14 NNLO PDF set is estimated from the uncertainty at the 90% confidence level as a function of the boson mass. A re-diagonalized set of seven PDF eigenvectors, which are provided by the authors of the CT14 PDF using MP4LHC, are used rather than the original 28 CT14 uncertainty eigenvectors [72].

Several PDFs are compared for the W cross section, and the CT14 PDF uncertainties do not cover the differences to the NNPDF3.0 prediction. Thus, a systematic uncertainty on the PDF choice for the NNPDF3.0 is also considered.

α_s Uncertainty

The uncertainty of α_s is assumed to be ± 0.003, which is two times larger than the uncertainty recommended by the PDF4LHC group [73] for $\alpha_s(m_Z^2)$ at the 68% confidence level.

Electroweak Uncertainty

The uncertainty of the electroweak corrections is estimated by comparing different approaches to calculate the final correction factor. The additive approach $(1+\delta_{EW}+\delta_{QCD})$ is taken as the central value as discussed in Section 7.1.1, and the difference from the multiplicative approach $((1+\delta_{EW})\times(1+\delta_{QCD}))$ is taken as a systematic uncertainty.

10.2.2 Top and Diboson Backgrounds

The uncertainty on the top backgrounds is taken to be 6% for the cross section, which is primarily derived from the uncertainty of the $t\bar{t}$ background. The uncertainties on the cross section of diboson backgrounds are about 5-10% [74], and these are neglected due to the small contribution to the total background.

10.3 Summary

The scale of each systematic uncertainty as a function of transverse mass is discussed in the following. Systematic uncertainties are calculated on the total background for each nuisance parameter as:

$$\text{Systematic uncertainty[\%]} = \frac{\text{variation - nominal}}{\text{nominal}} \times 100. \tag{10.1}$$

Figure 10.5 shows the experimental uncertainties in the electron on the left-hand side and the muon on the right-hand side. The electron energy scale uncertainty is about 3% from low m_{T} to very high m_{T} around 3 TeV. The electron identification and isolation uncertainties stay

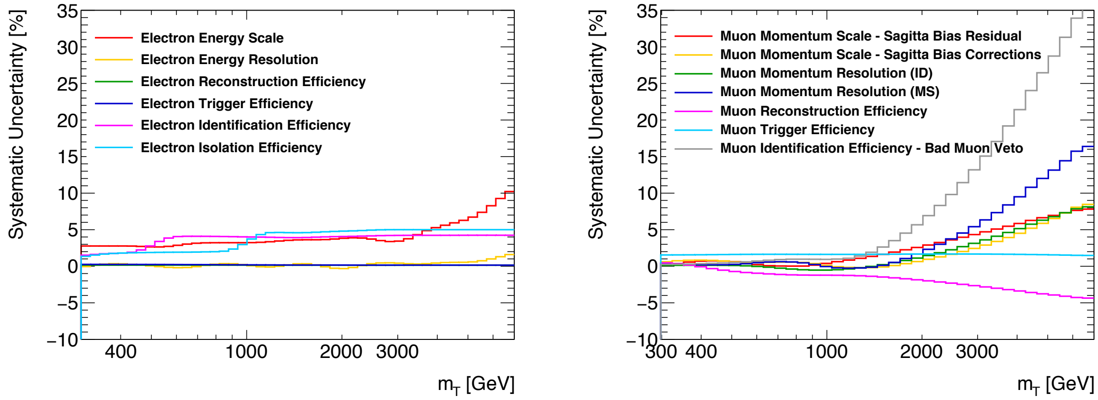

Figure 10.5. Experimental systematic uncertainties on the electron (left) and the muon (right).

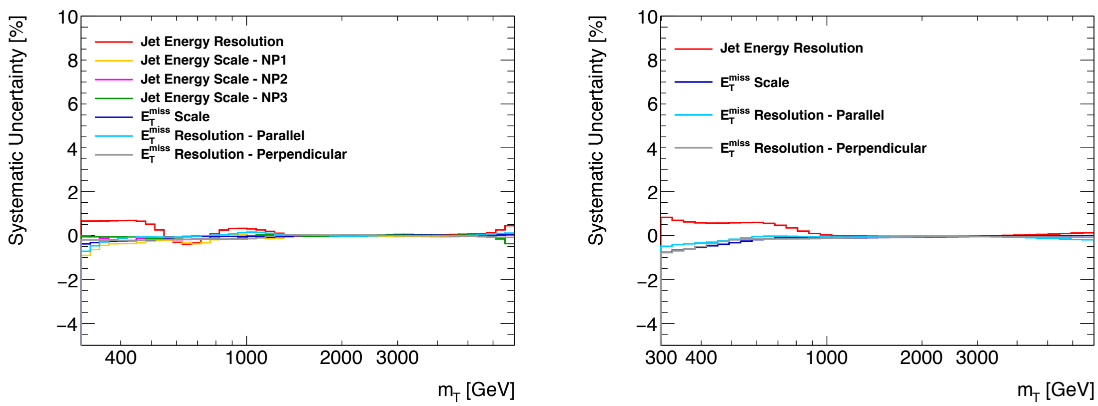

Figure 10.6. Experimental systematic uncertainties on the jet and $E_{\mathrm{T}}^{\mathrm{miss}}$ in the electron channel (left) and the muon channel (right).

below 2% for m_{T} less than 500 GeV and reach about 5% in the higher m_{T} region where the statistical uncertainty of data dominates. Thus, only the electron energy scale uncertainty is considered. The uncertainties in the muon channel are below 2% up to m_{T} around 1 TeV and become sizable in the higher m_{T} region. Figure 10.6 shows the experimental uncertainties on the jet and $E_{\mathrm{T}}^{\mathrm{miss}}$ in the electron channel on the left-hand side and the muon channel on the right-hand side. The uncertainty on the jet energy resolution is largest but still stays below 1% over the whole m_{T} range for both channels. Thus, the uncertainties on the jet and

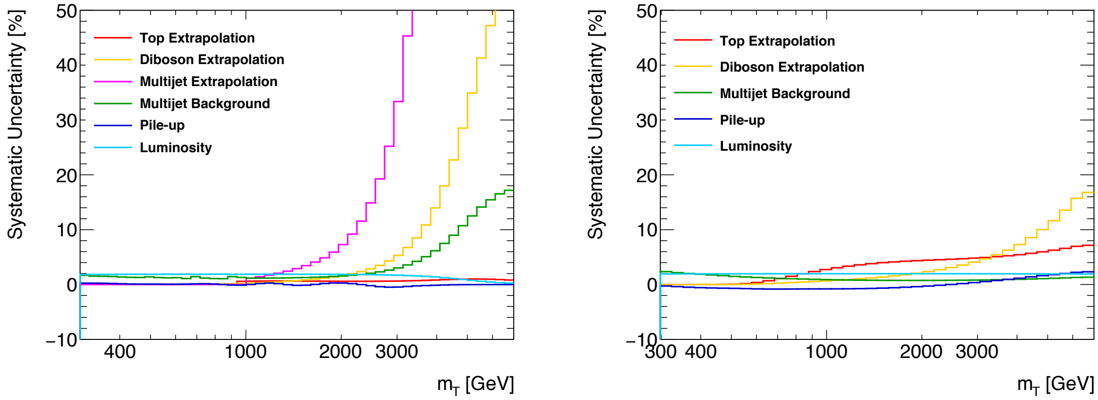

Figure 10.7. Experimental systemtic uncertainties on the background extrapolation, pile-up, and luminosity in the electron channel (left) and the muon channel (right).

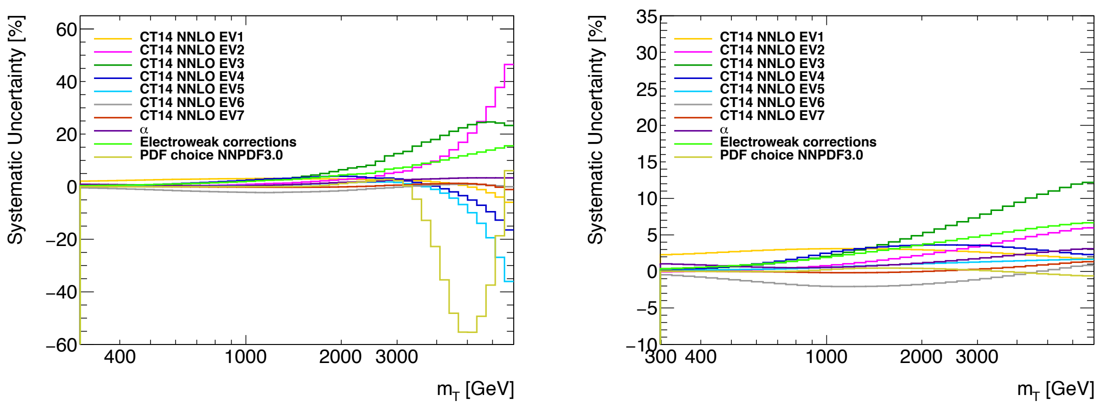

Figure 10.8. Theoretical systematic uncertainties in the electron channel (left) and the muon channel (right).

$E_{\mathrm{T}}^{\mathrm{miss}}$ are neglected. Figure 10.7 shows the experimental uncertainties of the background extrapolation, pile-up, and luminosity in the electron channel on the left-hand side and the muon channel on the right-hand side. The uncertainties of the multijet background and luminosity are about 2% in the low m_{T} region in both channels. The uncertainties of the multijet and diboson extrapolation are the dominant uncertainty in the high m_{T} region in the electron channel. On the other hand, the uncertainties of the background extrapolation are relatively small in the muon channel. The uncertainty of the pile-up is neglected for both channels. Figure 10.8 shows the theoretical uncertainties in the electron channel on the left-hand side and the muon channel on the right-hand side. The uncertainties of the CT14 PDF eigenvectors are similar between electron and muon channels, and the differences in the shapes are due to the worse resolution in the muon channel. The largest uncertainty in the electron channel is the PDF choice, which reaches up to 55% at m_{T} around 5 TeV. The uncertainty of the α_s is neglected.

All the systematic uncertainties considered in the analysis are listed in Table 10.1. The experimental uncertainties are applied to the backgrounds and the W' signal predictions. On the other hand, the theoretical uncertainties are applied only to the backgrounds in order to reduce the bias of a specific W' model for the search.

	$W' \to e\nu$	$W' \to \mu\nu$	Correlated between channels
Electron Energy Scale	applied	n/a	-
Electron Energy Resolution	neglected	n/a	-
Muon Momentum Scale (RHO)	n/a	applied	-
Muon Momentum Scale (RESBIAS)	n/a	applied	-
Muon Momentum Resolution (ID)	n/a	applied	-
Muon Momentum Resolution (MS)	n/a	applied	-
Lepton Trigger Efficiency	neglected	applied	no
Lepton Reconstruction Efficiency	neglected	applied	-
Lepton Selection Efficiency	neglected	applied	-
Jet Energy Resolution	neglected	neglected	-
Jet Energy Scale NP1	neglected	neglected	-
Jet Energy Scale NP2	neglected	neglected	-
Jet Energy Scale NP3	neglected	neglected	-
$E_{\mathrm{T}}^{\mathrm{miss}}$Resolution Parallel	neglected	neglected	-
$E_{\mathrm{T}}^{\mathrm{miss}}$Resolution Perpendicular	neglected	neglected	-
$E_{\mathrm{T}}^{\mathrm{miss}}$Scale	neglected	neglected	-
Pile-up	neglected	neglected	-
Luminosity	applied	applied	yes
QCD Background	applied	applied	no
QCD Extrapolation	applied	neglected	-
Top Background	applied	applied	yes
Top Extrapolation	applied	applied	no
Diboson Extrapolation	applied	applied	no
CT14 NNLO EV1	applied	applied	yes
CT14 NNLO EV2	applied	applied	yes
CT14 NNLO EV3	applied	applied	yes
CT14 NNLO EV4	applied	applied	yes
CT14 NNLO EV5	neglected	neglected	-
CT14 NNLO EV6	neglected	neglected	-
CT14 NNLO EV7	neglected	neglected	-
PDF Choice NNPDF3.0	applied	applied	yes
α_s	neglected	neglected	-
Electroweak Corrections	applied	applied	-

Table 10.1. Summary of the systematic uncertainties and correlations between channels.

Source	Electron channel		Muon channel	
	Background	Signal	Background	Signal
Trigger	negl. (negl.)	negl. (negl.)	1% (1%)	2% (2%)
Lepton reconstruction and identification	negl. (negl.)	negl. (negl.)	7% (21%)	5% (29%)
Lepton momentum scale and resolution	4% (3%)	4% (3%)	3% (12%)	7% (10%)
Multijet background	7% (113%)	N/A (N/A)	1% (1%)	N/A (N/A)
Top extrapolation	2% (5%)	N/A (N/A)	3% (3%)	N/A (N/A)
Top normalization	<0.5% (<0.5%)	N/A (N/A)	<0.5% (<0.5%)	N/A (N/A)
Diboson extrapolation	2% (9%)	N/A (N/A)	3% (10%)	N/A (N/A)
PDF choice for DY	1% (14%)	N/A (N/A)	<0.5% (<0.5%)	N/A (N/A)
PDF variation for DY	8% (12%)	N/A (N/A)	7% (11%)	N/A (N/A)
EW corrections for DY	4% (5%)	N/A (N/A)	4% (6%)	N/A (N/A)
Luminosity	2% (1%)	2% (2%)	2% (2%)	2% (2%)
Total	13% (115%)	4% (4%)	12% (29%)	9% (31%)

Table 10.2. Systematic uncertainties in the expected number of events as estimated for the total background and for signal with a W'_{SSM} mass of 2 (4) TeV. The uncertainty is estimated with the binning shown in Figure 10.5 to 10.8 at $m_{\mathrm{T}} = 2$ (4) TeV for the background and in a three-bin window around $m_{\mathrm{T}} = 2$ (4) TeV for the signal. Uncertainties that are not applicable are denoted "N/A", and "negl." means that the uncertainty is not included in the statistical analysis. Sources of uncertainties not included in the table are neglected in the statistical analysis.

11. Results

Using the event selection in Section 8, the background estimation in Section 9, and the estimation of systematic uncertainties in Section 10, the total background estimate and its uncertainty is compared to data to search for a new heavy gauge boson in the electron or muon and $E_{\mathrm{T}}^{\mathrm{miss}}$ final states.

Figure 11.1 shows the η, ϕ, p_{T}, and $E_{\mathrm{T}}^{\mathrm{miss}}$ distributions after the final signal selection in the $W' \to e\nu$ channel. The contribution from W is dominant over the whole range. The top background is the second largest in the central region, while the multijet background becomes the second largest in the forward region ($|\eta| > 1.5$). The ratio of data to the total background shows a good agreement over the whole η range within the systematic uncertainty which is shown as the gray hashed band. The ϕ distribution shows a flat distribution over the whole ϕ range, and a reasonable agreement within the systematic uncertainty. The p_{T} distribution shows a steep rise from 65 GeV to 150 GeV and then drops sharply to around 2 TeV. The shape of the p_{T} distribution originates from the cut on m_{T} at 300 GeV, which rejects a large fraction of events with $p_{\mathrm{T}} < 150$ GeV. Similar behavior is observed in the $E_{\mathrm{T}}^{\mathrm{miss}}$ distribution, although the rise below 150 GeV is relatively gentle due to the worse resolution in $E_{\mathrm{T}}^{\mathrm{miss}}$. The background composition changes noticeably in both p_{T} and $E_{\mathrm{T}}^{\mathrm{miss}}$. While the W background is the largest overall, the top background dominates in the low p_{T} region as multiple particles share the initial transverse momentum of a top quark and the multijet background becomes the primary background in the high p_{T} region due to misidentified leptons as discussed in Section 7.2.4. A similar behavior is observed between the diboson and Z/γ^* backgrounds. The diboson background tends to populate a lower p_{T} region than the Z/γ^* background. The corresponding behavior is observed for the background composition in the $E_{\mathrm{T}}^{\mathrm{miss}}$ distribution. The dominant background in the low $E_{\mathrm{T}}^{\mathrm{miss}}$ region is the multijet background as no neutral particles are expected in multijet events. Agreement between data and background is reasonably good within the

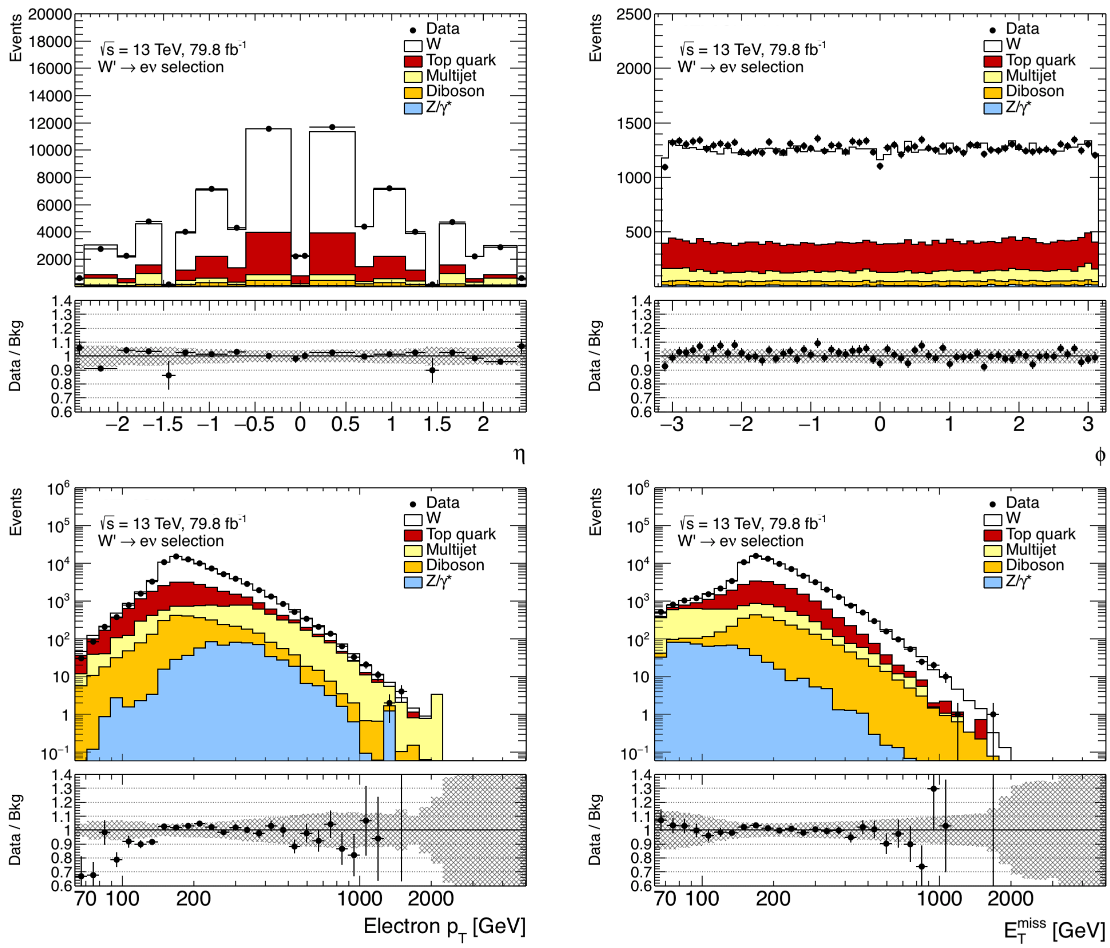

Figure 11.1. Electron η (left top), ϕ (right top), p_{T} (left bottom), and $E_{\mathrm{T}}^{\mathrm{miss}}$ (right bottom) distributions at the signal selection in the $W' \rightarrow e\nu$ channel.

systematic uncertainty for both the p_{T} and $E_{\mathrm{T}}^{\mathrm{miss}}$ distributions except in the low p_{T} region. The background overestimation in the low p_{T} region can be attributed to the multijet background. The discontinuity at p_{T} around 150 GeV in the ratio panel corresponds to the substantial change in the fake efficiency as shown in Figure 9.5. A detailed study can be found in Appendix B.

Figure 11.2 shows the η, ϕ, p_{T}, and $E_{\mathrm{T}}^{\mathrm{miss}}$ distributions after the final signal selection in the $W' \rightarrow \mu\nu$ channel. The average contribution of each background is in the following order: W, top, Z/γ^{*}, diboson, and multijet. The η distribution shows dips at $|\eta|$ around

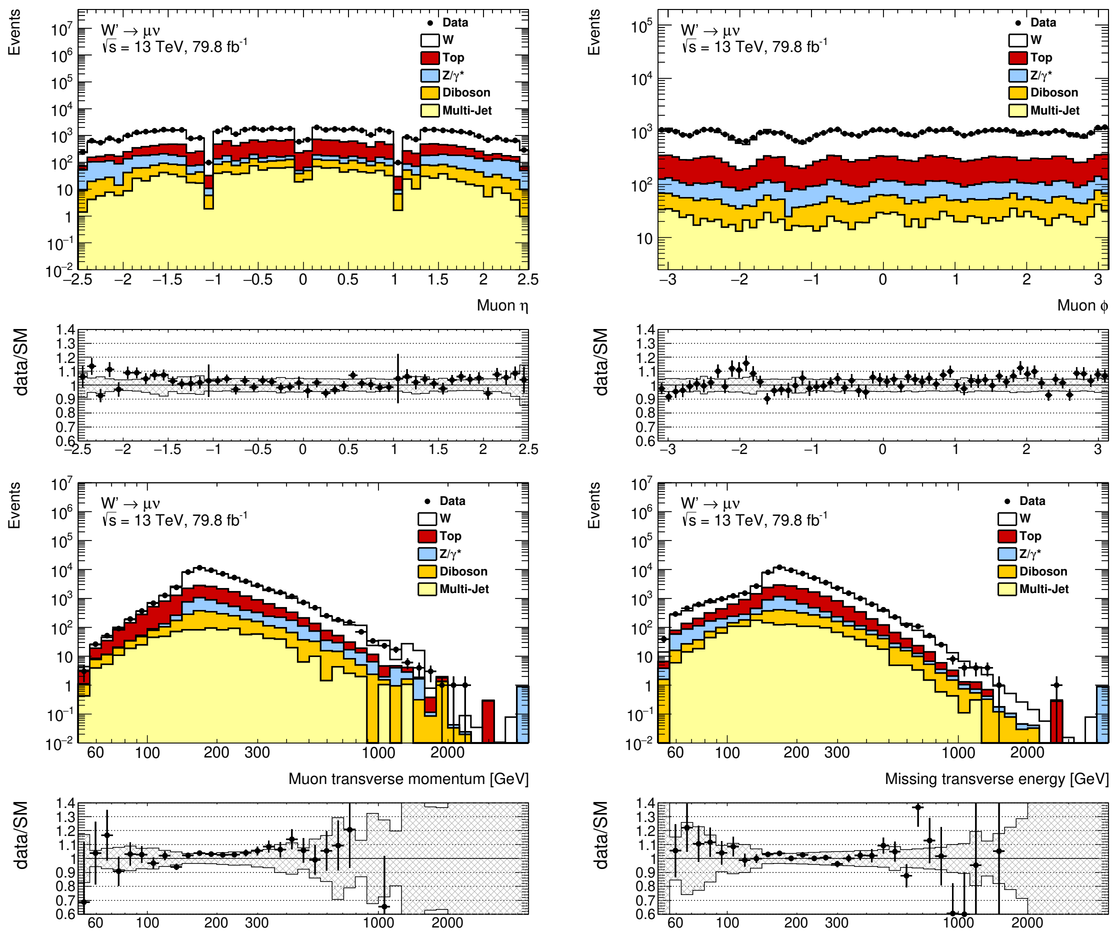

Figure 11.2. Muon η (left top), ϕ (right top), p_{T} (left bottom), and $E_{\mathrm{T}}^{\mathrm{miss}}$ (right bottom) distributions at the signal selection in the $W' \to \mu\nu$ channel.

1, which are caused by the high-p_{T} muon identification as discussed in Section 4.3.2. The dip at η around 0 is due to the detector services. The top background is the second largest background in the central region as observed in the electron channel, while the multijet background is the smallest background in the muon channel as jets cannot reach muon chambers as discussed in Section 7.2.4. The Z/γ^* background contribution becomes evident in the forward region, unlike in the electron channel. In case of the $Z/\gamma^* \to \mu\mu$ event, one of two muons can be lost due to the MS acceptance up to $|\eta| = 2.7$, thus the missing muon in the event can lead a large fake $E_{\mathrm{T}}^{\mathrm{miss}}$. In case of the $Z/\gamma^* \to ee$ event, one of two electrons can be still reconstructed as jet due to large acceptance of the calorimeter up to $|\eta| = 4.9$, thus the event is unlikely to pass the signal selection. The agreement between data and background is reasonably good over the whole η range. The ϕ distribution shows a ripple structure which arises from the structure of toroid magnets in the MS. The more pronounced dips at ϕ around -2 and -1 correspond to the feet which support the ATLAS detector. The p_{T} and $E_{\mathrm{T}}^{\mathrm{miss}}$ distributions show a steep rise from 55 GeV to 150 GeV and then fall steeply to 2 TeV as observed in the electron channel. The background composition as a function of p_{T} and $E_{\mathrm{T}}^{\mathrm{miss}}$ is similar to the electron channel for the W and the top backgrounds.

Figure 11.3 shows the transverse mass distributions in the electron and muon channels. The expected SSM W' signal distributions for 3, 4, and 5 TeV masses are also shown on top of the SM background prediction. The Jacobian peaks of the W' signal are much wider in the muon channel due to the worse p_{T} resolution than in the electron channel. No significant deviation is observed in the data from the SM background prediction. Table 11.1 and Table 11.2 show the contributions of individual backgrounds as well as the total background and the data in several m_{T} regions in the electron and muon channels, respectively. The

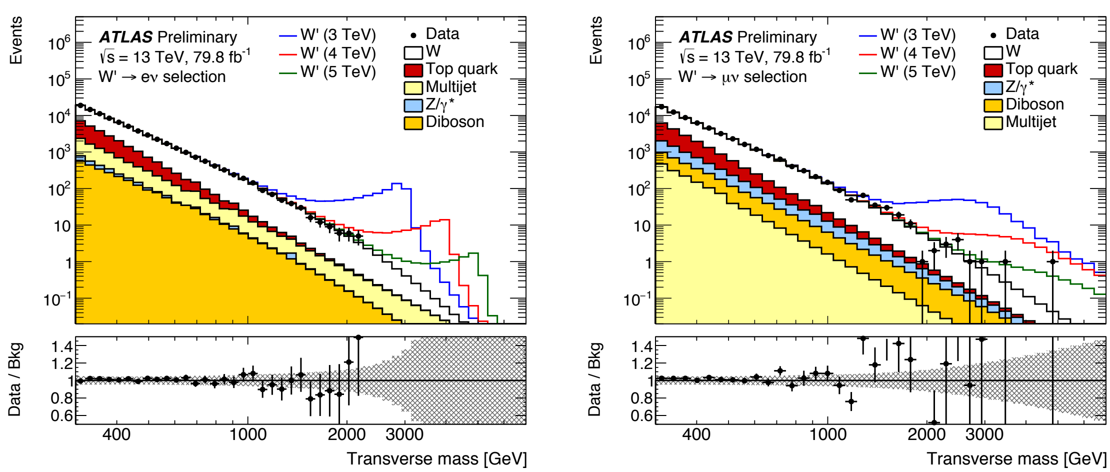

Figure 11.3. Transverse mass distributions at the signal selection in the electron (left) and muon (right) channels. As examples, the expected SSM W' signal distributions for three different masses are shown on top of the SM prediction.

expected contributions from several W' masses are also shown in each m_{T} region. The statistical analysis of the results will be discussed in the following chapter.

$W' \to e\nu$ selection						
Process	m_{T} [GeV]					
	300–400	400–600	600–1000	1000–2000	2000–3000	3000–7000
W	34947 ± 1964	14730 ± 932	3430 ± 271	424 ± 44	10.41 ± 1.53	0.62 ± 0.13
Top	12995 ± 524	3405 ± 209	353 ± 34	14 ± 5	0.11 ± 0.29	0.005 ± 0.040
Multi-jet	4243 ± 917	1337 ± 291	254 ± 60	29 ± 11	1.34 ± 1.78	0.26 ± 0.80
Diboson	1683 ± 73	677 ± 40	142 ± 14	14.9 ± 3.5	0.45 ± 0.36	0.053 ± 0.069
Z/γ^*	521 ± 108	95 ± 28	8.2 ± 8.6	1.07 ± 0.56	0.01 ± 0.00	0.00 ± 0.00
Total SM	54390 ± 2234	20244 ± 1000	4187 ± 280	483 ± 46	12.3 ± 2.4	0.94 ± 0.81
Data	54844	20519	4239	470	9	0
W' (2 TeV)	148 ± 12	418 ± 31	1291 ± 91	7146 ± 543	670 ± 192	1.83 ± 0.18
W' (3 TeV)	15.96 ± 1	34 ± 2	74 ± 5	263 ± 20	506 ± 39	50 ± 16
W' (4 TeV)	4.26 ± 0.14	7.56 ± 0.33	12.75 ± 0.74	26 ± 2	29 ± 2	50 ± 4
W' (5 TeV)	1.68 ± 0.05	2.87 ± 0.12	4.18 ± 0.22	5.68 ± 0.39	3.37 ± 0.24	8.05 ± 0.58

Table 11.1. Contributions of individual backgrounds with uncertainties for different m_{T} regions in the electron channel. The uncertainties include both statistical uncertainty and all systematics, and all weights are included so that the total background level can be compared to data.

$W' \to \mu\nu$ selection						
Process	m_{T} [GeV]					
	300–400	400–600	600–1000	1000–2000	2000–3000	3000–7000
W	26200 ± 1100	10700 ± 500	2510 ± 150	287 ± 23	8.6 ± 1.3	1.04 ± 0.28
Top	9550 ± 180	2570 ± 70	305 ± 15	19 ± 6	0.37 ± 0.30	0.04 ± 0.04
Z/γ^*	2458 ± 100	770 ± 40	132 ± 9	15.9 ± 2.2	0.51 ± 0.08	0.073 ± 0.025
Diboson	1257 ± 31	495 ± 16	101 ± 7	13 ± 5	0.6 ± 0.5	0.13 ± 0.14
Multi-jet	1080 ± 1000	310 ± 280	40 ± 40	4 ± 4	0.11 ± 0.11	0.018 ± 0.019
Total SM	40500 ± 1600	14800 ± 700	3100 ± 170	339 ± 26	10.2 ± 1.5	1.29 ± 0.32
Data	41445	15111	3129	368	12	2
W' (2 TeV)	121 ± 5	343 ± 15	960 ± 40	3900 ± 180	870 ± 70	30 ± 16
W' (3 TeV)	11.98 ± 0.34	26.01 ± 1.00	58.2 ± 2.9	185 ± 15	221 ± 19	91 ± 21
W' (4 TeV)	3.12 ± 0.06	5.50 ± 0.15	9.1 ± 0.4	18.4 ± 1.7	19.7 ± 2.5	25 ± 6
W' (5 TeV)	1.226 ± 0.022	2.02 ± 0.05	2.840 ± 0.100	3.80 ± 0.27	2.22 ± 0.34	3.8 ± 1.1

Table 11.2. Contributions of individual backgrounds with uncertainties for different m_{T} regions in the muon channel. The uncertainties include both statistical and systematic uncertainty, and all weights are included so that the total background level can be compared to data.

12. Statistical Interpretation of the Results

In this chapter, the framework for statistical analysis is introduced in Section 12.1. The statistical analysis for discovery of a new heavy boson is discussed in Section 12.2, and exclusion limits are discussed in Section 12.3.

12.1 Framework for Statistical Analysis

The search is performed using the binned m_{T} distribution, which is shown in Figure 11.3, for each of the SSM W' signals for masses from 350 GeV to 6 TeV in steps of 50 GeV. The data are interpreted using a multiple bin counting approach, which considers the event count in each transverse mass bin to extract the shape of the m_{T} distribution. This approach is also referred to as "binned shape analysis".

The parameter of interest of this analysis is the signal cross section σ. The expectation value λ_{kl} in each transverse mass bin l of decay channel k is written as the sum of the signal and background contributions:

$$\lambda_{kl}(\sigma, \boldsymbol{\theta}) = s_{kl}(\sigma, \boldsymbol{\theta}) + b_{kl}(\boldsymbol{\theta})\,, \tag{12.1}$$

where the nuisance parameters $\boldsymbol{\theta}$ describe the effect of systematic uncertainties.

The observed event count in each transverse mass bin is described using a Poisson distributed stochastic variable. Hence, the number of expected signal events in transverse mass bin of l of decay channel k is written as

$$s_{kl}(\sigma, \boldsymbol{\theta}) = \overline{s_{kl}}(\sigma)\ \exp\left(\sum_{i=1}^{N_{\mathrm{sys}}} \mathrm{sgn}[(\delta s_{kl})_i]\,\theta_i \sqrt{\ln\left[1 + \left(\frac{(\delta s_{kl})_i}{\overline{s_{kl}}}\right)^2\right]}\right) \tag{12.2}$$

with the central value

$$\overline{s_{kl}}(\sigma) = L_{\text{int}}\,\sigma\,A_k\,\varepsilon_{kl}, \tag{12.3}$$

where L_{int} is the integrated luminosity of the data, A_k is the total acceptance times efficiency for signal events in decay channel k, and ε_{kl} is the fraction of the events which go into bin l from the signal transverse mass histogram in decay channel k. The binning in the m_{T} distribution is coarse enough to ignore bin migration effects. The total acceptance times efficiency for signal A_k is discussed in Section 8.5 and plotted as a function of the W' mass for both electron and muon channels in Figure 8.5. For instance, the difference between the W' (colored lines) and the total background (black line) in the given transverse mass bin l in Figure 11.3 is the central value $\overline{s_{kl}}$ of the signal contribution of the channel k to the bin l.

The number of expected background events in transverse mass bin l of decay channel k is written as

$$b_{kl}(\boldsymbol{\theta}) = \overline{b_{kl}}\,\exp\left(\sum_{i=1}^{N_{\text{sys}}} \text{sgn}[(\delta b_{kl})_i]\,\theta_i\,\sqrt{\ln\left[1+\left(\frac{(\delta b_{kl})_i}{\overline{b_{kl}}}\right)^2\right]}\right), \tag{12.4}$$

with the central value $\overline{b_{kl}}$ is the background estimates.

The exponent terms in Equation 12.2 and Equation 12.4 reflect the effect of systematic uncertainties to the signal and background expectation values, respectively. The term $(\delta s_{kl})_i/\overline{s_{kl}}$ and $(\delta b_{kl})_i/\overline{b_{kl}}$ in each of the exponent expressions are the relative shift induced by a "one standard deviation" variation of the nuisance parameter θ_i associated with the ith systematic uncertainty. The complete list of systematic uncertainties is shown in Table 10.1 and the corresponding background distributions are shown in Figure 10.5 to Figure 10.8. Correlations of nuisance parameters between electron and muon channels and between s_{kl} and b_{kl} are properly considered. The relative shift is set to zero for nuisance parameters which affect only one of the channels or only the background.

The likelihood is then written by the product of the Poisson probabilities for each transverse mass bin l of decay channel k:

$$\mathcal{L}(\sigma, \boldsymbol{\theta}) = P(\mathbf{n}|\sigma, \boldsymbol{\theta}) = \prod_{k=1}^{N_{\text{chan}}} \prod_{l=1}^{N_{\text{bin}}} \frac{\lambda_{kl}(\sigma, \boldsymbol{\theta})^{n_{kl}} \, e^{-\lambda_{kl}(\sigma, \boldsymbol{\theta})}}{n_{kl}!} \tag{12.5}$$

where $\mathbf{n}$ denotes the set of observations n_{kl} from individual bins. The number of channels N_{chan} is equal to 1 for the electron or muon channels are analyzed separately, and 2 for the combined analysis.

12.2 Discovery Statistics

The search for a new heavy gauge boson is performed in the context of a frequentist statistical test.

12.2.1 Frequentist Probability for Discovery of a New Signal

The p-value, which represents the probability that the background fluctuation creates a signal-like excess greater or equal to the observed one, is computed using a test statistic. A test statistic q_0 for discovery of a positive signal is chosen as the test statistic of the analysis [75]. It compares the level of agreement of the observed data with background-only and signal plus background hypotheses using a profile likelihood ratio and considers only the positive signal contribution which leads an excess in addition to the background contribution. The likelihood of the background-only hypothesis and signal plus background hypotheses are built using Equation 12.5. The test statistic q_0 is then defined for $\hat{\sigma} \geqslant 0$

using the profile likelihood ratio with the background-only hypothesis in the numerator and the signal plus background hypothesis in the denominator:

$$q_0 = \begin{cases} -2\ln\left[\dfrac{\mathcal{L}(0,\hat{\boldsymbol{\theta}}_0)}{\mathcal{L}(\hat{\sigma},\hat{\boldsymbol{\theta}})}\right] & \text{for } \hat{\sigma} \geqslant 0, \\ \\ 0 & \text{for } \hat{\sigma} < 0, \end{cases} \tag{12.6}$$

where $\hat{\boldsymbol{\theta}}_0$ in the numerator are the nuisance parameter values maximizing $\mathcal{L}(0,\boldsymbol{\theta})$ and $\hat{\sigma}$ and $\hat{\boldsymbol{\theta}}$ in the denominator are the parameter values maximizing $\mathcal{L}(\sigma,\boldsymbol{\theta})$. A large excess in the data compared to the background leads to a large difference between $\mathcal{L}(0,\hat{\boldsymbol{\theta}}_0)$ and $\mathcal{L}(\hat{\sigma},\hat{\boldsymbol{\theta}})$, and hence a large corresponding q_0 value. The test statistic q_0 is set to zero for the case $\hat{\sigma} < 0$ as the signal cross section cannot be negative.

The p-value p_0 can be quantified using the observed value of q_0:

$$p_0 = P(q_0 \geqslant q_0^{\text{obs}}|\sigma = 0) = \int_{q_0^{\text{obs}}}^{\infty} f(q_0|0,\hat{\boldsymbol{\theta}}_0)\,dq_0, \tag{12.7}$$

where $f(q_0|0,\hat{\boldsymbol{\theta}}_0)$ is the probability density function of the test statistic q_0 under assumption of the background-only hypothesis. Background-only pseudo-experiments are generated to

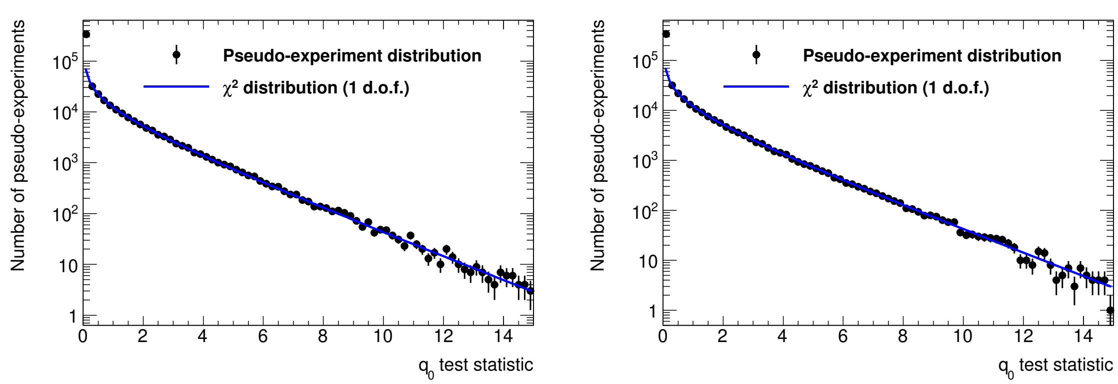

Figure 12.1. Distribution of the test statistic q_0 for background-only pseudo-experiments in the electron channel (left) and muon channel (right).

build the probability density function as shown in Figure 12.1. The peak at $q_0 = 0$ corresponds to downward fluctuations ($\hat{\sigma} < 0$) of background-only hypothesis. In the asymptotic limit, the distribution of test statistic q_0 for upward fluctuations under the background-only hypothesis follows a χ^2 distribution for one degree of freedom according to Wilks' theorem [76] as shown in Figure 12.1. Therefore, the p-value can be directly calculated from q_0 [75]:

$$p_0 = 1 - \Phi(\sqrt{q_0}) \tag{12.8}$$

where Φ is the cumulative distribution of the standard Gaussian.

The significance Z represents the number of standard deviations which correspond to an area equal to the p-value under the right-most tail of a standard normal distribution. The significance can be written as follows from the p_0 value:

$$Z = \Phi^{-1}(1 - p_0)\,, \tag{12.9}$$

and can be simplified in the asymptotic limit using Equation 12.8:

$$Z = \sqrt{q_0}\,. \tag{12.10}$$

By convention, a significance of 3σ is claimed as 'evidence' of a signal, which corresponds to a probability of background fluctuation of 1.35×10^{-3}. A significance of 5σ is claimed as 'discovery', which corresponds to a probability of background fluctuation of 2.87×10^{-7}.

The significance described above is evaluated at a given W' mass, which is called the *local significance*. The significance of observing a local excess should be compared with the probability of observing such an excess anywhere in the W' masses. This is called the *look elsewhere effect* [77]. The probability of a background fluctuation at any mass value in the range of interest is called the *global p-value*. The global significance is evaluated by generating background-only pseudo-experiments using the best-fit value of the nuisance parameters. The whole W' mass range is scanned for each pseudo-experiment, and the highest

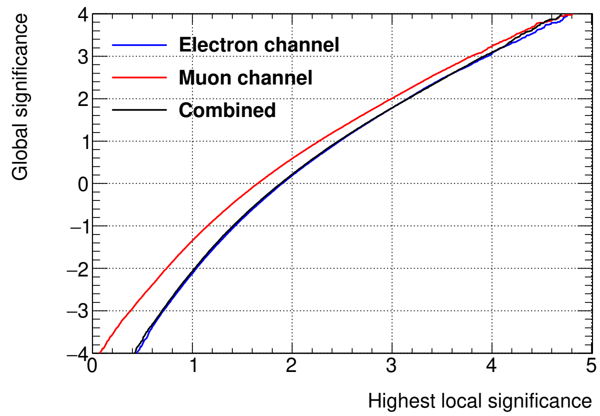

Figure 12.2. The mapping between the highest local significance and global significance for the electron channel, the muon channel, and the combined.

local significance is extracted. The global p-value for a given highest local significance is determined:

$$p_{\text{global}} = \int_Z^{\infty} f(Z)\, dZ \tag{12.11}$$

where $f(Z)$ is the probability density function given by the distribution of highest local significances in the pseudo-experiments. Figure 12.2 shows the global p-value expressed in Gaussian significance as a function of the highest local significance for the electron channel, the muon channel, and the combined channel. Negative values of global significance indicate cases which are less signal-like than expected from the background-only case. The global significance is smaller than the highest local significance. The highest local significance is on average lower in the muon channel than the electron channel at the given global significance. This is due to the better energy resolution in the electron channel, which leads to a smaller fluctuation along the transverse mass in the electron channel as shown in Figure 11.3.

12.2.2 Results

The observed local p-values for the SSM W' signals between 350 GeV and 6 TeV are shown in Figure 12.3. The results are shown for the electron channel on top left, the muon

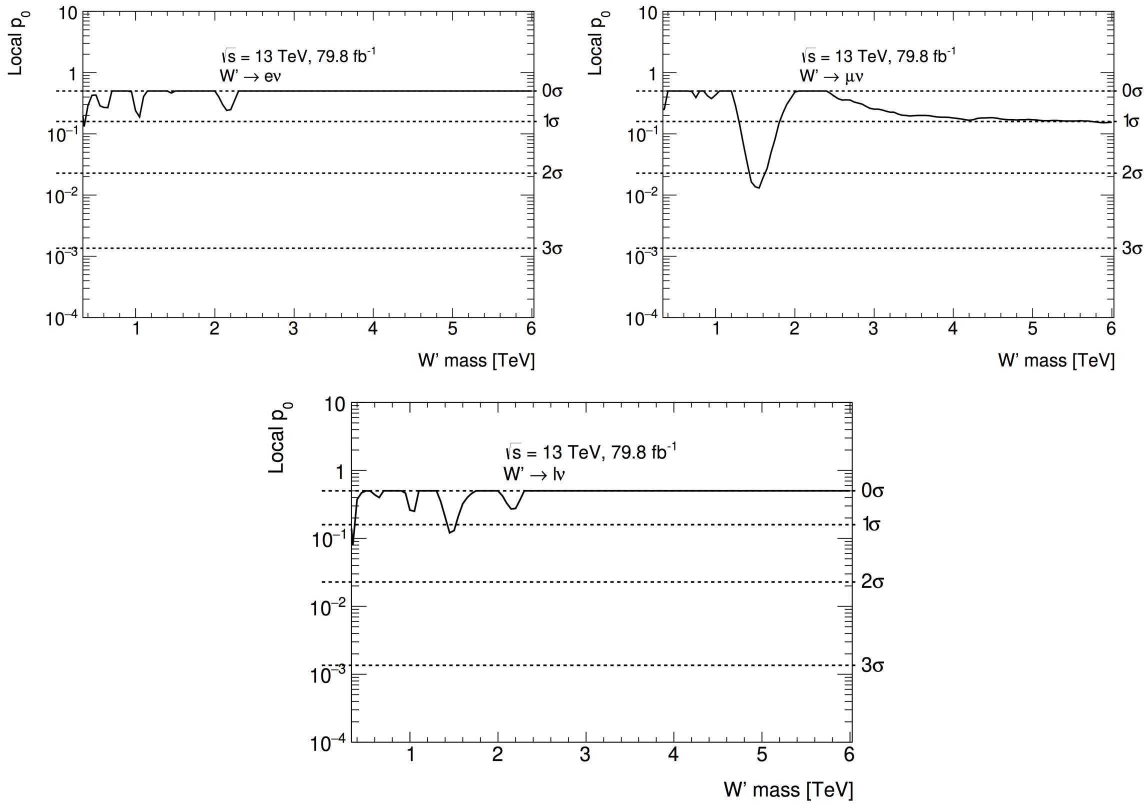

Figure 12.3. The local p-values from W'_{SSM} signals between 0.35 and 6 TeV for the electron (top left), muon (top right), and combined channel (bottom). The local significance levels are shown as dashed lines.

channel on the top right, and the combined channel on the bottom. The most significant excess in the electron channel is a local significance of 1.1σ at $m_{W'} = 350$ GeV. The excesses at $m_{W'} = 1.05$ TeV with a local significance of 0.9σ and at $m_{W'} = 2.15$ TeV with 0.7σ correspond to the two bins around 1 TeV above the background expectation and the last bin with data, respectively, as shown on the left-hand side plot of Figure 11.3. In the muon channel, the most significant excess is a local significance of 2.2σ at $m_{W'} = 1.55$ TeV, which corresponds to the few consecutive bins around 1.5 TeV as shown on the right-hand side of Figure 11.3. The broad excess in the very high W' mass region arises from the two events above 3 TeV as shown on the right-hand side of Figure 11.3. For the combination of the two channels, the most significant excess is a local significance of 1.4σ at $m_{W'} = 350$ GeV. The global significances of the highest local significances are –1.8σ in the electron channel, 0.9σ in the muon channel, and –1.0σ in the combined channel. No evidence of the W' signal is observed from the statistical tests for the electron, muon, and combined channel. Hence, the observed data are consistent with the Standard Model prediction.

12.3 Exclusion Limits

The statistical analysis for discovery shows no significant excess in the data over the expected SM backgrounds. Hence, exclusion limits are calculated for the SSM W' model.

12.3.1 Bayesian Limit on the Signal Cross Section

The exclusion limit on the signal cross section σ is calculated using the Bayesian approach. The Bayesian approach is chosen so as to compare with previous ATLAS W' searches and other experiments.

The Bayesian joint posterior probability distribution for the parameter of interest σ and nuisance parameters $\boldsymbol{\theta}$ is given by:

$$p(\sigma, \boldsymbol{\theta}|\mathbf{n}) = \frac{P(\mathbf{n}|\sigma, \boldsymbol{\theta})\, p(\sigma, \boldsymbol{\theta})}{P(\mathbf{n})} = \frac{\mathcal{L}(\sigma, \boldsymbol{\theta})\, p(\sigma, \boldsymbol{\theta})}{P(\mathbf{n})}\,, \tag{12.12}$$

where $P(\mathbf{n}|\sigma, \boldsymbol{\theta})$ is the likelihood as defined in Equation 12.5, $P(\mathbf{n})$ is the probability for the observed data , and $p(\sigma, \boldsymbol{\theta})$ is the prior probability density for σ and $\boldsymbol{\theta}$. The nuisance parameters are assumed to follow a Gaussian distribution. Hence, the prior can be written as:

$$p(\sigma, \boldsymbol{\theta}) = p(\sigma) \prod_{i=1}^{N_{\text{sys}}} \phi(\theta_i)\,, \tag{12.13}$$

where ϕ is the probability density function for the standard normal distribution and $p(\sigma)$ is the prior distribution for the signal cross section. The prior distribution for the signal cross section is taken to be flat, i.e. zero for $\sigma < 0$ and constant for $\sigma \geq 0$. Although a choice of the prior distribution for the signal cross section based on the knowledge from previous

W' searches would strengthen the limits, a conservative flat prior distribution is chosen to make the results comparable with previous W' searches.

The marginalization integral is performed over the nuisance parameters using Markov Chain MC sampling in the Bayesian Analysis Toolkit [78] to get the posterior only for the signal cross section. The posterior for the signal cross section is then written as:

$$p(\sigma|\mathbf{n}) = \int p(\sigma, \boldsymbol{\theta}|\mathbf{n})\, d\boldsymbol{\theta} = N \int \prod_{k=1}^{N_{\mathrm{chan}}} \prod_{l=1}^{N_{\mathrm{bin}}} \frac{\lambda_{kl}(\sigma, \boldsymbol{\theta})^{n_{kl}}\, e^{-\lambda_{kl}(\sigma,\boldsymbol{\theta})}}{n_{kl}!} \prod_{i=1}^{N_{\mathrm{sys}}} \phi(\theta_i)\, d\boldsymbol{\theta} \tag{12.14}$$

for $\sigma \geq 0$. The normalization constant N is determined by condition:

$$\int_0^\infty p(\sigma|\mathbf{n})\, d\sigma = 1\,. \tag{12.15}$$

The contant prior for the signal cross section is also absorbed into the normalization constant. Thus, the upper limit σ_{up} on the cross section at credibility level (CL) $1 - \delta$ is calculated from:

$$\int_{\sigma_{\mathrm{up}}}^\infty p(\sigma|\mathbf{n})\, d\sigma = \delta\,. \tag{12.16}$$

Exclusion at 95% CL is chosen as is customary in high energy physics.

The limit from the procedure described above is called the *observed limit* as it is calculated using the observed data. Additionally, the limit is calculated using the background-only hypothesis, which is called the *expected limit*. The expected limit utilizes a sample of background-only pseudo-experiments to calculate the cross section limit. The median of the limit distribution is taken as the expected limit, and the 68% and 95% quantiles as the $\pm 1\sigma$ and $\pm 2\sigma$ bands, respectively. The expected limit is a measure of the sensitivity of the experiment, and a large deviation of the observed limit from the expected limit indicates that the experiment or the background are not understood well or is a signatures of new physics.

12.3.2 Results

Figure 12.4 shows the upper limits on the cross section times branching ratio for $W' \to e\nu$ (top left), $W' \to \mu\nu$ (top right), and $W' \to \ell\nu$ (bottom) productions at 95% CL. The expected limits are shown in the black dashed lines with the $\pm 1\sigma$ and $\pm 2\sigma$ bands in green and yellow, respectively. The expected limits are falling steeply from low W' masses up to about 3.5 TeV and then increase towards the highest masses. This behavior is closely related to the total W' signal acceptance times efficiency as shown in Figure 8.5. A significantly lower signal-to-background ratio for lower W' masses, which originates from the much higher background levels and the worse W' signal acceptance times efficiency, leads an increased limit in the low W' mass region. The increase at the highest masses is due to low mass off-shell productions as discussed in Section 8.5. The limit is stronger in the electron channel than muon channel due to the larger W' signal efficiency and the better momentum resolution. The combined result is also driven by the electron channel.

The observed limits are shown in the solid black lines. The observed limits agree reasonably well with the expected limit and mostly lie within the $\pm 2\sigma$ bands. Slight excesses with respect to the expected limits correspond to the masses with relatively higher significances which are discussed in Section 12.2.2. The deficit in the electron channel for W' masses higher than 3 TeV could originate from a lack of very high m_{T} events in the electron channel or a slight overestimation of backgrounds, especially those backgrounds using a high-m_{T} extrapolation.

The predicted cross section time branching ratio for SSM W' productions is shown as red solid lines. The red-dashed lines represent the corresponding uncertainties from the theory as discussed in Section 10.2. Masses for the SSM W' boson above the intersection between observed limit and theory prediction are excluded with 95% CL. The observed and expected lower mass limits for the SSM W' are summarized in Table 12.1. The observed lower mass limit in the electron channel is 5.7 TeV and the expected lower mass limit is 5.4 TeV. The stronger lower mass limit is caused by a deficit in the very high m_{T} region as discussed before. The observed lower mass limit in the muon channel is 4.8 TeV and

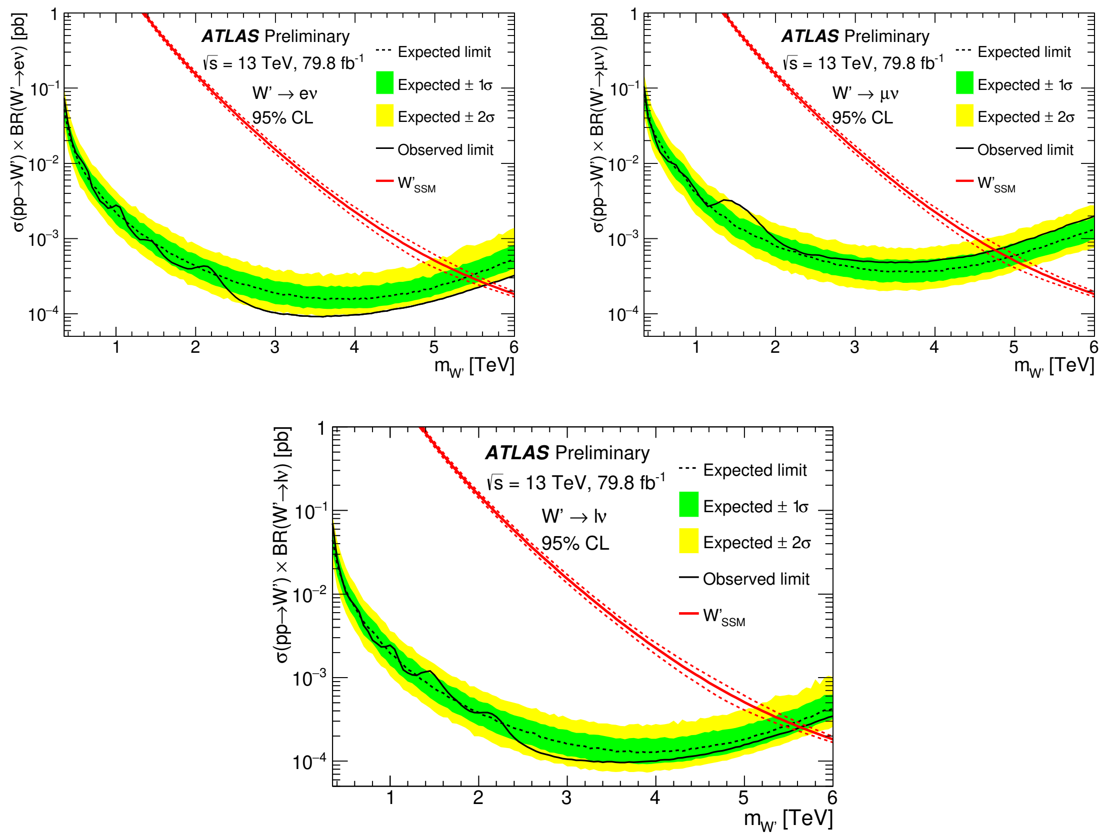

Figure 12.4. W' cross section limit results for the electron channel (top), the muon channel (middle) and combined (bottom).

the expected lower mass limit is 4.9 TeV. The lower mass limits are stronger in the electron channel for the same reason as the stronger limit on the signal cross section times branching

	$m_{W'}$ lower limit [TeV]	
Decay	Expected	Observed
$W' \to e\nu$	5.4	5.7
$W' \to \mu\nu$	4.9	4.8
$W' \to \ell\nu$	5.5	5.6

Table 12.1. Expected and observed 95% CL lower limit on the SSM W' mass in the electron and muon channels and their combination.

ratio. The observed lower mass limit in the combined channel is 5.6 TeV and the expected lower mass limit is 5.5 TeV.

12.3.3 Comparison to the Previous Searches

The exclusion limits on the SSM W' mass are compared with the previous W' searches for lepton channels at the Tevatron and LHC experiments as shown in Table 12.2. The limit was set to 1.00 TeV from the D0 experiment in 2008. The most stringent limit is set to 5.6 TeV in 2018 from the analysis of this thesis. The limit is drastically improved with the significantly higher center-of-mass energy and luminosity in the LHC.

Comparison of the results from the ATLAS and CMS experiments for a similar integrated luminosity shows stronger limits in the electron channel and weaker limits in the muon channel for the result from the ATLAS experiment. These differences originate from the differences in the acceptance times efficiency between two experiments, which reflect differences in the performance. The primary source is the lower muon trigger efficiency in the ATLAS (about 70 – 80%) compared to the CMS (above 90%) due to the stringent quality requirements on the high-p_{T} muons.

			$m_{W'}$ lower limit [TeV]		
Experiment	$\sqrt{s}$ [TeV]	$L_{\mathrm{int}}[\mathrm{fb}^{-1}]$	$W' \to e\nu$	$W' \to \mu\nu$	$W' \to \ell\nu$
D0 [79]	1.96	0.99	1.00	-	-
CDF [80]	1.96	5.3	1.12	-	-
ATLAS [81]	13	3.2	3.96	3.56	4.07
CMS [82]	13	2.3	3.8	4.0	4.4
ATLAS [83]	13	36.1	5.2	4.5	5.1
CMS [84]	13	35.9	4.9	4.9	5.2
ATLAS [85]	13	79.8	5.7	4.8	5.6

Table 12.2. Observed 95% CL lower limits on the SSM W' mass from previous and other searches. The last row is the result of this analysis.

13. Conclusion and Outlook

A search for a new heavy gauge boson in final states with one electron or one muon and missing transverse momentum has been presented. The dataset recorded in 2015−2017 by the ATLAS detector from proton-proton collisions at a center-of-mass energy of 13 TeV is analyzed, which amounts to an integrated luminosity of 79.8 fb^{-1}. No evidence of an excess over the SM expectations is observed. Hence, an upper limit on the production cross section times branching ratio, $\sigma(pp \to W') \times BR(W' \to \ell\nu)$, has been derived following the Bayesian approach. The excluded cross section reaches below 0.1 fb in the electron channel at $m_{W'}$ around 3.5 TeV, 0.5 fb in the muon channel at $m_{W'}$ around 3.4 TeV. The excluded cross section in the combination of electron and muon channels is driven by the electron channel. These results are interpreted in the context of the Sequential Standard Model W', and masses below 5.7 TeV and 4.8 TeV are excluded with 95% CL in the electron and muon channels, respectively. The combined exclusion limit is set to 5.6 TeV.

Even though no evidence of a new heavy gauge boson is observed from the analysis of this thesis, the analysis with the full Run-2 dataset is already underway to find possible clues of new physics. In the longer term, the HL-LHC (High Luminosity LHC) is foreseen with an expected integrated luminosity of 3000 fb^{-1}, which could lead an exclusion of the W' mass up to 7.9 TeV or a discovery of a new heavy gauge boson up to the SSM W' mass of 7.7 TeV based on a 5σ significance.

APPENDICES

A. Monte Carlo Background Samples

This chapter provides detail information on the Monte Carlo samples.

Run	Process	N_{evt} [k]	σB [pb]	K-factor	L_{int} [fb^{-1}]
		Diboson			
364250	$ZZ \to \ell\ell\ell\ell$	17842(a) / 35995(d)	1.3e+00	–	1.4e+04(a) / 2.8e+04(d)
364253	$WZ \to \ell\ell\ell\nu$	15537(a) / 32113(d)	4.6e+00	–	3.4e+03(a) / 7.0e+03(d)
364254	$VV \to \ell\ell\nu\nu$	14996(a) / 29975(d)	1.3e+01	–	1.2e+03(a) / 2.3e+03(d)
364255	$WZ \to \ell\nu\nu\nu$	5999(a) / 11995(d)	3.2e+00	–	1.9e+03(a) / 3.7e+03(d)
363360	$W^+W^- \to \ell\nu qq$	7188(a) / 14372(d)	2.5e+01	–	2.9e+02(a) / 5.7e+02(d)
363359	$W^+W^- \to qq\ell\nu$	7194(a) / 28711(d)	2.5e+01	–	2.9e+02(a) / 1.1e+03(d)
363489	$WZ \to \ell\nu qq$	7180(a) / 7200(d)	1.1e+01	–	6.5e+02(a) / 6.5e+02(d)
363358	$WZ \to qq\ell\ell$	5400(a) / 21532(d)	3.4e+00	–	1.6e+03(a) / 6.3e+03(d)
363356	$ZZ \to qq\ell\ell$	5400(a) / 5400(d)	2.2e+00	–	2.5e+03(a) / 2.5e+03(d)
		Top			
410470	$t\bar{t} \to \ell X$	59998(a) / 74486(d)	4.0e+02	1.14	1.5e+02(a) / 1.9e+02(d)
410642	t-channel $t \to \ell X$	4994(a) / 6238(d)	3.7e+01	–	1.3e+02(a) / 1.7e+02(d)
410643	t-channel $\bar{t} \to \ell X$	4975(a) / 6250(d)	2.2e+01	–	2.3e+02(a) / 2.8e+02(d)
410013	s-channel Wt	5000(a) / 5000(d)	3.4e+01	1.054	1.5e+02(a) / 1.5e+02(d)
410014	s-channel $W\bar{t}$	4968(a) / 4998(d)	3.4e+01	1.054	1.5e+02(a) / 1.5e+02(d)

Table A.1. Monte Carlo samples for backgrounds that contribute to both the electron and muon channels. For each dataset, the following is listed: the ATLAS Monte Carlo dataset ID, the physics process (including the mass range in GeV when appropriate), the number of generated events, the cross section times branching ratio, K-factor, and the equivalent integrated luminosity $L_{\mathrm{int}} = N_{\mathrm{evt}}/(\sigma B)$. Letters in the parentheses represent Monte Carlo samples with the 2015+2016 dataset pile-up profile with (a) and the 2017 dataset pile-up profile with (d).

Dataset ID	Process	N_{evt} [k]	σB [pb]	K-factor	L_{int} [fb^{-1}]
Inclusive and mass binned $W^+ \to e\nu$					
361100	$W^+ \to e\nu$	41415(a) / 40918(d)	1.1e+04	$K(m)$	3.8e+00(a) / 3.7e+00(d)
301060	$W^+(120, 180) \to e\nu$	500(a) / 500(d)	3.2e+01	$K(m)$	1.6e+01(a) / 1.6e+01(d)
301061	$W^+(180, 250) \to e\nu$	250(a) / 250(d)	5.0e+00	$K(m)$	5.0e+01(a) / 5.0e+01(d)
301062	$W^+(250, 400) \to e\nu$	140(a) / 135(d)	1.8e+00	$K(m)$	7.8e+01(a) / 7.5e+01(d)
301063	$W^+(400, 600) \to e\nu$	100(a) / 100(d)	3.1e−01	$K(m)$	3.2e+02(a) / 3.2e+02(d)
301064	$W^+(600, 800) \to e\nu$	50(a) / 50(d)	6.1e−02	$K(m)$	8.2e+02(a) / 8.2e+02(d)
301065	$W^+(800, 1000) \to e\nu$	50(a) / 50(d)	1.8e−02	$K(m)$	2.8e+03(a) / 2.8e+03(d)
301066	$W^+(1000, 1250) \to e\nu$	50(a) / 45(d)	7.3e−03	$K(m)$	6.8e+03(a) / 6.2e+03(d)
301067	$W^+(1250, 1500) \to e\nu$	50(a) / 50(d)	2.5e−03	$K(m)$	2.0e+04(a) / 2.0e+04(d)
301068	$W^+(1500, 1750) \to e\nu$	50(a) / 50(d)	9.9e−04	$K(m)$	5.1e+04(a) / 5.1e+04(d)
301069	$W^+(1750, 2000) \to e\nu$	40(a) / 40(d)	4.2e−04	$K(m)$	9.5e+04(a) / 9.5e+04(d)
301070	$W^+(2000, 2250) \to e\nu$	47(a) / 50(d)	1.9e−04	$K(m)$	2.5e+05(a) / 2.6e+05(d)
301071	$W^+(2250, 2500) \to e\nu$	50(a) / 50(d)	9.3e−05	$K(m)$	5.4e+05(a) / 5.4e+05(d)
301072	$W^+(2500, 2750) \to e\nu$	50(a) / 50(d)	4.6e−05	$K(m)$	1.1e+06(a) / 1.1e+06(d)
301073	$W^+(2750, 3000) \to e\nu$	50(a) / 50(d)	2.3e−05	$K(m)$	2.2e+06(a) / 2.2e+06(d)
301074	$W^+(3000, 3500) \to e\nu$	50(a) / 50(d)	1.8e−05	$K(m)$	2.8e+06(a) / 2.8e+06(d)
301075	$W^+(3500, 4000) \to e\nu$	50(a) / 50(d)	5.1e−06	$K(m)$	9.8e+06(a) / 9.8e+06(d)
301076	$W^+(4000, 4500) \to e\nu$	50(a) / 50(d)	1.4e−06	$K(m)$	3.6e+07(a) / 3.6e+07(d)
301077	$W^+(4500, 5000) \to e\nu$	50(a) / 45(d)	4.0e−07	$K(m)$	1.3e+08(a) / 1.1e+08(d)
301078	$W^+(> 5000) \to e\nu$	50(a) / 50(d)	1.5e−07	$K(m)$	3.3e+08(a) / 3.3e+08(d)

Table A.2. Monte Carlo samples for backgrounds that contribute to the electron channel. For each dataset, the following is listed: the ATLAS Monte Carlo dataset ID, the physics process (including the mass range in GeV when appropriate), the number of generated events, the cross section times branching ratio, K-factor ($K(m)$ denotes a mass dependent K-factor is used), and the equivalent integrated luminosity $L_{\text{int}} = N_{\text{evt}}/(\sigma B)$. Letters in the parentheses represent Monte Carlo samples with the 2015+2016 dataset pile-up profile with (a) and the 2017 dataset pile-up profile with (d).

Dataset ID	Process	N_{evt} [k]	σB [pb]	K-factor	L_{int} [fb^{-1}]
		Inclusive and mass binned $W^- \to e\nu$			
361103	$W^- \to e\nu$	49904(a) / 49961(d)	8.3e+03	$K(m)$	6.0e+00(a) / 6.0e+00(d)
301080	$W^-(120, 180) \to e\nu$	500(a) / 500(d)	2.2e+01	$K(m)$	2.3e+01(a) / 2.3e+01(d)
301081	$W^-(180, 250) \to e\nu$	250(a) / 250(d)	3.3e+00	$K(m)$	7.6e+01(a) / 7.6e+01(d)
301082	$W^-(250, 400) \to e\nu$	150(a) / 150(d)	1.1e+00	$K(m)$	1.4e+02(a) / 1.4e+02(d)
301083	$W^-(400, 600) \to e\nu$	100(a) / 100(d)	1.8e−01	$K(m)$	5.6e+02(a) / 5.6e+02(d)
301084	$W^-(600, 800) \to e\nu$	50(a) / 50(d)	3.1e−02	$K(m)$	1.6e+03(a) / 1.6e+03(d)
301085	$W^-(800, 1000) \to e\nu$	50(a) / 50(d)	8.3e−03	$K(m)$	6.0e+03(a) / 6.0e+03(d)
301086	$W^-(1000, 1250) \to e\nu$	50(a) / 50(d)	3.2e−03	$K(m)$	1.6e+04(a) / 1.6e+04(d)
301087	$W^-(1250, 1500) \to e\nu$	50(a) / 50(d)	1.0e−03	$K(m)$	5.0e+04(a) / 5.0e+04(d)
301088	$W^-(1500, 1750) \to e\nu$	50(a) / 50(d)	3.7e−04	$K(m)$	1.4e+05(a) / 1.4e+05(d)
301089	$W^-(1750, 2000) \to e\nu$	50(a) / 50(d)	1.5e−04	$K(m)$	3.3e+05(a) / 3.3e+05(d)
301090	$W^-(2000, 2250) \to e\nu$	50(a) / 50(d)	6.5e−05	$K(m)$	7.7e+05(a) / 7.7e+05(d)
301091	$W^-(2250, 2500) \to e\nu$	50(a) / 50(d)	3.0e−05	$K(m)$	1.7e+06(a) / 1.7e+06(d)
301092	$W^-(2500, 2750) \to e\nu$	50(a) / 50(d)	1.5e−05	$K(m)$	3.3e+06(a) / 3.3e+06(d)
301093	$W^-(2750, 3000) \to e\nu$	50(a) / 50(d)	7.3e−06	$K(m)$	6.8e+06(a) / 6.8e+06(d)
301094	$W^-(3000, 3500) \to e\nu$	50(a) / 50(d)	5.7e−06	$K(m)$	8.8e+06(a) / 8.8e+06(d)
301095	$W^-(3500, 4000) \to e\nu$	50(a) / 50(d)	1.6e−06	$K(m)$	3.1e+07(a) / 3.1e+07(d)
301096	$W^-(4000, 4500) \to e\nu$	50(a) / 50(d)	4.7e−07	$K(m)$	1.1e+08(a) / 1.1e+08(d)
301097	$W^-(4500, 5000) \to e\nu$	50(a) / 50(d)	1.4e−07	$K(m)$	3.6e+08(a) / 3.6e+08(d)
301098	$W^-(> 5000) \to e\nu$	50(a) / 50(d)	6.2e−08	$K(m)$	8.1e+08(a) / 8.1e+08(d)

Table A.3. Monte Carlo samples for backgrounds that contribute to the electron channel. For each dataset, the following is listed: the ATLAS Monte Carlo dataset ID, the physics process (including the mass range in GeV when appropriate), the number of generated events, the cross section times branching ratio, K-factor ($K(m)$ denotes a mass dependent K-factor is used), and the equivalent integrated luminosity $L_{\text{int}} = N_{\text{evt}}/(\sigma B)$. Letters in the parentheses represent Monte Carlo samples with the 2015+2016 dataset pile-up profile with (a) and the 2017 dataset pile-up profile with (d).

Dataset ID	Process	N_{evt} [k]	σB [pb]	K-factor	L_{int} [fb^{-1}]
		Inclusive and mass binned $W^+ \to \mu\nu$			
361101	$W^+ \to \mu\nu$	39962(a) / 39952(d)	1.1e+04	$K(m)$	3.6e+00(a) / 3.6e+00(d)
301100	$W^+(120, 180) \to \mu\nu$	500(a) / 500(d)	3.2e+01	$K(m)$	1.6e+01(a) / 1.6e+01(d)
301101	$W^+(180, 250) \to \mu\nu$	250(a) / 250(d)	5.0e+00	$K(m)$	5.0e+01(a) / 5.0e+01(d)
301102	$W^+(250, 400) \to \mu\nu$	150(a) / 150(d)	1.8e+00	$K(m)$	8.3e+01(a) / 8.3e+01(d)
301103	$W^+(400, 600) \to \mu\nu$	100(a) / 100(d)	3.1e−01	$K(m)$	3.2e+02(a) / 3.2e+02(d)
301104	$W^+(600, 800) \to \mu\nu$	50(a) / 50(d)	6.1e−02	$K(m)$	8.2e+02(a) / 8.2e+02(d)
301105	$W^+(800, 1000) \to \mu\nu$	50(a) / 50(d)	1.8e−02	$K(m)$	2.8e+03(a) / 2.8e+03(d)
301106	$W^+(1000, 1250) \to \mu\nu$	50(a) / 50(d)	7.3e−03	$K(m)$	6.8e+03(a) / 6.8e+03(d)
301107	$W^+(1250, 1500) \to \mu\nu$	50(a) / 50(d)	2.5e−03	$K(m)$	2.0e+04(a) / 2.0e+04(d)
301108	$W^+(1500, 1750) \to \mu\nu$	50(a) / 50(d)	9.9e−04	$K(m)$	5.1e+04(a) / 5.1e+04(d)
301109	$W^+(1750, 2000) \to \mu\nu$	50(a) / 50(d)	4.2e−04	$K(m)$	1.2e+05(a) / 1.2e+05(d)
301110	$W^+(2000, 2250) \to \mu\nu$	50(a) / 50(d)	1.9e−04	$K(m)$	2.6e+05(a) / 2.6e+05(d)
301111	$W^+(2250, 2500) \to \mu\nu$	50(a) / 50(d)	9.3e−05	$K(m)$	5.4e+05(a) / 5.4e+05(d)
301112	$W^+(2500, 2750) \to \mu\nu$	50(a) / 50(d)	4.6e−05	$K(m)$	1.1e+06(a) / 1.1e+06(d)
301113	$W^+(2750, 3000) \to \mu\nu$	50(a) / 50(d)	2.3e−05	$K(m)$	2.2e+06(a) / 2.2e+06(d)
301114	$W^+(3000, 3500) \to \mu\nu$	50(a) / 50(d)	1.8e−05	$K(m)$	2.8e+06(a) / 2.8e+06(d)
301115	$W^+(3500, 4000) \to \mu\nu$	50(a) / 50(d)	5.1e−06	$K(m)$	9.8e+06(a) / 9.8e+06(d)
301116	$W^+(4000, 4500) \to \mu\nu$	50(a) / 50(d)	1.4e−06	$K(m)$	3.6e+07(a) / 3.6e+07(d)
301117	$W^+(4500, 5000) \to \mu\nu$	50(a) / 50(d)	4.0e−07	$K(m)$	1.3e+08(a) / 1.3e+08(d)
301118	$W^+(> 5000) \to \mu\nu$	50(a) / 50(d)	1.5e−07	$K(m)$	3.3e+08(a) / 3.3e+08(d)

Table A.4. Monte Carlo samples for backgrounds that contribute to the muon channel. For each dataset, the following is listed: the ATLAS Monte Carlo dataset ID, the physics process (including the mass range in GeV when appropriate), the number of generated events, the cross section times branching ratio, K-factor ($K(m)$ denotes a mass dependent K-factor is used), and the equivalent integrated luminosity $L_{\text{int}} = N_{\text{evt}}/(\sigma B)$. Letters in the parentheses represent Monte Carlo samples with the 2015+2016 dataset pile-up profile with (a) and the 2017 dataset pile-up profile with (d).

Dataset ID	Process	N_{evt} [k]	σB [pb]	K-factor	L_{int} [fb^{-1}]
		Inclusive and mass binned $W^- \to \mu\nu$			
361104	$W^- \to \mu\nu$	31973(a) / 31978(d)	8.3e+03	$K(m)$	3.9e+00(a) / 3.9e+00(d)
301120	$W^-(120, 180) \to \mu\nu$	500(a) / 500(d)	2.2e+01	$K(m)$	2.3e+01(a) / 2.3e+01(d)
301121	$W^-(180, 250) \to \mu\nu$	250(a) / 250(d)	3.3e+00	$K(m)$	7.6e+01(a) / 7.6e+01(d)
301122	$W^-(250, 400) \to \mu\nu$	150(a) / 150(d)	1.1e+00	$K(m)$	1.4e+02(a) / 1.4e+02(d)
301123	$W^-(400, 600) \to \mu\nu$	100(a) / 100(d)	1.8e−01	$K(m)$	5.6e+02(a) / 5.6e+02(d)
301124	$W^-(600, 800) \to \mu\nu$	50(a) / 50(d)	3.1e−02	$K(m)$	1.6e+03(a) / 1.6e+03(d)
301125	$W^-(800, 1000) \to \mu\nu$	50(a) / 50(d)	8.3e−03	$K(m)$	6.0e+03(a) / 6.0e+03(d)
301126	$W^-(1000, 1250) \to \mu\nu$	50(a) / 50(d)	3.2e−03	$K(m)$	1.6e+04(a) / 1.6e+04(d)
301127	$W^-(1250, 1500) \to \mu\nu$	50(a) / 50(d)	1.0e−03	$K(m)$	5.0e+04(a) / 5.0e+04(d)
301128	$W^-(1500, 1750) \to \mu\nu$	50(a) / 50(d)	3.7e−04	$K(m)$	1.4e+05(a) / 1.4e+05(d)
301129	$W^-(1750, 2000) \to \mu\nu$	50(a) / 50(d)	1.5e−04	$K(m)$	3.3e+05(a) / 3.3e+05(d)
301130	$W^-(2000, 2250) \to \mu\nu$	50(a) / 50(d)	6.5e−05	$K(m)$	7.7e+05(a) / 7.7e+05(d)
301131	$W^-(2250, 2500) \to \mu\nu$	50(a) / 50(d)	3.0e−05	$K(m)$	1.7e+06(a) / 1.7e+06(d)
301132	$W^-(2500, 2750) \to \mu\nu$	50(a) / 50(d)	1.5e−05	$K(m)$	3.3e+06(a) / 3.3e+06(d)
301133	$W^-(2750, 3000) \to \mu\nu$	50(a) / 50(d)	7.3e−06	$K(m)$	6.8e+06(a) / 6.8e+06(d)
301134	$W^-(3000, 3500) \to \mu\nu$	50(a) / 50(d)	5.7e−06	$K(m)$	8.8e+06(a) / 8.8e+06(d)
301135	$W^-(3500, 4000) \to \mu\nu$	50(a) / 50(d)	1.6e−06	$K(m)$	3.1e+07(a) / 3.1e+07(d)
301136	$W^-(4000, 4500) \to \mu\nu$	50(a) / 50(d)	4.7e−07	$K(m)$	1.1e+08(a) / 1.1e+08(d)
301137	$W^-(4500, 5000) \to \mu\nu$	50(a) / 50(d)	1.4e−07	$K(m)$	3.6e+08(a) / 3.6e+08(d)
301138	$W^-(> 5000) \to \mu\nu$	50(a) / 50(d)	6.2e−08	$K(m)$	8.1e+08(a) / 8.1e+08(d)

Table A.5. Monte Carlo samples for backgrounds that contribute to the muon channel. For each dataset, the following is listed: the ATLAS Monte Carlo dataset ID, the physics process (including the mass range in GeV when appropriate), the number of generated events, the cross section times branching ratio, K-factor ($K(m)$ denotes a mass dependent K-factor is used), and the equivalent integrated luminosity $L_{\text{int}} = N_{\text{evt}}/(\sigma B)$. Letters in the parentheses represent Monte Carlo samples with the 2015+2016 dataset pile-up profile with (a) and the 2017 dataset pile-up profile with (d).

Dataset ID	Process	N_{evt} [k]	σB [pb]	K-factor	L_{int} [fb^{-1}]
		Inclusive and mass binned $W^+ \to \tau\nu$			
361102	$W^+ \to \tau\nu$	29982(a) / 29959(d)	1.1e+04	$K(m)$	2.7e+00(a) / 2.7e+00(d)
301140	$W^+(120, 180) \to \tau\nu$	500(a) / 500(d)	3.2e+00	$K(m)$	1.6e+01(a) / 1.6e+01(d)
301141	$W^+(180, 250) \to \tau\nu$	250(a) / 250(d)	5.0e+00	$K(m)$	5.0e+01(a) / 5.0e+01(d)
301142	$W^+(250, 400) \to \tau\nu$	150(a) / 150(d)	1.8e+00	$K(m)$	8.3e+01(a) / 8.3e+01(d)
301143	$W^+(400, 600) \to \tau\nu$	100(a) / 100(d)	3.1e−01	$K(m)$	3.2e+02(a) / 3.2e+02(d)
301144	$W^+(600, 800) \to \tau\nu$	50(a) / 50(d)	6.1e−02	$K(m)$	8.2e+02(a) / 8.2e+02(d)
301145	$W^+(800, 1000) \to \tau\nu$	50(a) / 50(d)	1.8e−02	$K(m)$	2.8e+03(a) / 2.8e+03(d)
301146	$W^+(1000, 1250) \to \tau\nu$	50(a) / 50(d)	7.3e−03	$K(m)$	6.8e+03(a) / 6.8e+03(d)
301147	$W^+(1250, 1500) \to \tau\nu$	50(a) / 50(d)	2.5e−03	$K(m)$	2.0e+04(a) / 2.0e+04(d)
301148	$W^+(1500, 1750) \to \tau\nu$	50(a) / 50(d)	9.9e−04	$K(m)$	5.1e+04(a) / 5.1e+04(d)
301149	$W^+(1750, 2000) \to \tau\nu$	50(a) / 50(d)	4.2e−04	$K(m)$	1.2e+05(a) / 1.2e+05(d)
301150	$W^+(2000, 2250) \to \tau\nu$	50(a) / 50(d)	1.9e−04	$K(m)$	2.6e+05(a) / 2.6e+05(d)
301151	$W^+(2250, 2500) \to \tau\nu$	50(a) / 50(d)	9.3e−05	$K(m)$	5.4e+05(a) / 5.4e+05(d)
301152	$W^+(2500, 2750) \to \tau\nu$	50(a) / 50(d)	4.6e−05	$K(m)$	1.1e+06(a) / 1.1e+06(d)
301153	$W^+(2750, 3000) \to \tau\nu$	50(a) / 50(d)	2.3e−05	$K(m)$	2.2e+06(a) / 2.2e+06(d)
301154	$W^+(3000, 3500) \to \tau\nu$	50(a) / 50(d)	1.8e−05	$K(m)$	2.8e+06(a) / 2.8e+06(d)
301155	$W^+(3500, 4000) \to \tau\nu$	50(a) / 50(d)	5.1e−06	$K(m)$	9.8e+06(a) / 9.8e+06(d)
301156	$W^+(4000, 4500) \to \tau\nu$	50(a) / 50(d)	1.4e−06	$K(m)$	3.6e+07(a) / 3.6e+07(d)
301157	$W^+(4500, 5000) \to \tau\nu$	50(a) / 47(d)	4.0e−07	$K(m)$	1.3e+08(a) / 1.2e+08(d)
301158	$W^+(> 5000) \to \tau\nu$	50(a) / 50(d)	1.5e−07	$K(m)$	3.3e+08(a) / 3.3e+08(d)

Table A.6. Monte Carlo samples for backgrounds that contribute to both the electron and muon channels. For each dataset, the following is listed: the ATLAS Monte Carlo dataset ID, the physics process (including the mass range in GeV when appropriate), the number of generated events, the cross section times branching ratio, K-factor ($K(m)$ denotes a mass dependent K-factor is used, see appendix), and the equivalent integrated luminosity $L_{\text{int}} = N_{\text{evt}}/(\sigma B)$. Letters in the parentheses represent Monte Carlo samples with the 2015+2016 dataset pile-up profile with (a) and the 2017 dataset pile-up profile with (d).

Dataset ID	Process	N_{evt} [k]	σB [pb]	K-factor	L_{int} [fb^{-1}]
		Inclusive and mass binned $W^- \to \tau\nu$			
361105	$W^- \to \tau\nu$	19955(a) / 19970(d)	8.3e+03	$K(m)$	2.4e+00(a) / 2.4e+00(d)
301160	$W^-(120, 180) \to \tau\nu$	470(a) / 500(d)	2.2e+01	$K(m)$	2.1e+01(a) / 2.3e+01(d)
301161	$W^-(180, 250) \to \tau\nu$	250(a) / 250(d)	3.3e+00	$K(m)$	7.6e+01(a) / 7.6e+01(d)
301162	$W^-(250, 400) \to \tau\nu$	150(a) / 150(d)	1.1e+00	$K(m)$	1.4e+02(a) / 1.4e+02(d)
301163	$W^-(400, 600) \to \tau\nu$	100(a) / 100(d)	1.8e−01	$K(m)$	5.6e+02(a) / 5.6e+02(d)
301164	$W^-(600, 800) \to \tau\nu$	50(a) / 50(d)	3.1e−02	$K(m)$	1.6e+03(a) / 1.6e+03(d)
301165	$W^-(800, 1000) \to \tau\nu$	50(a) / 50(d)	8.3e−03	$K(m)$	6.0e+03(a) / 6.0e+03(d)
301166	$W^-(1000, 1250) \to \tau\nu$	46(a) / 50(d)	3.2e−03	$K(m)$	1.4e+04(a) / 1.6e+04(d)
301167	$W^-(1250, 1500) \to \tau\nu$	50(a) / 50(d)	1.0e−03	$K(m)$	5.0e+04(a) / 5.0e+04(d)
301168	$W^-(1500, 1750) \to \tau\nu$	50(a) / 50(d)	3.7e−04	$K(m)$	1.4e+05(a) / 1.4e+05(d)
301169	$W^-(1750, 2000) \to \tau\nu$	50(a) / 50(d)	1.5e−04	$K(m)$	3.3e+05(a) / 3.3e+05(d)
301170	$W^-(2000, 2250) \to \tau\nu$	50(a) / 50(d)	6.5e−05	$K(m)$	7.7e+05(a) / 7.7e+05(d)
301171	$W^-(2250, 2500) \to \tau\nu$	50(a) / 50(d)	3.0e−05	$K(m)$	1.7e+06(a) / 1.7e+06(d)
301172	$W^-(2500, 2750) \to \tau\nu$	50(a) / 50(d)	1.5e−05	$K(m)$	3.3e+06(a) / 3.3e+06(d)
301173	$W^-(2750, 3000) \to \tau\nu$	50(a) / 50(d)	7.3e−06	$K(m)$	6.8e+06(a) / 6.8e+06(d)
301174	$W^-(3000, 3500) \to \tau\nu$	50(a) / 50(d)	5.7e−06	$K(m)$	8.8e+06(a) / 8.8e+06(d)
301175	$W^-(3500, 4000) \to \tau\nu$	50(a) / 50(d)	1.6e−06	$K(m)$	3.1e+07(a) / 3.1e+07(d)
301176	$W^-(4000, 4500) \to \tau\nu$	50(a) / 50(d)	4.7e−07	$K(m)$	1.1e+08(a) / 1.1e+08(d)
301177	$W^-(4500, 5000) \to \tau\nu$	50(a) / 50(d)	1.4e−07	$K(m)$	3.6e+08(a) / 3.6e+08(d)
301178	$W^-(> 5000) \to \tau\nu$	50(a) / 50(d)	6.2e−08	$K(m)$	8.1e+08(a) / 8.1e+08(d)

Table A.7. Monte Carlo samples for backgrounds that contribute to both the electron and muon channels. For each dataset, the following is listed: the ATLAS Monte Carlo dataset ID, the physics process (including the mass range in GeV when appropriate), the number of generated events, the cross section times branching ratio, K-factor ($K(m)$ denotes a mass dependent K-factor is used, see appendix), and the equivalent integrated luminosity $L_{\text{int}} = N_{\text{evt}}/(\sigma B)$. Letters in the parentheses represent Monte Carlo samples with the 2015+2016 dataset pile-up profile with (a) and the 2017 dataset pile-up profile with (d).

Run	Process	N_{evt} [k]	σB [pb]	K-factor	L_{int} [fb^{-1}]
		Inclusive and mass binned $Z \to ee$			
361106	$Z \to ee$	79942(a) / 79340(d)	1.9e+03	$K(m)$	4.2e+01(a) / 4.2e+01(d)
301000	$Z(120, 180) \to ee$	499(a) / 1115(d)	1.7e+01	$K(m)$	2.9e+01(a) / 6.6e+01(d)
301001	$Z(180, 250) \to ee$	250(a) / 245(d)	2.9e+00	$K(m)$	8.6e+01(a) / 8.4e+01(d)
301002	$Z(250, 400) \to ee$	150(a) / 150(d)	1.1e+00	$K(m)$	1.4e+02(a) / 1.4e+02(d)
301003	$Z(400, 600) \to ee$	100(a) / 825(d)	2.0e−01	$K(m)$	5.0e+02(a) / 4.1e+03(d)
301004	$Z(600, 800) \to ee$	145(a) / 386(d)	3.7e−02	$K(m)$	3.9e+03(a) / 1.0e+04(d)
301005	$Z(800, 1000) \to ee$	50(a) / 50(d)	1.1e−02	$K(m)$	4.5e+03(a) / 4.5e+03(d)
301006	$Z(1000, 1250) \to ee$	50(a) / 50(d)	4.3e−03	$K(m)$	1.2e+04(a) / 1.2e+04(d)
301007	$Z(1250, 1500) \to ee$	50(a) / 12(d)	1.4e−03	$K(m)$	3.6e+04(a) / 8.6e+03(d)
301008	$Z(1500, 1750) \to ee$	50(a) / 50(d)	5.5e−04	$K(m)$	9.1e+04(a) / 9.1e+04(d)
301009	$Z(1750, 2000) \to ee$	100(a) / 25(d)	2.3e−04	$K(m)$	4.3e+05(a) / 1.1e+05(d)
301010	$Z(2000, 2250) \to ee$	50(a) / 12(d)	1.0e−04	$K(m)$	5.0e+05(a) / 1.2e+05(d)
301011	$Z(2250, 2500) \to ee$	50(a) / 50(d)	4.9e−05	$K(m)$	1.0e+06(a) / 1.0e+06(d)
301012	$Z(2500, 2750) \to ee$	50(a) / 50(d)	2.4e−05	$K(m)$	2.1e+06(a) / 2.1e+06(d)
301013	$Z(2750, 3000) \to ee$	50(a) / 50(d)	1.2e−05	$K(m)$	4.2e+06(a) / 4.2e+06(d)
301014	$Z(3000, 3500) \to ee$	10(a) / 40(d)	1.0e−05	$K(m)$	1.0e+06(a) / 4.0e+06(d)
301014	$Z(3000, 3500) \to ee$	10(a) / 40(d)	1.0e−05	$K(m)$	1.0e+06(a) / 4.0e+06(d)
301015	$Z(3500, 4000) \to ee$	50(a) / 12(d)	2.9e−06	$K(m)$	1.7e+07(a) / 4.1e+06(d)
301016	$Z(4000, 4500) \to ee$	50(a) / 46(d)	9.0e−07	$K(m)$	5.6e+07(a) / 5.1e+07(d)
301017	$Z(4500, 5000) \to ee$	50(a) / 11(d)	2.8e−07	$K(m)$	1.8e+08(a) / 3.9e+07(d)
301018	$Z(> 5000) \to ee$	50(a) / 50(d)	1.3e−07	$K(m)$	3.8e+08(a) / 3.8e+08(d)

Table A.8. Monte Carlo samples for backgrounds that contribute to the electron channel. For each dataset, the following is listed: the ATLAS Monte Carlo dataset ID, the physics process (including the mass range in GeV when appropriate), the number of generated events, the cross section times branching ratio, K-factor ($K(m)$ denotes a mass dependent K-factor is used), and the equivalent integrated luminosity $L_{\text{int}} = N_{\text{evt}}/(\sigma B)$. Letters in the parentheses represent Monte Carlo samples with the 2015+2016 dataset pile-up profile with (a) and the 2017 dataset pile-up profile with (d).

Run	Process	N_{evt} [k]	σB [pb]	K-factor	L_{int} [fb^{-1}]
		Inclusive and mass binned $Z \to \mu\mu$			
361107	$Z \to \mu\mu$	79874(a) / 80919(d)	1.9e+03	$K(m)$	4.2e+01(a) / 4.3e+01(d)
301020	$Z(120, 180) \to \mu\mu$	500(a) / 1486(d)	1.7e+01	$K(m)$	2.9e+01(a) / 8.7e+01(d)
301021	$Z(180, 250) \to \mu\mu$	250(a) / 898(d)	2.9e+00	$K(m)$	8.6e+01(a) / 3.1e+02(d)
301022	$Z(250, 400) \to \mu\mu$	150(a) / 1195(d)	1.1e+00	$K(m)$	1.4e+02(a) / 1.1e+03(d)
301023	$Z(400, 600) \to \mu\mu$	100(a) / 900(d)	2.0e−01	$K(m)$	5.0e+02(a) / 4.5e+03(d)
301024	$Z(600, 800) \to \mu\mu$	100(a) / 495(d)	3.7e−02	$K(m)$	2.7e+03(a) / 1.3e+04(d)
301025	$Z(800, 1000) \to \mu\mu$	50(a) / 250(d)	1.1e−02	$K(m)$	4.5e+03(a) / 2.3e+04(d)
301026	$Z(1000, 1250) \to \mu\mu$	50(a) / 100(d)	4.3e−03	$K(m)$	1.2e+04(a) / 2.3e+04(d)
301027	$Z(1250, 1500) \to \mu\mu$	50(a) / 50(d)	1.4e−03	$K(m)$	3.6e+04(a) / 3.6e+04(d)
301028	$Z(1500, 1750) \to \mu\mu$	50(a) / 50(d)	5.5e−04	$K(m)$	9.1e+04(a) / 9.1e+04(d)
301029	$Z(1750, 2000) \to \mu\mu$	50(a) / 50(d)	2.3e−04	$K(m)$	2.2e+05(a) / 2.2e+05(d)
301030	$Z(2000, 2250) \to \mu\mu$	50(a) / 50(d)	1.0e−04	$K(m)$	5.0e+05(a) / 5.0e+05(d)
301031	$Z(2250, 2500) \to \mu\mu$	50(a) / 50(d)	4.9e−05	$K(m)$	1.0e+06(a) / 1.0e+06(d)
301032	$Z(2500, 2750) \to \mu\mu$	50(a) / 50(d)	2.4e−05	$K(m)$	2.1e+06(a) / 2.1e+06(d)
301033	$Z(2750, 3000) \to \mu\mu$	50(a) / 50(d)	1.2e−05	$K(m)$	4.2e+06(a) / 4.2e+06(d)
301034	$Z(3000, 3500) \to \mu\mu$	50(a) / 50(d)	1.0e−05	$K(m)$	5.0e+06(a) / 5.0e+06(d)
301035	$Z(3500, 4000) \to \mu\mu$	50(a) / 50(d)	2.9e−06	$K(m)$	1.7e+07(a) / 1.7e+07(d)
301036	$Z(4000, 4500) \to \mu\mu$	50(a) / 50(d)	9.0e−07	$K(m)$	5.6e+07(a) / 5.6e+07(d)
301037	$Z(4500, 5000) \to \mu\mu$	50(a) / 50(d)	2.8e−07	$K(m)$	1.8e+08(a) / 1.8e+08(d)
301038	$Z(> 5000) \to \mu\mu$	50(a) / 50(d)	1.3e−07	$K(m)$	3.8e+08(a) / 3.8e+08(d)

Table A.9. Monte Carlo samples for backgrounds that contribute to the muon channel. For each dataset, the following is listed: the ATLAS Monte Carlo dataset ID, the physics process (including the mass range in GeV when appropriate), the number of generated events, the cross section times branching ratio, K-factor ($K(m)$ denotes a mass dependent K-factor is used), and the equivalent integrated luminosity $L_{\text{int}} = N_{\text{evt}}/(\sigma B)$. Letters in the parentheses represent Monte Carlo samples with the 2015+2016 dataset pile-up profile with (a) and the 2017 dataset pile-up profile with (d).

Run	Process	N_{evt} [k]	σB [pb]	K-factor	L_{int} [fb^{-1}]
		Inclusive and mass binned $Z \to \tau\tau$			
361108	$Z \to \tau\tau$	39495(a) / 37114(d)	1.9e+03	$K(m)$	2.1e+01(a) / 2.0e+01(d)
301040	$Z(120, 180) \to \tau\tau$	450(a) / 450(d)	1.7e+01	$K(m)$	2.6e+01(a) / 2.6e+01(d)
301041	$Z(180, 250) \to \tau\tau$	150(a) / 450(d)	2.9e+00	$K(m)$	5.2e+01(a) / 1.6e+02(d)
301042	$Z(250, 400) \to \tau\tau$	444(a) / 450(d)	1.1e+00	$K(m)$	4.0e+02(a) / 4.1e+02(d)
301043	$Z(400, 600) \to \tau\tau$	150(a) / 450(d)	2.0e−01	$K(m)$	7.5e+02(a) / 2.2e+03(d)
301044	$Z(600, 800) \to \tau\tau$	450(a) / 450(d)	3.7e−02	$K(m)$	1.2e+04(a) / 1.2e+04(d)
301045	$Z(800, 1000) \to \tau\tau$	450(a) / 450(d)	1.1e−02	$K(m)$	4.1e+04(a) / 4.1e+04(d)
301046	$Z(1000, 1250) \to \tau\tau$	450(a) / 450(d)	4.3e−03	$K(m)$	1.0e+05(a) / 1.0e+05(d)
301047	$Z(1250, 1500) \to \tau\tau$	450(a) / 450(d)	1.4e−03	$K(m)$	3.2e+05(a) / 3.2e+05(d)
301048	$Z(1500, 1750) \to \tau\tau$	350(a) / 350(d)	5.5e−04	$K(m)$	6.4e+05(a) / 6.4e+05(d)
301049	$Z(1750, 2000) \to \tau\tau$	235(a) / 235(d)	2.3e−04	$K(m)$	1.0e+06(a) / 1.0e+06(d)
301050	$Z(2000, 2250) \to \tau\tau$	450(a) / 450(d)	1.0e−04	$K(m)$	4.5e+06(a) / 4.5e+06(d)
301051	$Z(2250, 2500) \to \tau\tau$	350(a) / 350(d)	4.9e−05	$K(m)$	7.1e+06(a) / 7.1e+06(d)
301052	$Z(2500, 2750) \to \tau\tau$	350(a) / 350(d)	2.4e−05	$K(m)$	1.5e+07(a) / 1.5e+07(d)
301053	$Z(2750, 3000) \to \tau\tau$	350(a) / 350(d)	1.2e−05	$K(m)$	2.9e+07(a) / 2.9e+07(d)
301054	$Z(3000, 3500) \to \tau\tau$	350(a) / 350(d)	1.0e−05	$K(m)$	3.5e+07(a) / 3.5e+07(d)
301055	$Z(3500, 4000) \to \tau\tau$	400(a) / 400(d)	2.9e−06	$K(m)$	1.4e+08(a) / 1.4e+08(d)
301056	$Z(4000, 4500) \to \tau\tau$	315(a) / 315(d)	9.0e−07	$K(m)$	3.5e+08(a) / 3.5e+08(d)
301057	$Z(4500, 5000) \to \tau\tau$	350(a) / 350(d)	2.8e−07	$K(m)$	1.2e+09(a) / 1.2e+09(d)
301058	$Z(> 5000) \to \tau\tau$	350(a) / 350(d)	1.3e−07	$K(m)$	2.7e+09(a) / 2.7e+09(d)

Table A.10. Monte Carlo samples for backgrounds that contribute to both the electron and muon channels. For each dataset, the following is listed: the ATLAS Monte Carlo dataset ID, the physics process (including the mass range in GeV when appropriate), the number of generated events, the cross section times branching ratio, K-factor ($K(m)$ denotes a mass dependent K-factor is used), and the equivalent integrated luminosity $L_{\text{int}} = N_{\text{evt}}/(\sigma B)$. Letters in the parentheses represent Monte Carlo samples with the 2015+2016 dataset pile-up profile with (a) and the 2017 dataset pile-up profile with (d).

B. Low-p_T Control Region

This appendix documents some additional checks that were performed to further understand the overestimation of the background observed at low p_T in the electron channel as shown in Figure 11.1. The distributions in Figure B.1 show the overestimation of the background in the various distributions for $p_T < 145$ GeV in the final selection. The overestimation

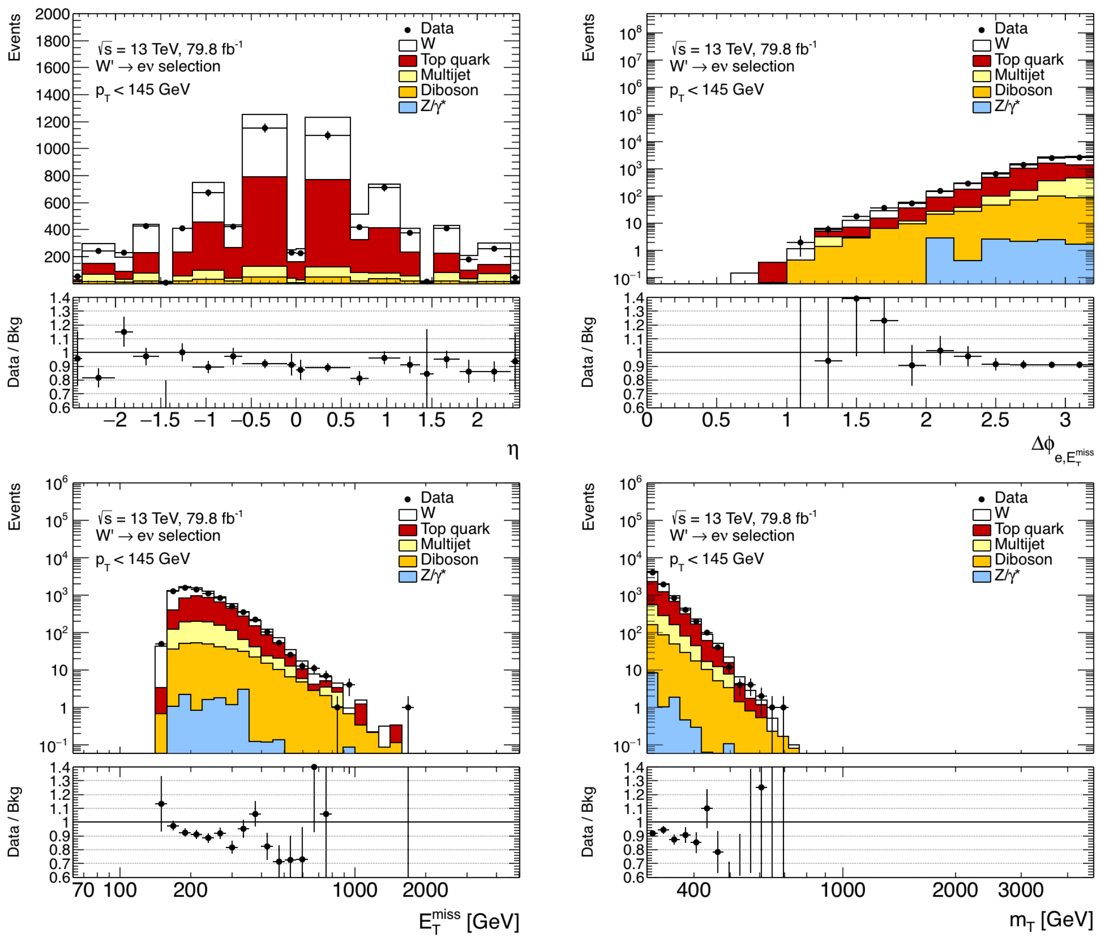

Figure B.1. Distributions of the η (top left), $|\Delta\phi_{e,E_T^{\text{miss}}}|$ (top right), E_T^{miss} (bottom left) and m_T (bottom right) for electron p_T less than 145 GeV in the final selection.

is about 10% and it is not localized any of these distributions. Since the transverse mass cut of 300 GeV in the final selection leads asymmetric event topologies for $p_{\mathrm{T}} < 145$ GeV events, it is compared with sysmetric event topologies as shown in Figure B.2.

The distributions in Figure B.2 show the $|\Delta\phi_{e,E_{\mathrm{T}}^{\mathrm{miss}}}|$ and the absolute value of the difference between the electron p_{T} and $E_{\mathrm{T}}^{\mathrm{miss}}$ for $p_{\mathrm{T}} < 145$ GeV on the left hand side and $145 < p_{\mathrm{T}} < 300$ GeV on the right hand side. As expected the width of the $|\Delta\phi_{e,E_{\mathrm{T}}^{\mathrm{miss}}}|$ distribution is narrower, and the difference between the electron p_{T} and $E_{\mathrm{T}}^{\mathrm{miss}}$ is peaking at 0 for the symmetric event topology as shown on the right hand side. The agreement between the

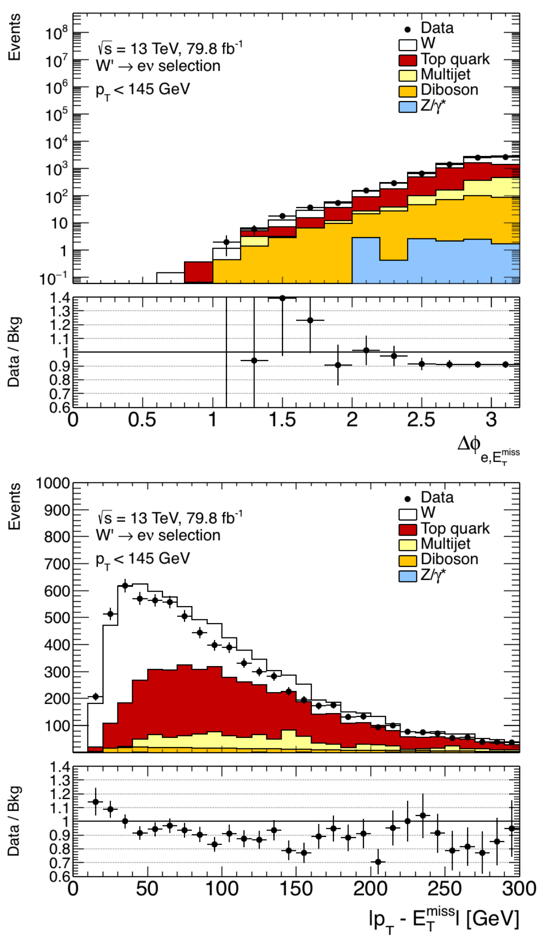

Figure B.2. Distributions of the $|\Delta\phi_{e,E_{\mathrm{T}}^{\mathrm{miss}}}|$ (top) and $|p_{\mathrm{T}} - E_{\mathrm{T}}^{\mathrm{miss}}|$ (bottom) between electron p_{T} and $E_{\mathrm{T}}^{\mathrm{miss}}$ for electron $p_{\mathrm{T}} < 145$ GeV on the left hand side and $145 < p_{\mathrm{T}} < 300$ GeV on the right hand side.

data and background is reasonably good for the symmetric event topology. On the other hand, the difference between the electron p_{T} and $E_{\mathrm{T}}^{\mathrm{miss}}$ for $p_{\mathrm{T}} < 145\,\mathrm{GeV}$ shows a relatively large difference as shown in Figure B.2 (bottom left). In this plot, it can be seen that the shape in the ratio panel follows the one for $145 < p_{\mathrm{T}} < 300\,\mathrm{GeV}$ for the first few bins, but it is systematically lower around 100 - 200 GeV. In addition, the magnitude and the range of the overstimation are similiar to the contribution of multijet background. At this point, it is not surprising that the multijet background estimation is not working well since the fake efficiency is estimated only up to $E_{\mathrm{T}}^{\mathrm{miss}}$ less than 60 GeV as shown in Figure 9.5 (bottom left). The fake efficiency takes the $|\Delta\phi_{e,E_{\mathrm{T}}^{\mathrm{miss}}}|$ to resolve the $E_{\mathrm{T}}^{\mathrm{miss}}$ dependency but it is not sufficient. The discontinuity at p_{T} around 150 GeV in Figure 11.1 also supports as it coincides with the discontinuity in the fake efficiency as shown in Figure 9.5 (top left).

The distributions in Fig. B.3 show the p_{T}, $E_{\mathrm{T}}^{\mathrm{miss}}$, η, $|\Delta\phi_{e,E_{\mathrm{T}}^{\mathrm{miss}}}|$, $|p_{\mathrm{T}} - E_{\mathrm{T}}^{\mathrm{miss}}|$ and m_{T} distributions without the multijet background, and it can be seen that the data and background agree quite well without the multijet background contribution.

The impact to the final result should be marginal as it is a 5–10% overestimation of 10% of the total background (0.5–1% to the total background). It also populates in the low m_{T} region as shown in Figure B.1 (right bottom). In the ratio panel, only the first and third bins are not covered by the systematic uncertainty band which is approximately 5% in this region. Further studies are ongoing to improve the multijet background estimation, especially in terms of $E_{\mathrm{T}}^{\mathrm{miss}}$ dependency.

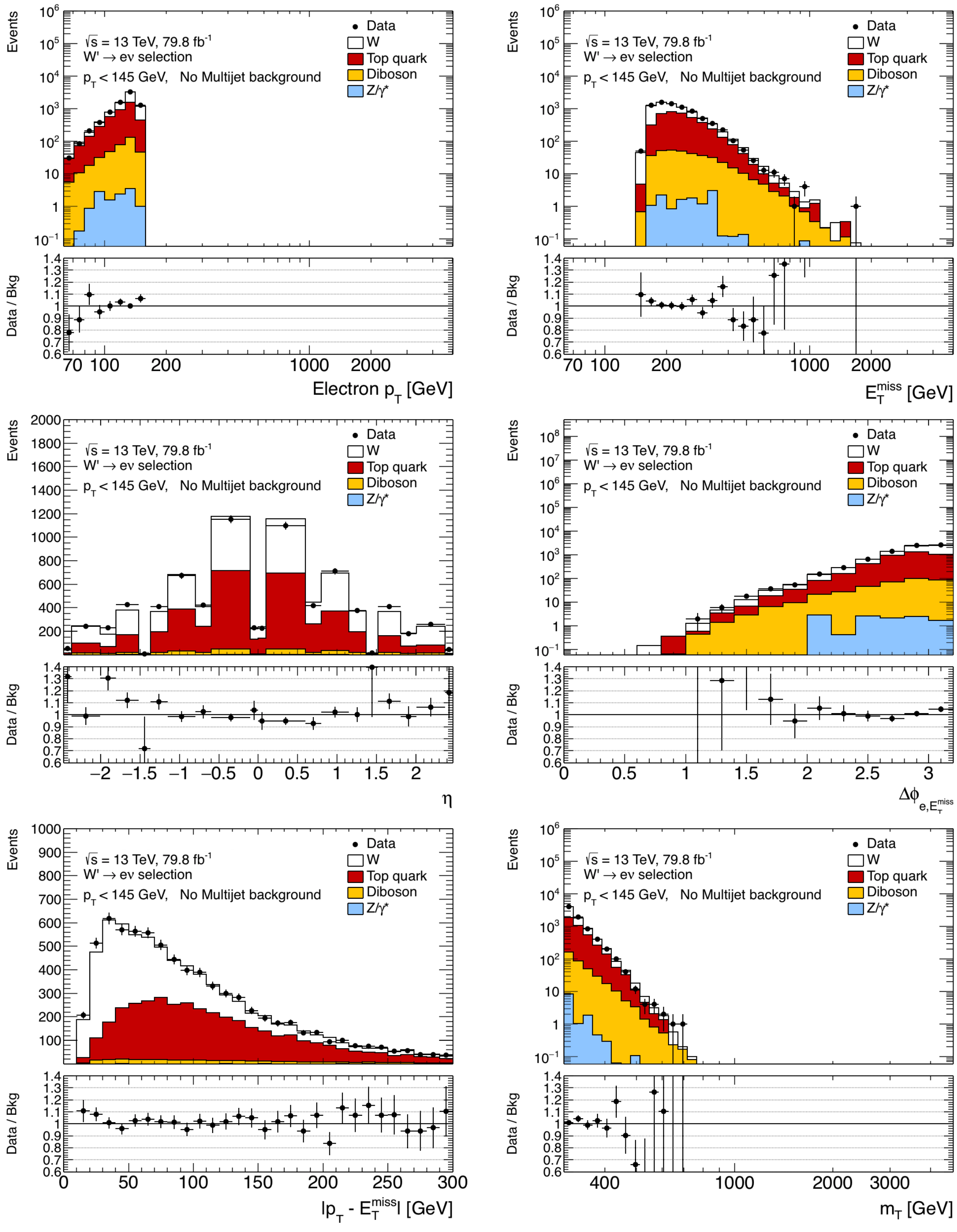

Figure B.3. Distributions of the p_{T}, $E_{\mathrm{T}}^{\mathrm{miss}}$, η, $|\Delta\phi_{e,E_{\mathrm{T}}^{\mathrm{miss}}}|$, $|p_{\mathrm{T}} - E_{\mathrm{T}}^{\mathrm{miss}}|$ and m_{T} without the multijet background for electron p_{T} less than 145 GeV in the final selection.

BIBLIOGRAPHY

[1] E. Rutherford, *The scattering of alpha and beta particles by matter and the structure of the atom*, Phil. Mag. **21** (1911) 669.

[2] J. Chadwick, *Possible Existence of a Neutron*, Nature **129** (1932) 312.

[3] J. J. Thomson, *Cathode rays*, Phil. Mag. **44** (1897) 293.

[4] M. Gell-Mann, *A Schematic Model of Baryons and Mesons*, Phys. Lett. **8** (1964) 214.

[5] ATLAS Collaboration, *Observation ofa new particle in the search for the Standard Model Higgs boson with the ATLAS detector at the LHC*, Phys. Lett. B **716** (2012) 1.

[6] CMS Collaboration, *Observation ofa new boson at a mass of125 GeV with the CMS experiment at the LHC*, Phys. Lett. B **716** (2012) 30.

[7] M. Peskin and D. Schroeder, *An Introduction to Quantum Field Theory.* Westview, 1995.

[8] G. Hinshaw et al., *Five-Year Wilkinson Microwave Anisotropy Probe (WMAP) Observations: Data Processing, Sky Maps, and Basic Results*, Astrophys. J. Suppl. **180** (2009) 225.

[9] D. Clowe et al., *A direct empirical proof of the existence of dark matter*, Astrophys. J. **648** (2006) 109.

[10] Planck Collaboration, *Planck 2013 results. I. Overview of Products and Scientific Results*, Astronomy and Astrophyics **571** (2014).

[11] P. Fayet, *Supersymmetry and weak, electromagnetic and strong interactions*, Phys. Lett. B **64** (1976) 159.

[12] T. Appelquist et al., *Bounds on universal extra dimensions*, Phys. Rev. D **64** (2001) 035002.

[13] K. Hsieh et al., *Global analysis of general SU(2) $\times$ SU(2) $\times$ U(1) models with precision data*, Phys. Rev. D **82** (2010) 035011.

[14] A. Maiezza et al., *Left-Right Symmetry at LHC*, Phys. Rev. D **82** (2010) 055022.

[15] G. Altarelli et al., *Searching for New Heavy Vector Bosons in $p\bar{p}$ Colliders*, Z. Phys. C **47** (1990) 676.

[16] C. Arina et al., *Constraints on sneutrino dark matter from LHC Run 1*, JHEP **05** (2015) 142.

[17] A. Birkedal et al., *Dark matter at colliders: a model independent approach*, Phys. Rev. D **70** (2004) 077701.

[18] J. Goodman et al., *Constraints on light Majorana dark matter from colliders*, Phys. Lett. B **695** (2011) 185.

[19] Y. Bai et al., *The Tevatron at the frontier of dark matter direct detection*, JHEP **12** (2010) 048.

[20] J. Goodman et al., *Constraints on dark matter from colliders*, Phys. Rev. D **82** (2010) 116010.

[21] L. R. Evans and P. Bryant, *LHC Machine*, JINST **3** (2008) S08001.

[22] ATLAS Collaboration, *The ATLAS Experiment at the CERN Large Hadron Collider*, JINST **3** (2008) S08003.

[23] E. Mobs and E. Anais, *The CERN accelerator complex*, `https://cds.cern.ch/record/2225847`.

[24] G.Papotti et al., *Operation of the LHC with Protons at High Luminosity and High Energy*, in *Proceedings, 7th International Particle Accelerator Conference (IPAC 2016)*, Busan, Korea, May 2016.

[25] ATLAS Collaboration, *Commissioning of the ATLAS Muon Spectrometer with Cosmic Rays*, Eur. Phys. J. C **70** (2010) 875.

[26] T. Cornelissen et al., *Concepts, Design and Implementation of the ATLAS New Tracking (NEWT)*, `ATLAS-SOFT-PUB-2007-007`, `https://cds.cern.ch/record/1020106`.

[27] R. Frühwirth, *Application of Kalman Filtering to Track and Vertex Fitting*, Nucl. Instrum. Meth.A **262** (1987) 444.

[28] T. Cornelissen et al., *The global χ^2 track fitter in ATLAS*, J. Phys. Conf. Ser. **119** (2008) 032013.

[29] W. Lampl et al., *Calorimeter Clustering Algorithms: Description and Performance*, `ATL-LARG-PUB-2008-002`, `https://cds.cern.ch/record/1099735`.

[30] ATLAS Collaboration, *Topological cell clustering in the ATLAS calorimeters and its performance in LHC Run 1*, Eur. Phys. J. C **77** (2017) 490.

[31] ATLAS Collaboration, *Electron and photon reconstruction and performance in ATLAS using a dynamical, topological cell clustering-based approach*, `ATLAS-PHYS-PUB-2017-022`, `https://cds.cern.ch/record/2298955`.

[32] ATLAS Collaboration, *Improved electron reconstruction in ATLAS using the Gaussian sum filter-based model for bremsstrahlung*, `ATLAS-CONF-2012-047`, `http://inspirehep.net/record/1204271`.

[33] ATLAS Collaboration, *Electron efficiency measurements with the ATLAS detector using 2012 LHC proton–proton collision data*, The European Physical Journal C **77** (2017) 195.

[34] ATLAS Collaboration, *Electron efficiency measurements with the ATLAS detector using the 2015 LHC proton-proton collision data*, `ATLAS-CONF-2016-024`, `http://inspirehep.net/record/1467063`.

[35] A. Hoecker et al., *TMVA: toolkit for multivariate data analysis*, PoS ACAT **040** (2007), `arXiv:physics/0703039`.

[36] M. Cacciari and G. P. Salam, *Pileup subtraction using jet areas*, Phys. Lett. B **659** (2008) 119.

[37] ATLAS Collaboration, *Electron and photon energy calibration with the ATLAS detector using LHC Run 1 data*, Eur. Phys. J. C **74** (2014) 3071.

[38] ATLAS Collaboration, *Muon reconstruction performance of the ATLAS detector in proton–proton collision data at* $\sqrt{s} = 13$ *TeV*, Eur. Phys. J. C **76** (2016) 292.

[39] M. Cacciari, G. P. Salam and G. Soyez, *The Anti-k(t) jet clustering algorithm*, JHEP **2008** no. 04, (063) 2008.

[40] ATLAS Collaboration, *Jet energy scale measurements and their systematic uncertainties in proton–proton collisions at* $\sqrt{s} = 13$ *TeV with the ATLAS detector*, Phys. Rev. D **96** (2017) 072002.

[41] ATLAS Collaboration, *Performance ofpile-up mitigation techniques for jets in pp collisions at* $\sqrt{s} = 8$ *TeV using the ATLAS detector*, Eur. Phys. J. C **76** (2016) 581.

[42] ATLAS Collaboration, *Jet reconstruction and performance using particle flow with the ATLAS Detector*, Eur. Phys. J. C **77** (2017) 466.

[43] ATLAS Collaboration, *Selection of jets produced in 13 TeV proton-proton collisions with the ATLAS detector*, ATLAS-CONF-2015-029, http://inspirehep.net/record/1384980.

[44] ATLAS Collaboration, *Performance ofpile-up mitigation techniques for jets in pp collisions at* $\sqrt{s} = 8$ *TeV using the ATLAS detector*, Eur. Phys. J. C **76** (2016) 581.

[45] ATLAS Collaboration, *Measurements ofthe photon identification efficiency with the ATLAS detector using 4.9 fb*$^{-1}$ *of pp collision data collected in 2011*, ATLAS-CONF-2012-123, http://cds.cern.ch/record/1473426.

[46] ATLAS Collaboration, *Reconstruction, Energy Calibration, and Identification ofHadronically Decaying Tau Leptons in the ATLAS Experiment for Run-2 ofthe LHC*, ATLAS-PHYS-PUB-2015-045, https://cds.cern.ch/record/2064383.

[47] ATLAS Collaboration, E_T^{miss} *performance in the ATLAS detector using 2015-2016 LHC pp collisions*, ATLAS-CONF-2018-023, https://cds.cern.ch/record/2625233.

[48] ATLAS Collaboration, *Forward Jet Vertex Tagging: A new technique for the identification and rejection offorward pileup jets*, ATLAS-PHYS-PUB-2015-034, https://cds.cern.ch/record/2042098.

[49] T. Sjöstrand, *Monte Carlo Generators*, arXiv:hep-ph/0611247.

[50] T. Sjöstrand et al., *A Brief Introduction to PYTHIA 8.1*, Comput. Phys. Commun. **178** (2008) 852.

[51] S. Alioli et al., *A general framework for implementing NLO calculations in shower Monte Carlo programs: the POWHEG BOX*, JHEP **06** (2010) 43.

[52] J. Alwall et al., *A Standard format for Les Houches event file*, Comput. Phys. Commun. **176** (2007) 300.

[53] T. Gleisberg et al., *Event generation with Sherpa 1.1*, JHEP **02** (2009) 007.

[54] M. Dobbs et al., *The HepMC C++ Monte Carlo event record for high energy physics*, Comput. Phys. Commun. **134** (2001) 41.

[55] S. Agostinelli et al., *Geant4 a simulation toolkit*, Nucl. Instrum. Methods Phys. Res. A **506** (2003) 250.

[56] ATLAS Collaboration, *The ATLAS Simulation Infrastructure*, Eur. Phys. J. C **70** (2010) 823.

[57] R. D. Ball et al., *Parton distributions with LHC data*, Nucl. Phys. B **867** no. 2, (2013) 244–289.

[58] C. Anastasiou et al., *High precision QCD at hadron colliders: Electroweak gauge boson rapidity distributions at NNLO*, Phys. Rev. D **69** (2004) 094008.

[59] S. Dulat et al., *The CT14 Global Analysis of Quantum Chromodynamics*, Phys. Rev. D **93** (2016) 033006.

[60] C. Quigg, *LHC Physics Potential vs. Energy*, `arXiv:0908.3660v2`.

[61] M. Tanabashi et al., *Particle Data Group*, Phys. Rev. D **98** (2018) 030001.

[62] N. Kidonakis, *Next-to-next-to-leading logarithm resummation for s-channel single top quark production*, Phys. Rev. D **81** no. 5, (2010) 1–17.

[63] N. Kidonakis, *Next-to-next-to-leading-order collinear and soft gluon corrections for t-channel single top quark production*, Phys. Rev. D **83** no. 9, (2011) 1–11.

[64] T. Golling et al., *The ATLAS Data Quality Defect Database System*, The European Physical Journal C **72** (2012) 1960.

[65] S. M. Weber, *Operation and Performance of the ATLAS Level-1 Calorimeter and Level-1 Topological Triggers in Run 2 at the LHC*, in *The European Physical Society Conference on High Energy Physics (EPS-HEP2017)*, Venice, Italy, July 2017.

[66] ATLAS Collaboration, *Search for new phenomena in dijet events using* 37 fb^{-1} *of pp collision data collected at* $\sqrt{s} = 13$ *TeV with the ATLAS detector*, Phys. Rev. D **96** (2017) 052004.

[67] ATLAS Collaboration, *Search for new high-mass phenomena in the dilepton final state using* 36 fb^{-1} *of proton-proton collision data at* $\sqrt{s} = 13$ *TeV with the ATLAS detector*, J. High Energ. Phys. **2017** (2017) 182.

[68] ATLAS Collaboration, *Measurement of the muon reconstruction performance ofthe ATLAS detector using 2011 and 2012 LHC proton-proton collision data*, Eur. Phys. J. C **74** (2014) 3130.

[69] ATLAS Collaboration, *Measurement of the Inelastic Proton-Proton Cross Section at* $\sqrt{s} = 13$ *TeV with the ATLAS Detector at the LHC*, Phys. Rev. Lett. **117** (2016) 182002.

[70] ATLAS Collaboration, *Luminosity Determination in pp Collisions at* $\sqrt{s} = 8$ *TeV using the ATLAS Detector at the LHC*, Eur. Phys. J. C **76** (2016) 653.

[71] G. A. et al., *The new LUCID-2 detector for luminosity measurement and monitoring in ATLAS*, JINST **13** no. 07, (2018) P07017.

[72] J. Gao et al., *A meta-analysis of parton distribution functions*, J. High Energ. Phys. **07** (2014) 035.

[73] J. B. et al., *PDF4LHC recommendations for LHC Run II*, J. Phys. G: Nucl. Part. Phys. **43** (2016) 023001.

[74] V. Lombardo, *Diboson production cross section at LHC*, `arXiv:1305.3773`.

[75] G. C. et al., *Asymptotic formulae for likelihood-based tests of new physics*, Eur. Phys. J. C **71** (2011) 1554.

[76] W. Wilks, *The large-sample distribution ofthe likelihood ratio for testing composite hypotheses*, Ann. Math. Statist. **9** (1938) 60.

[77] E. G. et al., *Trial factors for the look elsewhere effect in high energy physics*, Eur. Phys. J. C **70** (2010) 525.

[78] F. B. et al., *BAT: The Bayesian analysis toolkit*, J. Phys. Conf. Ser. **331** (2011) 072040.

[79] D0 Collaboration, *Search for W' Bosons Decaying to an Electron and a Neutrino with the D0 Detector*, Phys. Rev. Lett. **100** (2008) 031804.

[80] CDF Collaboration, *Search for a New Heavy Gauge Boson W' with Electron + $\not{E}_{\mathrm{T}}$ Event Signature in $p\bar{p}$ collisions at $\sqrt{s} = 1.96$ TeV*, Phys. Rev. D **83** (2011) 031102.

[81] ATLAS Collaboration, *Search for new resonances in events with one lepton and missing transverse momentum in pp collisions at $\sqrt{s} = 13$ TeV with the ATLAS detector*, Phys. Lett. B **762** (2016) 334.

[82] CMS Collaboration, *Search for heavy gauge W bosons in events with an energetic lepton and large missing transverse momentum at $\sqrt{s} = 13$ TeV*, Phys.Lett. B **770** (2017) 278.

[83] ATLAS Collaboration, *Search for a new heavy gauge boson resonance decaying into a lepton and missing transverse momentum in 36 fb^{-1} of pp collisions at $\sqrt{s} = 13$ TeV with the ATLAS experiment*, Eur. Phys. J. C **78** (2018) 401.

[84] CMS Collaboration, *Search for high-mass resonances in final states with a lepton and missing transverse momentum at $\sqrt{s} = 13$ TeV*, J. High Energ. Phys. **2018** (2018) 128.

[85] ATLAS Collaboration, *Search for a new heavy gauge boson resonance decaying into a lepton and missing transverse momentum in 79.8 fb^{-1} of pp collisions at $\sqrt{s}$ = 13 TeV with the ATLAS experiment*, `ATLAS-CONF-2018-017`.

Curriculum Vitae

KyungEon Choi

Education

Indiana University Bloomington, USA
Ph.D, Physics — Dec 2018
Disseration: *Search for a new heavy gauge boson in final state with one lepton and missing transverse momentum with the ATLAS detector*
Advisor: Professor Harold G. Evans

Pusan National University, South Korea
M.S., Physics — Feb 2009
Thesis: *Development of Acrylic Cherenkov Detector*
Advisor: Professor In-Kwon Yoo

B.S., Physics — Feb 2006

Research Highlights

Search for a new heavy gauge boson $W' \to \ell\nu$ at ATLAS — 2017 - present
- Main analyzer of electron channel for 2015-2017 data: main executer of the analysis, data-driven background estimation using the matrix method, systematics estimation.
- One of the first public results using 2017 data.
- The result was presented at LHCP2018 (CONF-2018-017).

MC development for stable exotic particles at ATLAS — 2017
- Responsible for xAOD MC productions from modified LHA files.
- Fixed the GEANT4 ionization modeling for charginos.

TRT detector software group at ATLAS — 2012 - 2014, 2017
- Led the TRT dE/dx team (a group of 5 people) and developed a pile-up robust TRT dE/dx tool.
- Studied the TRT dE/dx performance for Heavy Stable Charged Exotic Particles such as $\chi_0^{\pm}$ and R-hadrons.
- Responsible for xAOD data productions from RAW or MC GEANT HITS files.
- Performed TRT MC low-level parameter tunes such as thresholds and timing for both Xe and Ar gas mixtures, and optimized the TRT MC settings.

ITS Upgrade project at ALICE — 2014 - 2016

- One of main participants for test beams at CERN PS, and analyzed the results using the EUTelescope framework.
- Performed lab tests for the characterization of prototype chips using ^{55}Fe source. I studied the effect of neutron irradiation (NIEL) to the various types of silicon pixel sensors.
- Led a team (a group of 4 people) for the characterization of pixel chips and the initial setup as a one of module assembly site.

Measurement of material budget at STAR 2008

- Measured the material budget of the STAR detector for data and MC from reconstructed photon conversion vertices.

Development of prototype Cherenkov detector 2006 - 2008

- Participated test beams for the prototype Cherenkov detector for the CBM experiment. I contributed to the DAQ and the alignment of detector.
- Designed and developed the acrylic Cherenkov detector with a multi-anode PMT. I have rich experiences with fabrications of small detector parts using a milling machine and electronic instruments such as CAMAC and NIM modules.

Presentations

"Search for a new heavy particle in final states with one lepton (e/μ) and missing transverse energy in the ATLAS detector with 80 fb^{-1} of integrated luminosity",
Poster session, ATLAS Week, CERN — Feb 2018

"Tracking and Vertexing with the ATLAS Inner Detector in the LHC Run-2",
Parallel session, TIPP 2017, Beijing, China — May 2017

"Gamma - conversion tomography of STAR Silicon Detector",
Parallel session, ATHIC 2008, Tsukuba, Japan — Oct 2008

Awards

Indiana University Graduate Fellowship — Aug 2010
Global Internship Fellowship (Brookhaven National Laboratory) Aug 2007 - Jan 2008

Schools

The CERN-Fermilab Hadron Collider Physics Summer School — Aug 2017
The Nuclear Physics School — June 2006

Mentoring Experience

Philipp König (graduate student at University of Bonn) for TRT Qualification task
Nadezda Proklova (graduate student at MEPhI) for TRT Qualification task
Jiyoung Kim (graduate student at Pusan National Univeristy) for Master thesis work

Outreach

Guided tour at CERN for visiting science high school students from Korea — Jan 2017